Confinement and the supercritical Pomeron in QCD

Alan R. White*
High Energy Physics Division, Argonne National Laboratory, 9700 South Cass Avenue, Illinois 60439
(Received 30 January 1998; published 4 September 1998)

Deep-inelastic diffractive scaling violations have provided fundamental insight into the QCD Pomeron, suggesting a single-gluon inner structure rather than that of a perturbative two-gluon bound state. This paper derives a high-energy, transverse momentum cutoff, confining solution of QCD. The Pomeron, in a first approximation, is a single Reggeized gluon plus a ''wee-parton'' component that compensates for the color and particle properties of the gluon. This solution corresponds to a supercritical phase of Reggeon field theory. Beginning with the multi-Regge behavior of massive quark and gluon amplitudes, Reggeon unitarity is used to derive a Reggeon diagram description of a wide class of multi-Regge amplitudes, including those describing the formation and scattering of bound-state Regge poles. When quark and gluon masses are taken to zero, a logarithmic divergence is produced by helicity-flip Reggeon interactions containing the infrared quark triangle anomaly. With the gauge symmetry partially broken, this divergence selects the bound states and amplitudes of a confining theory. Both the Pomeron and hadrons have an anomalous color-parity wee-parton component. For the Pomeron the wee-parton component determines that it carries negative color charge parity and that the leading singularity is an isolated Regge pole.
[S0556-2821(98)01319-8]

PACS number(s): 12.38.Aw, 11.55.Jy, 12.40.Nn

I. INTRODUCTION

This is the first of two articles that will report our recent progress in ''understanding the Pomeron in QCD.'' A complete understanding of the Pomeron requires no more or less than solving the theory at high energy. While high energy can be expected to keep the theory as close as possible to perturbation theory, nevertheless the nonperturbative properties of confinement and chiral symmetry breaking must emerge. Therefore this paper (and that following) necessarily also reports progress in ''understanding confinement and chiral symmetry breaking.''

Our formalism is entirely based within the high-energy S matrix. We start with the multi-Regge behavior of massive quarks and gluons and arrive at the S matrix for hadrons via an extended analysis of infrared divergences within multi-Regge amplitudes. Rather than appearing as consequences of a nonperturbative vacuum, both confinement and chiral symmetry breaking are properties of the bound-state (Regge pole) spectrum. It is a crucial strength of the multi-Regge formalism that we can simultaneously study the formation of bound states and their scattering amplitudes. Hadrons, and the Pomeron by which they scatter, emerge together as Regge pole states at spacelike momentum transfer. Indeed, there is a close link between confinement, chiral symmetry breaking, and the Regge pole property of the Pomeron.

The main purpose of this first paper is to establish the relationship, which we initially suggested over 17 years ago [1], between a supercritical Pomeron phase of Reggeon field theory [2] (RFT) and a confining solution of QCD with the gauge symmetry broken to SU(2) (''partially broken QCD''). In this phase the Pomeron is, approximately, an SU(2) singlet Reggeized gluon plus a ''wee-parton'' component that compensates for the particle properties of the gluon. The restoration of SU(3) gauge symmetry is directly related to the critical behavior [3] of the Pomeron. However, in the RFT formalism, the transverse momentum cutoff is a relevant parameter at the critical phase transition. This implies that the supercritical phase can appear with the full gauge symmetry if a physical cutoff is present. Alternatively, the large Q^2 of deep-inelastic scattering can be viewed as introducing a (local) lower transverse momentum cutoff which effectively removes the critical behavior altogether and (locally) keeps the theory in the supercritical phase as the full gauge symmetry is restored.

We will postpone, until the second paper, almost all discussion of the many issues of principle and interpretation involved in connecting our results to other, more conventional, field theory formalisms. However, if our results can be interpreted within a field-theoretic framework, it is likely to be that of light-cone quantization. In this formalism it is hoped [4] that the zero-mode (zero-longitudinal-momentum) component of physical states can reproduce the nontrivial vacuum properties of confinement and chiral symmetry breaking. At infinite momentum the ''zero modes'' are simply the ''wee partons,'' carrying finite momentum. Correspondingly, in our solution of partially broken QCD, both the Pomeron and hadrons have a zero-momentum component which we refer to as a ''wee-parton component.'' This component, which in the past we have called a ''Reggeon condensate,'' is closely related to the fermion anomaly and carries ''anomalous'' color parity (i.e., it contains vectorlike multigluon combinations carrying positive color parity: cf. the three-gluon component of the winding-number current.)

The anomalous color parity of the wee-parton component determines that the Pomeron carries negative color charge parity overall and also that its leading singularity is a Regge pole with a trajectory that is exchange degenerate with that of a massive, Reggeized, gluon. There is confinement in that

*Email address: arw@hep.anl.gov

the states carry color zero and have a completeness property and also there are no massless multigluon states. Note that the Balitskii-Fadin-Kuraev-Lipatov (BFKL) Pomeron [5] appears in the positive color parity sector. Our analysis implies that it does not couple to the physical states. As we will discuss in detail in the second paper, the color parity property of the wee-parton component also determines the chiral-symmetry-breaking nature of the hadron spectrum. In fact, without chiral symmetry breaking it would be inconsistent for a negative color parity Pomeron to describe total cross sections and the BFKL Pomeron would not decouple. While it may eventually be possible to formulate our solution in terms of a light-cone quantization procedure which leads directly to the correct properties of physical states, we would like to emphasize that we have been able to understand the physics of the wee-parton component only by determining the role of the fermion anomaly in the construction of the fully unitary, high-energy, multiparticle S matrix. This is a very complicated and intricate problem which it is hard to imagine studying outside of the multi-Regge framework we use.

The discovery of deep-inelastic scaling provided the impetus for the original development of the parton model and underlaid the formulation of QCD as the theory of the strong interaction. Deep-inelastic scaling violations now provide much of the information on short-distance partonic structure that is the basis for the application of perturbative QCD to a wide range of hadronic physics. We believe that the observation [6] of diffractive deep-inelastic scattering at the DESY *ep* collider HERA will turn out to be almost as significant in developing an understanding of how QCD describes strong-interaction physics. This is because it tells us how the parton model operates beyond the simplest short-distance processes and, in doing so, provides vital information on the wee-parton component of physical states. The Pomeron, which, as we have already implied, is deeply tied to the long distance dynamics of confinement and chiral symmetry breaking, is studied experimentally at short distances. By analyzing diffractive scaling violations, H1 have shown [7] that, in deep-inelastic scattering, the Pomeron behaves like a single gluon (rather than the perturbative two-gluon bound-state BFKL Pomeron [5]). Within perturbative QCD, gauge invariance makes this a very difficult property to realize. From our perspective, the H1 analysis [7] implies [8] that at intermediate Q^2 values the Pomeron is effectively in the supercritical phase. The phenomenon can also be understood directly within QCD, once the physics of the wee-parton component is incorporated [8].

We first suggested that the Pomeron could appear as a single (Reggeized) gluon in [1]. The idea that the Pomeron should carry negative color parity and that this is closely tied to chiral symmetry breaking was also present. Although this long paper was accepted for publication, the journal Editors insisted it be split in two. After eventually conceding this point, we then decided that further development was needed before ''final'' publication. We first attempted to do this in [9] by (partially) recasting the S-matrix language of [1] in the more field-theoretic language of light-cone quantization. However, essentially because of problems with our treatment of the fermion anomaly, the results were still unsatisfactory. We then returned to the S-matrix formalism of multi-Regge theory and, in two lengthy articles [10,11], laid out what we hoped could be developed into a complete dynamical understanding of the Pomeron in QCD. As in our original paper [1] (and the present paper), our aim was to use general multi-Regge theory to carry out a combined infrared and multi-Regge limit analysis, the essential idea being always the association of supercritical RFT with partially broken QCD and the identification of the critical Pomeron phase transition [3] with the restoration of the full gauge symmetry.

Unfortunately the arguments presented in [11] were still very incomplete. Even so, they gave a fundamentally different picture of the Pomeron to what might be called the conventional, perturbative, BFKL picture [5]. In addition to the incompleteness of the arguments, the techniques we were using were (and still are) unfamiliar to most theorists studying QCD. The analysis also depended on our version of the supercritical Pomeron which was the subject of heated controversy in the pre-QCD years of RFT [12]. As a result, we anticipated that the validity of our arguments would take many years of theoretical study to resolve. We certainly did not anticipate that experiment could play a role in what we regarded as fundamentally a (deep) theoretical issue.

Remarkably, as we discussed above, it now appears that experiment is providing significant support for our picture. The experimental results have encouraged us to return to our earlier work and make another major effort to put it on firmer ground and to make it accessible. The outcome is the present article (and its successor). This time around, we believe we really have solved the problem. A major reason for the incompleteness of our earlier work was ignorance as to how to construct the complicated Reggeon diagrams that are necessary to discuss the simultaneous formation and scattering of bound states. The solution of this problem via Reggeon unitarity and the realization of the special role played by ''helicity-flip vertices'' is, we believe, a significant achievement of the early sections of this paper. Helicity-flip vertices only appear as interactions coupling dynamically different Reggeon channels. They do not appear as interactions within the normal Reggeon diagrams that, for example, generate Pomeron RFT. The other central difficulty in our previous work was that, although we understood qualitatively that the fermion anomaly should have a crucial infrared dynamical role, we were unable to pin down specifically how this is the case. The interrelation with ultraviolet regularization seemed inevitably to lead to unresolvable field-theoretic complications. In fact, the solution of the formal Reggeon diagram problem has led us to the realization that the anomaly enters just in the helicity-flip vertices. In our new development the anomaly plays a straightforward infrared role (although ultraviolet regularization is still involved). As a result, it is clear that the infrared divergence phenomenon we have been searching for is [when the gauge symmetry is broken to SU(2)] a very simple overall ''volume'' divergence directly related to confinement. Although the global picture we presented in our previous papers reemerges, the details are different in very important ways.

RFT is not a conventional field theory. It is really just a

diagrammatic technique set in field-theoretic language [2]. Since it has a non-Hermitian interaction, it is not apparent that there is any kind of ''vacuum state'' in the theory. As a result, the physical meaning of a ''vacuum expectation value'' for the Pomeron field, together with the consequent ''vacuum production of Pomerons,'' has always been particularly elusive. This was, at least partially, responsible for the disagreement about the nature of the supercritical phase [12]. The Pomeron field effectively describes the ''wee-particle'' distribution in a scattering hadron. Therefore it is natural that a vacuum expectation value for this field could be associated with a zero-mode contribution in the light-cone language and so represent nontrivial vacuum properties of the underlying theory. If this is the case, then the physical context for our supercritical solution, which does involve a Pomeron vacuum expectation value, is an underlying theory with a nontrivial vacuum. In particular, an understanding of the QCD Pomeron may be essential. (Technically, it is the presence of helicity-flip vertices containing the anomaly which provides a meaning for Reggeon vacuum production.) Since this was certainly not available at the time of the controversy concerning the nature of the supercritical phase, it is, perhaps, not surprising that the issue remained unresolved. Conversely, as we will see is indeed the case, the supercritical Pomeron may be a valuable high-energy formalism for describing the role of the vacuum properties of QCD.

In this first paper we will concentrate on the development and application of the *S*-matrix technical machinery that is the basis for our arguments. As we noted above, we want to reserve all field-theoretic discussion of the interpretation and significance of our results for the second paper. For the purposes of this paper, we could even define QCD as the massless limit of a theory of massive, Reggeized, vector particles (gluons) with SU(3) quantum numbers, whose interactions satisfy (Reggeon) Ward identities as a condition of gauge invariance and which couple to quarks with the usual vector interaction. In practice, though, we will use Feynman diagrams as a direct tool to construct the Reggeon interactions we discuss. The infrared problems we consider involve taking a subset, or all of, the gluon masses to zero and also taking the quark mass to zero. Since the solution of Reggeon unitarity by Reggeon diagrams is an infrared approximation, a (gauge-invariant) transverse momentum cutoff is always implicitly present in our analysis. Consequently, we could [1,11] specifically formulate our discussion in terms of the Higgs mechanism for spontaneous symmetry breaking and appeal to complimentarity [13] to justify using the massless limit to define QCD. However, for this first paper, we will minimize references to specific field-theoretic assumptions that could be made since, in our experience, this often serves only to confuse the reader as to the issues involved.

For related reasons, we will reserve discussion of a number of topics for the second paper. These include chiral symmetry breaking, the quark bound-state spectrum, deep-inelastic diffractive scaling violations, the implications for perturbative QCD and the parton model, the RFT formulation of both the supercritical Pomeron and the critical Pomeron, the restoration of full SU(3) symmetry, and the dependence on the quark flavor spectrum. Our aim in this paper is to simply expose the infrared massless quark problem related to the anomaly and to show, in a self-contained manner, that this leads to a confining solution of partially broken QCD. We will identify all the elements of supercritical Pomeron behavior, but as we just implied, we will not discuss the RFT formulation in any detail.

II. OUTLINE OF THE ARGUMENTS

If a theory is ''Reggeized,'' that is, if all the particles lie on Regge trajectories, it is not unreasonable to expect that the full *S* matrix is then determined by the corresponding tree diagrams. If all the multiparticle amplitudes containing the poles due to the stable particles of the theory can be found, Reggeization should imply that there is no subtraction ambiguity in constructing the full amplitudes of the theory dispersively via unitarity. (In practice, there is no formulation of such a program, although recent ''unitarity-based'' calculations [14] of loop amplitudes in QCD and supersymmetric gauge theories partially illustrate the principle. The loop expansion for string theories is perhaps an illustration of the essence of the argument.) Reggeization also implies that the tree amplitudes can be found by studying the behavior of all multiparticle amplitudes in multi-Regge limits. The leading Regge pole trajectories in each quantum-number *t* channel are directly associated with a corresponding particle (or resonance), and at the particle poles, Regge pole amplitudes give the corresponding particle amplitudes. Since QCD is believed to be a bound-state theory in which all the particle states lie on Regge trajectories, studying multi-Regge limits should be a direct way to study the particle spectrum.

In the vacuum quantum-number *t* channel, however, the leading Regge pole is the Pomeron. The Pomeron is even signature and probably (in our view) has no particles on its trajectory. The Pomeron determines, in particular, the high-energy elastic scattering amplitudes of the particles in the theory. In this and the following paper, we will see that we can extract both the particle spectrum and the high-energy amplitudes that correspond to the Pomeron by studying multi-Regge limits.

During the period that quantum field theory was out of vogue, very extensive analyticity methods were developed [10,15] to study multi-Regge behavior and its interrelation with unitarity. The analyticity domains for multiparticle amplitudes derived within the formalisms of ''axiomatic field theory'' and ''axiomatic *S*-matrix theory'' were the basis for this abstract analysis. All the assumptions made within these formalisms are expected to be valid perturbatively in a completely massive spontaneously broken gauge theory, and as we discussed in the Introduction, the *S* matrix of such a theory can be thought of as the starting point for our analysis of QCD.

The abstract formalism remains little known and so in Sec. III we both summarize and develop the contents of our previous papers [10]. We emphasize those results required for the rest of the paper. The most important point, which we do not elaborate on explicitly in this paper, is that there are relatively simple, many-variable, domains of analyticity in the multi-Regge asymptotic regime and corresponding mul-

tiparticle dispersion relations are valid. Consequently, generalized ''Sommerfeld-Watson representations'' exist which imply that all multiparticle asymptotic behavior is strongly constrained by ''cross-channel'' multiparticle unitarity continued in complex angular momenta and helicity variables. These constraints are embodied in the general ''Reggeon unitarity equations,'' which hold in every complex angular momentum and helicity plane and control multi-Regge exchanges in all amplitudes. These equations were first proposed in [16]. At the time they were a remarkable ''all-orders'' generalization of results found in lowest-order field theory models of Regge cut behavior. However, the full dispersion theory basis for multi-Regge theory had to be developed before the validity and generality of the Reggeon unitarity equations could be established [10]. Given the Reggeization of gluons and quarks, the (essentially) factorizing nature of the Reggeon unitarity equations implies the very powerful consequence that the multi-Regge behavior of all QCD multiparticle amplitudes is built up from elementary components, many of which are already known from existing calculations of elastic scattering production processes.

In Sec. IV we apply the general formalism of Sec. III to the special case of triple-Regge kinematics. For our purposes, it is important that the conventional ''triple-Regge'' limit of the one-particle inclusive cross section is only the simplest kinematical situation in which triple-Regge behavior appears. We show that in the full triple-Regge limit and also in what we term a helicity-flip helicity-pole limit, new ''helicity-flip vertices'' appear. These vertices are generated by amplitudes with distinctive combinations of invariant cuts. We also formulate the additional limits in terms of large light-cone momenta. This is important in Sec. V for building up the very complicated multi-Reggeon diagrams that we use in later sections.

The initial discussion in Sec. V is concerned with the similarity between RFT Pomeron diagrams and the Reggeon diagrams that describe Regge limit calculations in QCD. Both sets of diagrams can be regarded as explicit solutions of the Reggeon unitarity equations. The remainder of the section is devoted to the task of constructing the Reggeon diagrams that in QCD will contain the bound-state hadron and Pomeron behavior that we are looking for. The essential point is that in a general class of limits, which we call ''maximal helicity-pole limits,'' only a single analytically continued multiparticle partial-wave amplitude appears, related to a leading-helicity particle amplitude. Such partial-wave amplitudes straightforwardly satisfy Reggeon unitarity equations in each t channel and, as a result, have a Reggeon diagram description in terms of two-dimensional transverse momentum integrals. We show, however, that when a helicity-flip vertex is involved the reduction to transverse momentum integrals is more subtle. In this case, if a light-cone description of the limits is formulated, a correlated lightlike vector is necessarily part of the ''physical transverse plane.'' This longitudinal component vanishes with the corresponding transverse momentum.

We begin our QCD analysis in Sec. VI. We show first how elementary quark-Reggeon couplings are obtained by calculating successive on-shell scatterings of fast quarks. We then discuss the derivation of Reggeon Ward identities from gauge invariance gluon Ward identities. We show that quark scattering Reggeon diagrams have infrared divergences and trace the related failure of Reggeon Ward identities to the restricted Regge limit kinematics of on-shell elastic scattering. After discussing how the Reggeon Ward identities are satisfied in high-order Reggeon interactions, we note that there is an ultraviolet divergence problem in the quark loops contributing to triple-Regge vertices. To obtain the Reggeon Ward identities for massive quark loops, it is necessary to introduce Pauli-Villars regulator fermions. These provide a unitarity-violating ultraviolet cutoff in the quark sector, which we ultimately remove only after the massless quark limit is taken.

In Sec. VII we show how the triangle quark loop diagram appears in triple-Regge helicity-flip vertices coupling multi-Reggeon states. We show that the presence of the triangle singularity leads to a nonuniformity in the massless and zero-transverse-momentum limits for such vertices. We identify the momentum and color structure of this ''anomaly.'' As we discuss, it is essentially the infrared appearance of the U(1) axial anomaly. Its appearance in Reggeon diagrams is a subtle effect, related to the presence of nonlocal infrared axial-like couplings for multi-Reggeon states. We show that anomalous color parity Reggeon states (with distinct color parity and signature) must be involved.

The infrared divergence phenomenon producing confinement is described in Sec. VIII. We show that in the limit of zero quark mass the triangle anomaly, combined with the Pauli-Villars regularization procedure, leads to the violation of Reggeon Ward identities in a complicated set of Reggeon diagrams. In such diagrams helicity-flip interactions of anomalous Reggeon states accompany the nonflip interactions of normal Reggeon states. We argue that the resulting logarithmic divergence cancels in the sum of such diagrams when the gauge symmetry is unbroken. However, when the gauge symmetry of QCD is partially broken to SU(2), the divergence does not cancel, but rather selects the ''physical amplitudes.'' The physical states we identify contain massive SU(2) singlet Reggeons with a zero-momentum anomalous odderon component that acts like a background wee-parton component or ''Reggeon condensate.'' We show that we have a ''confinement phenomenon'' in that two initial physical Reggeon states states scatter only into arbitrary numbers of the same physical states. We also have confinement in the sense that, in the gluon sector, we have only massive Reggeon states composed of elementary Regge pole constituents. We postpone discussion of the quark states and chiral symmetry breaking until the next paper.

It is presumably important that because the zero transverse momenta in the Reggeon condensate are implicitly accompanied by longitudinal zero momenta, the condensate can potentially be understood as a zero-mode effect in light-cone quantization and as a wee-parton component at infinite momentum. We summarize our confining solution of partially broken QCD as containing exchange-degenerate even- and odd-signature Reggeons together with vacuum production of multi-Reggeon states. These are the defining characteristics of supercritical Pomeron RFT.

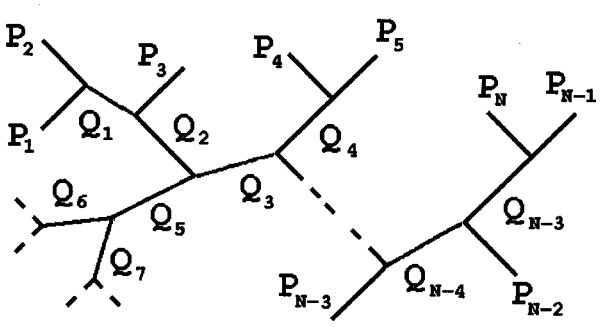

FIG. 1. Toller diagram for the N-point amplitude.

III. MULTI-REGGE LIMITS AND REGGEON UNITARITY

In this section we describe the general multi-Regge theory that will underly the analysis and arguments of this paper. In many cases a more extensive discussion of the subjects we cover can be found in [10] and a very useful background review is provided by [17]. However, as we noted in the previous section, we will also need additional elements that were not adequately described in [10]. We first describe the general kinematics and partial-wave analyses which are the basis of multi-Regge theory.

A. Toller diagrams and little group variables

To describe the most general Regge behavior of a multiparticle amplitude, we first introduce a set of angular variables. For a given amplitude, there are many possible sets, each associated with a distinct Toller diagram. A Toller diagram is simply a tree diagram with only three-point vertices.

Denoting the external momenta for an N-point amplitude by P_i, $i=1,\ldots,N$, we begin by drawing a Toller diagram and introducing internal momenta Q_j, $j=1,\ldots,N-3$, for each internal line of the diagram as illustrated in Fig. 1. The Q_j are defined by imposing momentum conservation at each vertex. Next, we introduce three standard Lorentz frames at each vertex, in each of which one of the three momenta entering the vertex has a standard form, chosen according to some convention. We then denote as g_j the Lorentz transformation—associated with the internal line j—which transforms between the two standard frames, in which Q_j has the standard form, defined, respectively, at the two vertices to which the line j is attached. Since Q_j has the same form, say, Q_j^0, in both standard frames, g_j necessarily belongs to the little group of Q_j^0, implying that

$$g_j \in \mathrm{SO}(2,1) \quad \text{if } Q_j \text{ is spacelike},$$

$$g_j \in \mathrm{SO}(3) \quad \text{if } Q_j \text{ is timelike}. \tag{3.1}$$

We also introduce the Lorentz transformations ζ_{jk} transforming between the standard frames defined for Q_j and Q_k, respectively, at the same vertex. Note that ζ_{jk} is a function of $t_j=Q_j^2$, $t_k=Q_k^2$, and $t_l=(Q_j+Q_k)^2$ only. We can clearly combine the g_j and ζ_{jk} (together with ζ_{ij} transformations defined analogously to the ζ_{jk}, but at external vertices) to determine any of the external momenta in any of the standard frames associated with the Toller diagram. For an N-point amplitude M_N, we can therefore write

$$M_N(P_1,\ldots,P_N) \equiv M_N(t_1,\ldots,t_{N-3},g_1,\ldots,g_{N-3}). \tag{3.2}$$

If we initially consider all the Q_j to be timelike, then we can use the SO(3) parametrization

$$g=u_z(\mu)u_x(\theta)u_z(\nu), \quad 0\leqslant\theta<\pi, \quad 0\leqslant\nu,\mu\leqslant 2\pi, \tag{3.3}$$

where u_z and u_x are, respectively, rotations about the z and x axes. We can also take all the ζ_{jk} and ζ_{ij} to be boosts $a_z(\zeta)$ in the z-t plane. In this case the u_z rotations clearly commute with the a_z, and as a result, the external invariant variables depend only on combinations $w_{jk}=\mu_j-\mu_k$ of azimuthal angles. The net effect is that the angular variables for each Toller diagram reduce always to the $(3N-10)$ independent variables needed to describe an N-point amplitude. There are always

$$\left.\begin{array}{ll} (N-3) & t_i \text{ variables } (\equiv Q_i^2) \\ (N-3) & z_j \text{ variables } (\equiv \cos\theta_j) \\ (N-4) & u_{jk} \text{ variables } (\equiv e^{i\omega_{jk}}) \end{array}\right\} (3N-10) \quad \text{variables}. \tag{3.4}$$

For each Toller diagram the t_j, z_j, and u_{jk} variables are an unconstrained Lorentz-invariant set of variables for an N-point amplitude.

We will also make use of two parametrizations of SO(2,1). The first corresponds directly to the SO(3) parametrization (3.3) (with $\cos\theta\to\cosh\beta$), i.e.,

$$g=u_z(\mu)a_x(\beta)u_z(\nu), \quad -\infty<\beta<\infty, \quad 0\leqslant\mu,\nu\leqslant 2\pi, \tag{3.5}$$

where a_x is now a boost in the x-t plane. An alternative parametrization is

$$g=u_z(\mu)a_x(\beta)a_y(\gamma), \quad -\infty<\beta,\gamma<\infty, \quad 0\leqslant\mu\leqslant 2\pi. \tag{3.6}$$

B. Invariants and angular variables

A general multi-Regge limit is defined, via a particular Toller diagram, as

$$z_1,z_2,\ldots,z_{N-3}\to\infty, \quad \forall t_i,u_{jk} \quad \text{fixed}. \tag{3.7}$$

A variety of ''helicity-pole limits'' in which some combination of the z_j and u_{jk} variables is taken as large can also be discussed. The reason for the helicity-pole name will be clear after we introduce Sommerfeld-Watson representations. ''Maximal helicity-pole limits'' in which (in a sense we will discuss later) the maximum number of u_{jk} variables are taken large will play an important role in our discussion. The significance of maximal helicity-pole limits is that they can be used to isolate a single, analytically continued, ''helicity amplitude.'' A multi-Regge limit, in general, has contributions from many different helicity amplitudes.

It is straightforward to calculate the behavior of channel invariants in terms of the angular variables. An explicit ex-

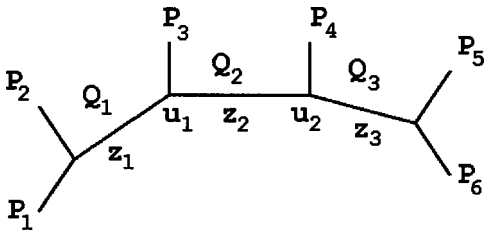

FIG. 2. Toller diagram for the six-point amplitude.

ample, the six-point amplitude and the angular variables corresponding to the Toller diagram of Fig. 2, can be found in the Appendix of [15]. The parametrization (3.5) is used and the specific standard frames are essentially those we have described. We can also list a few of the most important features that appear in general.

(A) If we write $z_j=\frac{1}{2}(v_j+v_j^{-1})$ (i.e., $v_j=e^{i\theta_j}$) and define u_{jk} as above, then all factors of i in expressions for invariants (coming from $\sin\theta_j$ and $\sin\omega_{jk}$) cancel. The relation between all invariants and the u's and v's is real and analytic.

(B) When all the z_j's are large (or all the v_j's), we obtain, for $s_{mn}=(p_m+p_n)^2$,

$$s_{mn}\sim\sinh\zeta_{mj_1}v_{j_1}(\cosh\zeta_{j_1j_2}+\cos\omega_{j_1j_2})v_{j_2}\cdots v_{j_{r-1}}\times(\cosh\zeta_{j_{r-1}j_r}+\cos\omega_{j_{r-1}j_r})v_{j_r}\sinh\zeta_{j_rn}, \quad (3.8)$$

where $j_1,j_2,\ldots,j_s$ is the set of internal lines of the tree diagram linking the two external momenta. As a result, for any invariant $s_{mn\cdots r}=(p_m+p_n+\cdots+p_r)^2$, we obtain

$$s_{mn\cdots r}\underset{z_j\to\infty\forall_j}{\sim} f(\underline{t},\underline{\omega})z_{j_1}z_{j_2}\cdots z_{j_s}, \quad (3.9)$$

where now $j_1,j_2,\ldots,j_s$ denotes the longest path through the tree diagram linking any two of the external momenta contained in $s_{mn\cdots r}$.

(C) When all the u_{jk}'s are large, we similarly obtain

$$s_{mn}\sim\sinh\zeta_{mj_1}\sin\theta_{j_1}u_{j_1,j_2}(\cos\theta_{j_2}+1)u_{j_2,j_3}\cdots u_{j_{r-2},j_{r-1}}\times(\cos\theta_{j_{r-1}}+1)u_{j_{r-1},j_r}\sin\theta_{j_r}\sinh\zeta_{j_rn}. \quad (3.10)$$

Again, the leading behavior of any $s_{mn\cdots r}$ is obtained from the two particles linked by the longest path through the tree diagram.

It is important, although we will make little reference to it, that the singularities of amplitudes as functions of the invariant variables have a similar asymptotic structure in terms of either the z_j variables or the u_{jk} variables.

C. Hexagraphs, direct channels, and cross channels

While the Toller diagram is sufficient to introduce angular variables, there are many analytic and kinematic properties of amplitudes for which it is very useful to introduce a further set of related ''tree diagrams'' called ''hexagraphs.'' There are many hexagraphs for each Toller diagram.

A hexagraph is necessarily drawn in a plane. It has the same number of vertices as the parent Toller diagram, but each internal line of the Toller diagram is replaced by a line containing both horizontal and sloping elements. The complete set of hexagraphs corresponding to a Toller diagram is constructed as follows.

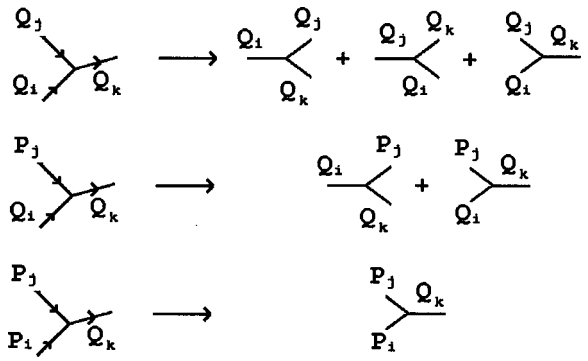

FIG. 3. Hexagraph vertices from Toller diagram vertices.

We begin by substituting for each of the vertices of the Toller diagram the sets of vertices shown in Fig. 3, in each of which one of the Q_i is attached to a horizontal line. (As illustrated, the number of vertices substituted depends on the number of external lines entering the vertex.) We next join the available vertices with horizontal lines in all possible manners, forming projections on the plane. From the set of graphs obtained, we generate further graphs by ''twisting'' each graph about each internal horizontal line. Twisting rotates all of that part of the graph attached to one end of the horizontal line by 180° relative to the remainder of the graph—turning it upside-down in the plane. We continue ''twisting'' until no new graphs are obtained.

Examples of hexagraphs obtained from the Toller diagram of Fig. 1 are shown in Fig. 4. One use of a hexagraph is to generalize the elastic scattering concepts of the ''s-channel,'' or ''direct-channel,'' physical region and the ''t-channel,'' or ''cross-channel,'' physical region. Each hexagraph simultaneously describes an ''s-channel'' physical region in which all the Q_i of the Toller diagram are spacelike and a ''t-channel'' physical region in which all the Q_i are timelike. (Of course, there are also additional channels in which some Q_i are timelike and some are spacelike, but we will not discuss them specifically.) The direct channel is obtained by interpreting the diagram as describing scattering particles entering from the bottom of the diagram and exiting at the top. The cross channel is obtained by interpreting the diagram as describing scattering particles entering from the left of the diagram and exiting to the right. (Since we do not consider scattering processes as distinct that differ by an overall CPT transformation, we do not consider hexagraphs as distinct that differ only by the complete vertical, or horizontal, reflection corresponding to a CPT transformation of the corresponding direct channel or cross

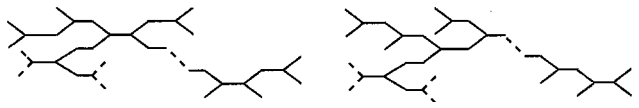

FIG. 4. Examples of hexagraphs obtained from the Toller diagram of Fig. 1.

channel. As a result, it is irrelevant whether the scattering particles enter from the bottom or top in the direct channel or whether they enter from the left or right in the cross channel.) Note that the same cross channel is described by a class of distinct direct-channel hexagraphs related by ''twisting.'' As we describe further below, the process of twisting a hexagraph about a horizontal line defines the multiparticle generalization of signature.

The angular variables can be straightforwardly introduced in any physical region by the procedure described in Sec. III A. In a cross channel,

$$t_j \geqslant 4m^2, \quad -1 \leqslant z_j \leqslant 1, \quad -1 \leqslant \cos\,\omega_{jk} \leqslant 1. \quad (3.11)$$

For a direct channel the situation is more complicated. Even if all the Q_j meeting at a vertex are spacelike, the vertex may lie in either a spacelike or a timelike plane [i.e., $\lambda(t_i,t_j,t_k) \leqslant 0$, where $\lambda(t_i,t_j,t_k)=t_i^2+t_j^2+t_k^2-2t_it_j-2t_jt_k-2t_kt_i$]. In that part of a direct channel in which all the Q_j are spacelike and all the internal vertices are timelike,

$$t_j<0, \quad z_j \geqslant 1 \text{ or } \leqslant 1, \quad -1 \leqslant \cos\omega_{jk} \leqslant 1. \quad (3.12)$$

In this kinematic configuration, the multi-Regge limit is a physical limit, but a helicity-pole limit is unphysical. For those parts of a direct channel where a vertex is spacelike, the physical region is parametrized by the ω_{jk} angles becoming boosts as in Eq. (3.6). In this case both Regge and helicity-pole limits are physical region limits.

We will use hexagraphs to describe more and more information as we proceed. In particular, we can associate each θ_j and each t_j with the corresponding horizontal line of the hexagraph, while the independent ω_{jk} can always be associated (in an obvious manner) with the internal sloping lines. (This association can also be made for the conjugate J_j, n_k, and n_k' variables that we introduce below. It will be illustrated in Fig. 5.) We can then associate a ''twist'' about a horizontal line of a hexagraph with a change of sign of the corresponding z_j and also, for a sloping line attached directly to this line (not via a vertex), with a change of sign of the corresponding u_{jk}. This is how twisting is used in defining signature.

D. Partial-wave expansions

In a cross channel all the little groups are SO(3). For a general function $f(g)$ on SO(3), we can write

$$f(g)=\sum_{J=0}^{\infty} \sum_{|n|,|n'|<J} D^J_{nn'}(g)\,a_{J_{nn'}}, \quad (3.13)$$

where the $D^J_{nn'}(g)$ are representation functions. For the parametrization (3.3),

$$D^J_{nn'}(g)=e^{in\mu}d^J_{nn'}(\theta)e^{in'\nu}, \quad (3.14)$$

where the $d^J_{nn'}(\theta)$ are well-known special functions. From Eq. (3.2) we can write

$$M_N(\underset{\sim}{t},g_1,\ldots,g_{N-3})=\sum_{J_1=0}^{\infty} \sum_{|n_1|,|n_1'|<J_1} \cdots \sum_{J_{N-3}=0}^{\infty} \sum_{|n_{N-3}|,|n_{N-3}'|<J_{N-3}} D^{J_1}_{n_1n_1'}(g_1)\cdots D^{J_{N-3}}_{n_{N-3},n_{N-3}'}(g_{N-3}) \times a_{J_1,n_1,n_1',\ldots,J_{N-3},n_{N-3},n_{N-3}'}(\underset{\sim}{t}). \quad (3.15)$$

Since, as we have discussed, each M_N depends only on combinations of the azimuthal angles μ_j and ν_j, there is a related constraint on the sums over n_j and n_j' in Eq. (3.15). With the particular convention that, at the vertex where lines j,k,l meet, the Lorentz transformations g_j,g_k,g_l are defined to transform from this particular vertex to adjacent vertices, this constraint takes the form

$$n_j+n_k+n_l=0. \quad (3.16)$$

After this constraint is imposed there are $(N-4)$ independent n and n' indices in Eq. (3.15) (considering spinless external particles) which are ''conjugate'' to the $(N-4)$ independent azimuthal angles ω_{jk} introduced above. The j, n, and n' variables can be associated with the lines of a hexagraph as illustrated in Fig. 5.

To use the partial-wave expansion to discuss Regge behavior in Regge and helicity-pole limits in direct channels, we first define continuations of the partial-wave amplitudes $a_{J,n,n'}(t)$ to complex values of the angular momenta J_i and the helicities n_i,n_i'. This will enable us to transform (some of) the summations in Eq. (3.15) into integrals via the Sommerfeld-Watson (SW) transformation. For this purpose it is necessary to break the full amplitude M_N down into spectral components containing distinct multiple discontinuities in the invariant variables that are large in the limit discussed. This is achieved by writing an (asymptotic) dispersion relation in the z_j variables. As we noted in Sec. II, the existence of such dispersion relations is actually the fundamental core of our development of multi-Regge theory.

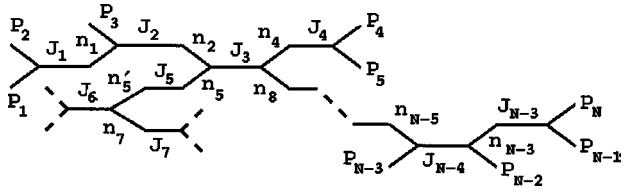

FIG. 5. Association of j, n, and n' indices with the lines of a hexagraph.

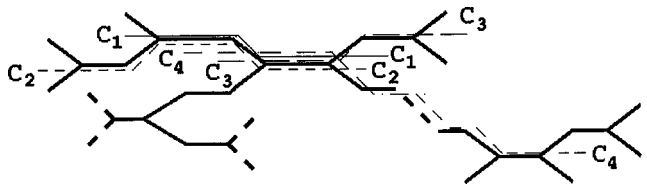

FIG. 6. Allowable cuts through the hexagraph of Fig. 3.

However, since an understanding of their derivation is not necessary for the purposes of this paper, we simply go straight to the result. An extended description of the general derivation can be found in [10], and the particular example corresponding to the Toller diagram of Fig. 2 is discussed in detail in [15].

E. Asymptotic dispersion relations

A primary purpose of the hexagraph notation is to describe the spectral contributions to the asymptotic dispersion relation, for an amplitude M_N, obtained by simultaneously dispersing in all the z_j variables of the parent Toller diagram. By introducing the concept of a ''cut'' through a hexagraph, we can use such cuts to describe invariant channels in which there is a discontinuity or ''cut.'' For each hexagraph we define an ''allowable'' direct-channel discontinuity to be in any subchannel, defined by a subset of the external particles, such that the minimal ''cut'' drawn through the graph connecting all the particles involved enters and exits only between a pair of sloping lines. Some allowable cuts of the upper hexagraph in Fig. 4 are shown in Fig. 6.

The asymptotic dispersion relation takes the form

$$M(p_1,\ldots p_N)=\sum_{H\in T} M^H(p_1,\ldots,p_N)+M^0, \qquad (3.17)$$

where the sum is over all hexagraphs H generated by the Toller diagram T and M^0 contains only nonleading multi-Regge behavior. Each ''hexagraphical component'' M^H is further written as

$$M^H=\sum_{C\in H} M^C(p_1,\ldots,p_N), \qquad (3.18)$$

where now the sum is over all sets C of $(N-3)$ nonoverlapping cuts which are (all) allowable cuts of the hexagraph. (In the simplest graphs there will be only one set C). The $(N-3)$ cuts must be ''asymptotically distinct'' when all the z_j variables are large. If we denote the invariant cuts of a particular set C as $(s_1,\ldots,s_{N-3})$, then

$$M^C(p_1,\ldots,p_N) = \frac{1}{(2\pi i)^{N-3}}\int \frac{ds_1'\cdots ds_{N-3}'\Delta^C(\underline{t},\underline{w},s_1',s_2',\ldots,s_{n-3}')}{(s_1'-s_1)(s_2'-s_2)\cdots(s_{N-3}'-s_{N-3})}, \qquad (3.19)$$

where

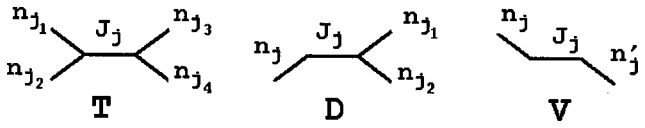

FIG. 7. *T*, *D*, and *V* subgraphs of a hexagraph.

$$\Delta^C(\underline{t},\underline{w},s_1\ldots,s_{n-3}) = \sum_{\epsilon}(-1)^{\epsilon}M(\underline{t},\underline{w},s_1\pm i0,s_2\pm i0,\ldots,s_{N-3}\pm i0). \qquad (3.20)$$

The sum over ϵ is over all combinations of $+$ and $-$ signs in Eq. (3.20) and $(-1)^{\epsilon}$ is positive when the number of $+$ signs is even. In writing Eq. (3.19) the asymptotic relation (3.9) has been used to change variables from $z_1,\ldots,z_{N-3}$ to $s_1,\ldots,s_{N-3}$. We note again that an explicit example of an asymptotic dispersion relation is described in full detail in [15].

F. Froissart-Gribov continuations and signature

Each hexagraph spectral component M^H has simultaneous cuts in only $N-3$ large invariants. As we will see, the invariant cuts are reflected directly in the form that multi-Regge behavior takes. Each cut is associated with a particular power behavior. Correspondingly, the multi-Regge behavior of a spectral component is obtained by SW transforming only $N-3$ of the angular momentum and helicity sums in Eq. (3.15). Indeed, unique Froisart-Gribov (FG) continuations in the complex plane can only be made for the relevant indices. An important property of the hexagraph notation is that it classifies together all those sets of cuts for which continuations in the same helicity and angular momentum variables can be made. The construction of FG continuations is described in detail in [10]. Here we will simply give the rules for determining the continuations that exist for a particular hexagraph amplitude.

We first need to define *T*, *D*, and *V* subgraphs of a hexagraph as in Fig. 7. It is obvious how hexagraphs, such as those of Fig. 4, break up into subgraphs of this form. The continuation rules are that in each V_j we take n_j complex with (J_j-n_j) and (n_j-n_j') held fixed at integer values. In each D_j we take n_j complex with (J_j-n_j) held fixed at an integer value. In each T_j we take J_j complex, independently of all the n_{j_i}. These rules imply that the helicity labels, which are attached to sloping lines of the hexagraph, are always coupled to (that is, differ only by an integer from) the angular momentum associated with the corresponding horizontal line of the hexagraph.

An important point for all continuations is that they are made separately for positive and negative helicities and also for positive and negative helicity differences, that is, for $n_j \gtrless n_j'$ for each V_j, for $n_j \gtrless (n_{j_1}\pm n_{j_2})$ for each D_j, and for $(n_{j_1}\pm n_{j_2}) \gtrless (n_{j_3}\pm n_{j_4})$ for each T_j. We will use a convention in which if n_{j_1} and n_{j_2} have the same sign, this implies they have opposite sign helicities in the t_j-channel center of

mass. (In a direct channel this would correspond to helicity sign conservation.) Continuations from values of n_{j_1} and n_{j_2} with the opposite sign will be referred to as ''helicity-flip'' continuations and will be crucial in what follows.

As in elementary Regge theory, it is necessary to introduce signature to obtain well-defined FG continuations. In the analytic procedure we are following, signatured amplitudes are obtained by adding or subtracting the dispersion relation spectral components corresponding to those hexagraphs differing simply by a twist, about the corresponding horizontal line for a continuation in a J_j and about the horizontal line to which the corresponding sloping line is attached for a continuation in n_j. This definition also separates ''even'' and ''odd'' terms in the relevant series appearing in the partial-wave expansion. As we described above, a single twist changes the sign of the angular variable (associated with the line about which the twist is made) whose conjugate variable (J_j or n_j) is taken to be complex.

We shall also utilize the following, equivalent, ''group-theoretic'' definition of signature, since in general it is easier to implement. Beginning with an N-point amplitude in a particular direct channel, we form the positive (or negative) signatured amplitude, with respect to a particular internal line of a Toller diagram, by adding (or subtracting) the amplitude obtained by making a complete CPT transformation on all external particles connected (through the diagram) to one end of the internal line. The fully signatured amplitude is formed by carrying out this procedure for all internal lines of the Toller diagram. In this way signature is introduced at the amplitude level without introducing spectral components. It is an operation defined directly on the external states. Although the equivalence of the two definitions has only been proved in the simplest cases, we have no reason to doubt that the equivalence is true in general, and we will assume this to be the case. Of course, to understand the implications of signature for phases, etc., it is necessary to utilize the analytic formulation.

It is interesting to note that, in the case when no V_j's are present in the hexagraph, the total cross-channel angular momentum is continued to complex values, together with all the helicities of (cross-channel) subchannels. In no case is the angular momentum of a subchannel continued separately from the helicity. When V_j's are present the total angular momentum of the cross channel is not used as a variable. Instead, the scattering can be regarded as made up of subprocesses for which the total angular momenta and subchannel helicities are analytically continued.

G. Sommerfeld-Watson representations, and multi-Regge and helicity-pole limit amplitudes

The process of first defining a SW transformation on the partial-wave expansion for a hexagraph amplitude and then studying asymptotic limits is sufficiently complicated that it is difficult to give a general description. We give a general idea of the procedure by considering simple examples. We will study further examples in the following section. As we remarked earlier, we will be particularly interested in ''maximal helicity-pole limits.'' For hexagraphs with no V subgraphs, a maximal helicity-pole limit is simply defined by taking all the azimuthal u_{ij} variables to be large. When a V subgraph is involved, only one combination of the two azimuthal angles associated with the central line of the graph is taken to be large. The maximal number of helicity poles is still involved and a single partial-wave amplitude is isolated.

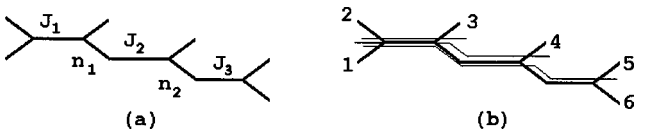

FIG. 8. Hexagraph from the Toller diagram of Fig. 2: (a) J and n variables and (b) cuts.

We consider specifically the Toller diagram for the six-point function shown in Fig. 2. This is the Toller diagram for which the asymptotic dispersion relation is derived in [15]. There are 4 basic hexagraphs which after twisting gives a total of 32 hexagraphs. A full discussion of the SW representation for all the hexagraphs and their use in all asymptotic limits is given in [10]. Here, for illustration, we concentrate on two of the basic graphs. Consider first the hexagraph shown in Fig. 8. With the J and n variables as illustrated, the partial-wave expansion has the form

$$A_H(z_1,z_2,z_3,u_1,u_2,t_1,t_2,t_3) = \sum_{\underset{\sim}{J}\underset{\sim}{n}} d^{J_1}_{0,n_1}(z_1)u_1^{n_1}d^{J_2}_{n_1,n_2}(z_2)u_2^{n_2}d^{J_3}_{n_2,0}(z_3)a_{\underset{\sim}{J}\underset{\sim}{n}}(\underset{\sim}{t}). \tag{3.21}$$

The hexagraph contains one T graph and two D graphs, and the above rules determine that from $n_1,\ n_2>0$ (signatured) FG continuations can be made to complex J_1, n_1, and n_2 in the three complex half-planes:

$$\mathrm{Re}(J_1-n_1)\geqslant 0, \quad \mathrm{Re}(n_1-n_2)\geqslant 0, \quad \mathrm{Re}\ n_2\geqslant 0, \tag{3.22}$$

while J_2-n_1 and J_3-n_2 are held fixed at integer values. For the present we omit the complications of signature in order to more simply illustrate other features. The SW transform of that part of Eq. (3.21) satisfying Eq. (3.22) is then

$$\begin{aligned} A_H=\frac{1}{8}\int_{C_{n_2}}\frac{dn_2u_2^{n_2}}{\sin\pi n_2}\int_{C_{n_1}}\frac{dn_1u_1^{n_1}}{\sin\pi(n_1-n_2)} \\ \times\int_{C_{J_1}}\frac{dJ_1d^{J_1}_{0,n_1}(z_1)}{\sin\pi(J_1-n_1)}\sum_{\substack{J_2-n_1=N_1=0\\ J_3-n_2=N_2=0}}^{\infty} d^{J_2}_{n_1,n_2}(z_2)d^{J_3}_{n_2,0}(z_3) \\ \times a_{N_2N_3}(J_1,n_1,n_2,\underset{\sim}{t})+\sum_{\underset{\sim}{J}\underset{\sim}{n}}^{\sim} d^{J_1}_{0,n_1}(z_1)u_1^{n_1}d^{J_2}_{n_1,n_2}(z_2) \\ \times u_2^{n_2}d^{J_3}_{n_2,0}(z_3)a_{\underset{\sim}{J}\underset{\sim}{n}}(\underset{\sim}{t}), \end{aligned} \tag{3.23}$$

where C_{n_2}, C_{n_1}, and C_{J_1} are parallel to the imaginary axis. The sum $\tilde{\Sigma}$ is over that part of Eq. (3.21) not satisfying Eq. (3.22).

We will show first that the representation (3.23) is sufficient to study the ''maximal helicity-pole limit''

$$z_1, u_1, u_2 \to \infty, \tag{3.24}$$

with z_2 and z_3 (and t_1, t_2, t_3) kept fixed. The cut structure of A_H is straightforwardly represented asymptotically by the SW integrals as follows. Asymptotically, the invariant cuts of Fig. 8(b) appear in the angular variables via

$$\begin{aligned} s_{23} &= (p_2+p_3)^2 \sim z_1, \\ s_{234} &= (p_2+p_3+p_4)^2 \sim y_{12} \\ &\equiv [(z_1^2-1)^{1/2}(z_2^2-1)^{1/2}]u_1, \\ s_{16} &= (p_1+p_6)^2 \sim y_{123} \\ &\equiv [(z_1^2-1)^{1/2}(z_2+1)(z_3^2-1)^{1/2}]u_1 u_2. \end{aligned} \tag{3.25}$$

We can rewrite Eq. (3.23) in the form

$$\begin{aligned} A_H = \int & \frac{dn_2 dn_1 dJ_1}{\sin \pi n_2 \sin \pi(n_1-n_2) \sin \pi(J_1-n_1)} \\ & \times y_{123}^{n_2} y_{12}^{n_1-n_2} P^{J_1-n_1}(z_1) \\ & \times \sum_{N_1,N_2=0}^{\infty} P^{N_1}(z_2) P^{N_2}(z_3) a_{N_1 N_2}(J_1, n_1, n_2 t) \\ & + \tilde{\sum}, \end{aligned} \tag{3.26}$$

where

$$p^{j-n}(z) = \frac{1}{2}(1+z)^{(-n-n')/2}(1-z)^{(n'-n)/2} d^j_{nn'}(z), \qquad n > n', \tag{3.27}$$

is a polynomial for integer $j-n=N$. In the form (3.26), it is clear that each of the asymptotic cuts of A_H is directly represented by one of the SW integrals. Since A_H has no singularities in the remaining variables, the sums over N_1 and N_2 (of polynomials) will be convergent in the asymptotic region.

An asymptotic expansion for the limit (3.24) can be obtained by pulling the J_1, n_1, and n_2 contours to the left in Eq. (3.26), provided positive power singularities are encountered. The $\tilde{\Sigma}$ contribution gives only inverse powers of either u_1 or $u_1 u_2$. (We will not describe the subtleties of introducing second-type representation functions, etc., that are necessary to obtain a true asymptotic expansion.) It can be shown [10] from the analytically continued unitarity equations that the Regge singularities of $a_{N_1 N_2}(J_1, n_1, n_2)$ occur at values of $J_1, J_2 = n_1 + N_1$ and $J_3 = n_2 + N_2$. In particular, if there are Regge poles at $J_1 = \alpha_1$, $J_2 = \alpha_2$, and $J_3 = \alpha_3$, the leading behavior in the limit (3.24) arises from $N_1 = N_2 = 0$. A Regge pole at $J_1 = \alpha_1$, together with ''helicity poles'' at $n_1 = J_2 = \alpha_2$ and $n_2 = J_3 = \alpha_3$, gives

$$A_H \underset{\substack{z_1\to\infty \\ u_2\to\infty \\ u_3\to\infty}}{\sim} \frac{z_1^{\alpha_1-\alpha_2} y_{12}^{\alpha_2-\alpha_3} y_{123}^{\alpha_3} \beta_{00}^{\alpha_1\alpha_2\alpha_3}}{\sin \pi\alpha_3 \sin \pi(\alpha_2-\alpha_3) \sin \pi(\alpha_1-\alpha_2)}. \tag{3.28}$$

Note that this result holds whether or not z_2 and/or z_3 are large. The partial-wave amplitude with $N_1 = N_2 = 0$ is selected provided only that the limit $u_1, u_2 \to \infty$ is taken. The limit is called a ''helicity-pole limit'' because it is controlled (in part) by poles (or more generally singularities) in helicity planes.

The denominator factors in Eq. (3.28) give singularities in the t_i variables that are determined by the consistency of the asymptotic cut structure of A_H with the Steinmann relations. To see this we use Eq. (3.25) to rewrite Eq. (3.28) in the form

$$\begin{aligned} A_H \sim & s_{23}^{\alpha_1-\alpha_2} s_{236}^{\alpha_2-\alpha_3} s_{15}^{\alpha_3} \\ & \times \frac{\beta_{00}^{\alpha_1\alpha_2\alpha_3}}{\sin \pi\alpha_3 \sin \pi(\alpha_2-\alpha_3) \sin \pi(\alpha_1-\alpha_2)}, \end{aligned} \tag{3.29}$$

which implies that, asymptotically,

$$\underset{s_{23}}{\text{disc}}\, A_H \sim \sin \pi(\alpha_1-\alpha_2) A_H, \tag{3.30}$$

$$\underset{s_{236}}{\text{disc}}\, A_H \sim \sin \pi(\alpha_2-\alpha_3) A_H, \tag{3.31}$$

$$\underset{s_{15}}{\text{disc}}\, A_H \sim \sin \pi\alpha_3 A_H. \tag{3.32}$$

Consequently, each discontinuity cancels one of the poles in the α_j variables, and as a result, the triple discontinuity of A_H has no poles in the t_j variables. The Steinmann relations imply this must be the case. The Steinmann relations, which should be valid asymptotically, forbid singularities in overlapping channels.

To obtain a complete asymptotic expansion in the multi-Regge limit

$$z_1, z_2, z_3 \to \infty \tag{3.33}$$

(with u_1 and u_2 kept fixed), we must also SW transform the sums with $n_2 < 0$ and/or $n_1 - n_2 < 0$ in $\tilde{\Sigma}$. If we again pull back the J_1, n_2, and n_1 contours appropriately, we obtain

$$A_H \underset{\substack{z_1\to\infty\\ z_2\to\infty\\ z_3\to\infty}}{\sim} \sum_{N_1,N_2=0}^{\infty} \frac{P^{N_1}(z_2)P^{N_2}(z_3)}{\sin\,\pi\alpha_3 \sin\,\pi(\alpha_2-\alpha_3)\sin\,\pi(\alpha_1-\alpha_2)}$$

$$\times[\beta^{\alpha_1\alpha_2\alpha_3}_{N_1,N_2} z_1^{\alpha_1}(z_2u_1)^{\alpha_2-N_i}(z_3u_2)^{\alpha_3-N_2} + \beta^{\alpha_1(-\alpha_2)\alpha_3}_{N_1,N_2} z_1^{\alpha_1}(z_2u_1^{-1})^{\alpha_2-N_1}(z_3u_2)^{\alpha_3-N_2}$$

$$+ \beta^{\alpha_1\alpha_2-\alpha_3}_{N_1,N_2} z_1^{\alpha_1}(z_2u_1)^{\alpha_2-N_1}(z_3u_2^{-1})^{\alpha_3-N_2} + \beta^{\alpha_1(-\alpha_2)(-\alpha_3)}_{N_1,N_2} z_1^{\alpha_1}(z_2u_1^{-1})^{\alpha_2-N_1}(z_3u_2^{-1})^{\alpha_3-N_2}]$$

$$\sim \frac{z_1^{\alpha_1}z_2^{\alpha_2}z_3^{\alpha_3}}{\sin\,\pi\alpha_3 \sin\,\pi(\alpha_2-\alpha_3)\sin\,\pi(\alpha_1-\alpha_2)} \sum_{N_1=N_2=0}^{\infty} [\beta^{\alpha_1\alpha_2\alpha_3}_{N_1N_2} u_1^{\alpha_2-N_1}u_2^{\alpha_3-N_2} + \beta^{\alpha_1(-\alpha_2)\alpha_3}_{N_1N_2} u_1^{-\alpha_2-N_1}u_2^{\alpha_3-N_2}$$

$$+ \beta^{\alpha_1\alpha_2(-\alpha_3)}_{N_1N_2} u_1^{\alpha_2-N_1}u_2^{-\alpha_3-N_2} + \beta^{\alpha_1(-\alpha_2)(-\alpha_3)}_{N_1N_2} u_1^{-\alpha_2-N_1}u_2^{-\alpha_3-N_2}]. \tag{3.34}$$

In terms of invariants we have the same result as Eq. (3.28), but now the vertex function contains infinite series of (analytically continued) partial-wave helicity amplitudes. This illustrates the close relationship between the u_j dependence and z_j dependence of amplitudes in the asymptotic region which we referred to earlier. It is, as in this example, simply a consequence of the presence of only $(N-3)$ cuts for $(2N-7)$ variables.

By comparing Eqs. (3.28) and (3.34), we see how a (maximal) helicity-pole limit selects a single FG partial-wave amplitude from the infinite series that appears in the multi-Regge limit. This is important because the unitarity properties of a single FG partial-wave amplitude can be straightforwardly studied. Note that the helicity-pole limit (3.24) is not a physical region limit, although for the more complicated hexagraphs studied in later sections, analogous limits will be physical.

Before we discuss the particle-pole properties of Eqs. (3.28) and (3.34), we briefly discuss the SW representation of a second hexagraph associated with Fig. 2. We consider the hexagraph shown in Fig. 9.

The partial-wave expansion of Eq. (3.21) is again appropriate. The hexagraph now contains one V graph and two T graphs, and the above rules determine that from $n_1,n_2>0$ (signatured) FG continuations can be made to complex J_1, J_3, and n_1 in the three complex half-planes

$$\mathrm{Re}(J_1-n_1)\geqslant 0, \quad \mathrm{Re}(J_3-n_2)\geqslant 0, \quad \mathrm{Re}\; n_1\geqslant 0, \tag{3.35}$$

with J_2-n_1 and n_1-n_2 held fixed at integer values. The SW transform of that part of Eq. (3.21) satisfying Eq. (3.35) is then

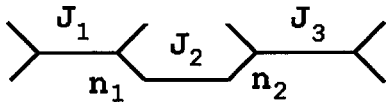

FIG. 9. Another hexagraph from the Toller diagram of Fig. 2.

$$A_H = \frac{1}{8}\int_{C_{n_1}} \frac{dn_1(u_1u_2)^{n_1}}{\sin\,\pi n_1} \int_{C_{J_1}} \frac{dJ_1 d^{J_1}_{0,n_1}(z_1)}{\sin\,\pi(J_1-n_1)}$$

$$\times \int_{C_{J_3}} \frac{dJ_3 d^{J_3}_{n_2,0}(z_3)}{\sin\,\pi(J_3-n_2)} \sum_{\substack{J_2-n_1=N_1=0\\ n_1-n_2=N_2=0}}^{\infty} d^{J_2}_{n_1,n_2}(z_2)$$

$$\times u_2^{n_2-n_1} a_{N_2N_3}(J_1,J_3,n_1,t)$$

$$+ \sum_{\underset{\sim}{Jn}}^{\sim} d^{J_1}_{0,n_1}(z_1) u_1^{n_1} d^{J_2}_{n_1n_2}(z_2) u_2^{n_2} d^{J_3}_{n_2,0}(z_3) a_{\underset{\sim}{Jn}}(\underset{\sim}{t}). \tag{3.36}$$

We now consider the ''maximal helicity-pole limit''

$$z_1,z_3,u_1u_2\to\infty, \tag{3.37}$$

with z_2 and u_1/u_2 fixed. Regge poles at $J_1=\alpha_1$ and $J_3=\alpha_3$ contribute straightforwardly. If we take $N_1=N_2=0$, the Regge pole at $J_2=\alpha_2$ appears as a helicity pole at $n_1=\alpha_2$ and we obtain, in analogy with Eq. (3.28),

$$A_H \underset{\substack{z_1\to\infty\\ u_2\to\infty\\ u_3\to\infty}}{\sim} \frac{z_1^{\alpha_1-\alpha_2}z_3^{\alpha_3-\alpha_2}y_{123}^{\alpha_2}\beta^{\alpha_1\alpha_2\alpha_3}_{00}}{\sin\,\pi\alpha_2 \sin\,\pi(\alpha_1-\alpha_2)\sin\,\pi(\alpha_3-\alpha_2)}. \tag{3.38}$$

Again, a single FG partial-wave amplitude is isolated. Note that Eq. (3.38) continues to hold if z_2 is taken large.

We can use Eqs. (3.28), (3.34), and (3.38) to illustrate some general properties of hexagraph multi-Regge amplitudes. Suppose, for simplicity, that the α_i are even-signature Regge trajectories giving a particle pole at $\alpha_i=0$. We note first that Eq. (3.28) contains a pole only at $\alpha_3=0$. A pole at $\alpha_2=0$ appears if we first set $\alpha_3=0$. In contrast, Eq. (3.38) contains directly a pole at $\alpha_2=0$. As we discussed, the pole structure in the t_i variables relates directly to the analytic structure in the large invariant variables. Together, Eqs. (3.28) and (3.38) represent a general situation in very complicated hexagraphs. Particle poles occur in association with

a V subgraph or with a D subgraph at the end of a ''cascade'' of D subgraphs. Regge pole factorization gives that, in Eq. (3.38),

$$\beta_{00}^{\alpha_1\alpha_2\alpha_3}=\beta_0^{\alpha_1\alpha_2}\beta_0^{\alpha_2\alpha_3}, \tag{3.39}$$

and so, as the hexagraph of Fig. 9 suggests pictorially, at $\alpha_2=0$ the amplitude factorizes into a product of four-point amplitudes. The factorization property (3.39) holds provided only that we pick out a Regge pole in the t_2 channel. In general, we obtain full four-point scattering amplitudes rather than just the Regge exchange amplitudes given by Eq. (3.39). If we continue α_2 to a nonzero even integer value, then the factorization of Eq. (3.39) gives the leading-helicity four-point amplitudes. Analogously, if we continue α_3 to an even integer value in Eq. (3.28), we obtain the leading-helicity amplitude at the particle pole. As illustrated by Eq. (3.34), a multi-Regge limit amplitude in general gives a sum over helicity amplitudes at a particle pole.

Finally, we note that we can also obtain leading-helicity amplitudes with opposite signs for the n_j involved by taking corresponding helicity-pole limits, for example, by taking the limit $u_1/u_2\to\infty$ with u_1u_2 fixed in Eq. (3.36) and by taking $u_2\to 0$ instead of $u_2\to\infty$ in Eq. (3.23).

H. Reggeon unitarity

The most important property of the FG amplitudes is that they can effectively be used to analytically continue, in the complex J_j and n_j planes, the cross-channel multiparticle unitarity equations in any t_i channel of any Toller diagram. This leads to a set of ''Reggeon unitarity'' equations for the discontinuities across multi-Reggeon branch cuts which appear in each of the complex angular momentum planes. These equations are crucial in enabling us to build the multi-Regge behavior of QCD amplitudes on the basis of known results for elastic and production processes. We will only give a brief outline of the derivation of the Reggeon unitarity equations here. (Note that in the abstract analysis of this section and the next section we use ''Reggeon'' to refer to any Regge pole. In Sec. V we will use this term specifically for an odd-signature Regge pole with intercept near 1, referring to an even-signature pole with intercept near 1 as a Pomeron. From Sec. VI onwards a Reggeon will specifically be a Reggeized gluon.)

The discontinuity across the M-Reggeon cut (i.e., the branch cut due to the exchange of M Regge poles) in any J plane is derived most simply from the $2M$-particle discontinuity formula in the corresponding t channel. The t-channel discontinuity is first expressed as a conventional unitarity phase-space integral. By using a Toller diagram including the internal particles, this phase-space integral $I_{2M}(t)$ can be written in the form

$$I_{2M}(t)=i\int d\rho(t,t_1,\ldots,t_j,\ldots)\int dg_J\prod_j dg_j, \tag{3.40}$$

where the g_j are associated with lines of the Toller diagram and (apart from numerical factors)

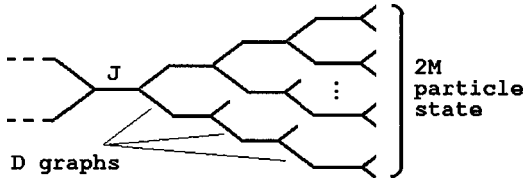

FIG. 10. A ''cascade'' of D graphs for $2M$ particle phase space.

$$\int d\rho(t,t_1,\ldots,t_j,\ldots)$$
$$=\int\prod_j dt_j\,\frac{\lambda^{1/2}(t,t_1,t_2)}{t}\,\frac{\lambda^{1/2}(t_1,t_3,t_4)}{t_1}\cdots$$
$$\times\frac{\lambda^{1/2}(t_j,t_{j+1},t_{j+2})}{t_j}\cdots. \tag{3.41}$$

There is a λ function for each internal vertex, including those involving the internal particles (for which the corresponding ''t_j'' is the mass^2). The integration region is defined by

$$\lambda(t_j,t_{j+1},t_{j+2})\geqslant 0 \quad \forall j. \tag{3.42}$$

It can be shown [10] that the unitarity integral generates Regge cut behavior only when particular multiple discontinuities are present in the amplitudes appearing in the integral. The necessary discontinuities are present when (and only when) the amplitudes correspond to hexagraphs having a ''cascade'' structure of D subgraphs with respect to the internal phase space, as illustrated in Fig. 10. (The subtleties in isolating hexagraph product contributions are discussed in [10]; we will not discuss them here.) As a result, for the purposes of studying Regge cuts, we obtain a form of hexagraph diagonalization of the t-channel $2M$-particle unitarity integral

$$\text{disc}\ A^H=i\int d\rho\int dg\prod_j dg_j A^{H_L}(g,\ldots,g_j,\ldots)$$
$$\times A^{H_R}(g^{-1}g_J,\ldots,g_j,\ldots), \tag{3.43}$$

where H_L and H_R have the necessary cascade structure. For example, if H is the hexagraph shown in Fig. 11, the hexagraphs H_L and H_R have the form illustrated in Fig. 12; i.e., H_L and H_R are formed from H by splitting H in two at the J line and substituting a product of D cascades that connect to the intermediate particle state. Equation (3.43) can then be diagonalized by partial-wave projection, i.e. (suppressing all the external hexagraph angular momenta and helicity labels),

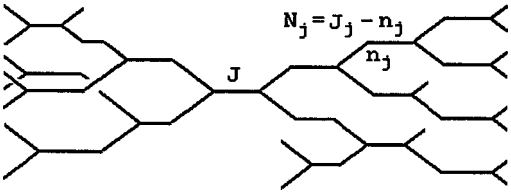

FIG. 11. Hexagraph H.

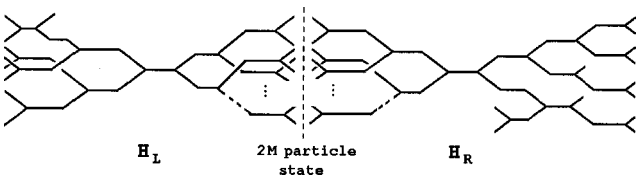

FIG. 12. Product of hexagraphs in the discontinuity formula.

$$\text{disc}\ \ a_J^H = i\int d\rho \sum_{\underset{\sim}{N},\underset{\sim}{n}} a^{H_L}_{J\underset{\sim}{N}\underset{\sim}{n}} a^{H_R}_{J\underset{\sim}{N}\underset{\sim}{n}}. \tag{3.44}$$

The summation shown is over all internal helicity labels n and angular momenta $N=J-n$ of all the D graphs in the phase-space part of H_L and H_R.

The partial-wave equations (3.44) can be analytically continued to complex values of the external angular momenta and helicities by converting the internal sums to integrals having the SW form. The M-Reggeon cut is generated in the analytically continued equations by a combination of M Regge poles, the phase-space boundaries (3.42), and ''nonsense poles'' for each of the D-graph vertices. In the notation of Fig. 5, the nonsense poles are at

$$J_j=|n_j|=n_{j_1}+n_{j_2}-1 \tag{3.45}$$

when n_{j_1} and n_{j_2} are positive or at

$$J_j=|n_j|=-n_{j_1}-n_{j_2}-1 \tag{3.46}$$

when both n_{j_1} and n_{j_2} are negative. If the Regge poles are identical, then the relevant boundary of the phase space is at

$$\sqrt{t_i}=\sqrt{t_j}+\sqrt{t_k}\quad \forall i,j,k. \tag{3.47}$$

This, combined with all the nonsense conditions, gives a trajectory

$$J=\alpha_M(t)=M\alpha(t/M^2)-M+1. \tag{3.48}$$

As we stated earlier, in our notation $-n_{j_2}$ is the helicity in the t-channel center-of-mass frame. It is very important in what follows that there is no nonsense pole contribution from n_{j_1} positive and n_{j_2} negative or from n_{j_1} negative and n_{j_2} positive. (These are not ''nonsense'' states.) Therefore ''helicity-flip'' partial-wave continuations, from opposite-sign n_{j_i} at an internal vertex, do not contribute to the generation of Regge cuts. (We stated earlier that we will refer to amplitudes which have $n_{j_1}=-n_{j_2}$ as ''helicity-flip'' amplitudes. Such amplitudes are ''nonflip'' in the t-channel center of mass. However, for massless particles, helicity is reversed in going from the s to the t channel and so t-channel nonflip amplitudes correspond to s-channel helicity-flip amplitudes. Ultimately, it is s-channel helicity properties that will interest us.)

Consider now the hexagraph H and consider specifically the M-Reggeon cut in the J channel associated with the central T subgraph of Fig. 11. We denote by $a^{H,\underset{\sim}{\tau}\gtrless}_{J\underset{\sim}{N}\underset{\sim}{n}}$ the signatured FG amplitude associated with H. All the helicities that are continued to complex values are now denoted by $\underset{\sim}{n}$, $\underset{\sim}{N}$ denotes all the $N_j=J_j-n_j$ that are kept fixed at integer values, $\underset{\sim}{\tau}=(\tau_J,\ldots,\tau_{n_j},\ldots)$ are the signature labels, with τ_J given by the product of the signatures of the contributing M Reggeons, and $\gtrless$ denotes all the $\gtrless$ labels describing the signs of helicities and helicity differences from which the continuation is made. The discontinuity formula involves the product of nonsense–Regge-pole amplitudes extracted from the FG amplitudes for the hexagraphs H_L and H_R of Fig. 12. The discontinuity formula is then

$$\text{disc}_{\,J=\alpha_M(t)} a^{H,\underset{\sim}{\tau},\gtrless}_{J\underset{\sim}{N}\underset{\sim}{n}} = \xi_M \int d\hat{\rho}\ A^{H_L,\underset{\sim}{\tau},\gtrless}_{\underset{\sim}{\alpha}}(J^+) A^{H_R,\underset{\sim}{\tau},\gtrless}_{\underset{\sim}{\alpha}}(J^-)$$
$$\times \frac{\delta(J-1-\Sigma_{k=1}^M(\alpha_k-1))}{\sin\frac{\pi}{2}(\alpha_1-\tau_1')\cdots\sin\frac{\pi}{2}(\alpha_m-\tau_M')}, \tag{3.49}$$

where $\int d\hat{\rho}$ has the same form as Eq. (3.41) except that only Regge-pole energies are integrated over (the integration over the masses of the pairs of particles has been eliminated by using elastic unitarity). ξ_M is a (relatively complicated) signature factor that we will give simple approximations for in Sec. V $\tau'=(\tau+1)/2$, and $A^{H_L,\underset{\sim}{\tau},\gtrless}_{\underset{\sim}{\alpha}}(J^+)$ is a ''nonsense'' Reggeon scattering amplitude extracted from $a^{H_L,\underset{\sim}{\tau},\gtrless}_{J\underset{\sim}{N}\underset{\sim}{n}}$ and evaluated above the Regge cut at $J=\alpha_M(t)$. Here, $A^{H_L,\underset{\sim}{\tau},\gtrless}_{\underset{\sim}{\alpha}}(J^-)$ is the same amplitude evaluated below the cut.

For the introduction of Pomeron and Reggeon diagrams in Sec. V, it is important that the phase-space integration $\int d\hat{\rho}$ in Eq. (3.49) can be modified by extracting the ''threshold behavior'' of the nonsense amplitudes at the phase-space boundaries (3.47), i.e., at the nonsense point $(n_j-n_{j+1}-n_{j+2})=-1$:

$$A^{H_R,\underset{\sim}{\tau},\gtrless}_{\underset{\sim}{\alpha}}(J,t_1,\ldots,t_j,t_{j+1},t_{j+2},\ldots)$$
$$\underset{\lambda(t_j,t_{j+1},t_{j+2})\to 0}{\sim}\left(\frac{\lambda(t_j,t_{j+1},t_{j+2})}{t_j}\right)^{(n_j-n_{j+1}-n_{j+2})/2}$$
$$\sim\left(\frac{\lambda(t_j,t_{j+1},t_{j+2})}{t_j}\right)^{-1/2}. \tag{3.50}$$

We can then write

$$\int d\hat{\rho}(t,t_1,\ldots t_j,\ldots)\to\int\prod_j dt_j\lambda^{-1/2}(t,t_1,t_2)$$
$$\times\lambda^{-1/2}(t_1,t_3,t_4)\cdots$$
$$\times\lambda^{-1/2}(t_j,t_{j+1},t_{j+2})\cdots. \tag{3.51}$$

A discontinuity formula, essentially the same as Eq. (3.49), also holds in any n_j plane for $a^{H_L,\underset{\sim}{\tau},\gtrless}_{J\underset{\sim}{N}\underset{\sim}{n}}$ except that the hexagraphs H_L and H_R that are involved are obtained by inserting into the j line of H the same cascade structure that appears in Fig. 12. This is illustrated in Fig. 13.

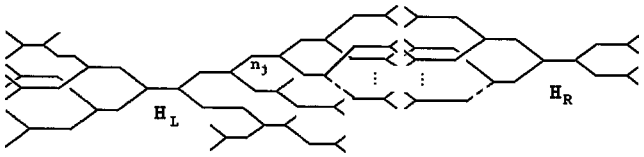

FIG. 13. Another product of hexagraphs.

Similarly, an analogous discontinuity formula to Eq. (3.49) holds in any complex angular momentum or helicity plane for any hexagraph FG amplitude. The hexagraphs involved in the discontinuity formula are simply found by introducing the relevant cascade structures as in Figs. 12 and 13. Before the advent of QCD it was understood that Reggeon unitarity provides a general, model-independent, basis for a Reggeon field theory description of the Pomeron. This will be elaborated on in Sec. V. However, only a limited part of the full set of Reggeon unitarity equations was exploited historically. For the purpose of this paper, the full set of equations (3.17) has another very important role. Extensive results on the Reggeon diagram structure of elastic scattering have been derived by direct calculation within QCD (at leading logarithmic, next-to-leading logarithmic, etc. [5,18,19]). As we will discuss, the power of the Reggeon unitarity formulas is that they can be used to directly extend these results to the multi-Regge behavior of arbitrarily complicated multiparticle scattering amplitudes.

IV. TRIPLE-REGGE VERTICES AND LIMITS

In this section we specialize much of the discussion of the last section to the various ''triple-Regge'' limits of the six-particle amplitude. It is important that triple-Regge kinematics is more general than the well-known case of the large mass limit of the diffractive inclusive cross section. There are ''triple-Regge vertices'' which play a crucial role in our study of QCD, but only appear in the more general triple-Regge and helicity-pole limit kinematics that we discuss below.

A. Hexagraph cuts and limits

We consider the Toller diagram shown in Fig. 14. As in Eq. (3.2), we write

$$M_6(P_1,\ldots,P_6)\equiv M_6(t_1,t_2,t_3,g_1,g_2,g_3). \tag{4.1}$$

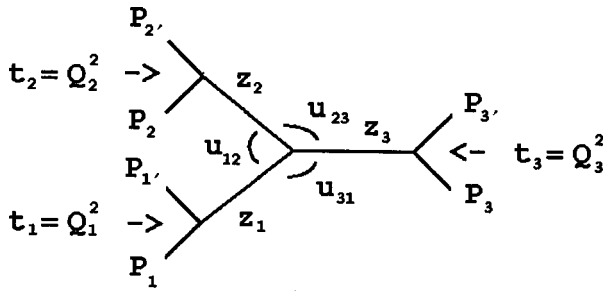

FIG. 14. Toller diagram for M_6.

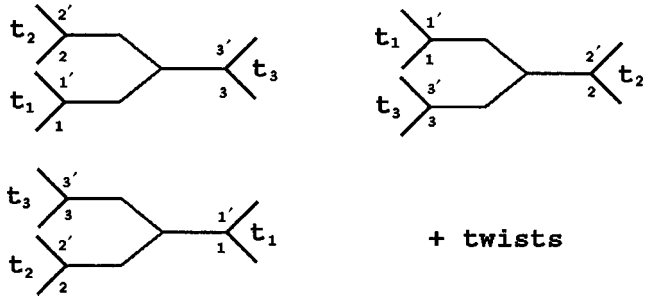

FIG. 15. Hexagraphs associated with the Toller diagram of Fig. 14.

We initially take all the t_i positive so that the g_i are elements of SO(3). We also define each of the g_i to transform from the central vertex to the external vertex. If, for the moment, we take the external particles to be spinless, the amplitude will be independent of the ν_i, $i=1,2,3$, and will depend only on differences of the μ_i. Therefore, if we define

$$u_{12}=e^{i(\mu_1-\mu_2)},\quad u_{23}=e^{i(\mu_2-\mu_3)},\quad u_{31}=e^{i(\mu_3-\mu_1)}, \tag{4.2}$$

then

$$u_{12}u_{23}u_{31}=1 \tag{4.3}$$

and we can take any two as independent variables. Combined with t_1,t_2,t_3 and z_1,z_2,z_3, this gives the appropriate eight independent variables.

The Toller diagram of Fig. 14 generates the set of hexagraphs shown in Fig. 15. Each hexagraph shown is one of $2\times2\times2=8$ related by twisting, where the twists are made about the three horizontal lines in the graphs. There are 24 hexagraphs in total. As we have described in the last section, each hexagraph corresponds to particular sets of allowable triple discontinuities (in direct-channel physical regions where the t_i are negative).

For the first hexagraph of Fig. 15, the allowable sets of cuts are as shown in Fig. 16. The cuts of Fig. 16(a) are in the invariants

$$\begin{aligned} C_1&\equiv s_{2'3'}\quad [=(P_{2'}+P_{3'})^2],\\ C_2&\equiv s_{13}\quad [=(P_1+P_3)^2],\\ C_3&\equiv s_{11'3}\quad [=(P_1-P_{1'}+P_3)^2]. \end{aligned} \tag{4.4}$$

This set of cuts is well known to be related to the one-particle inclusive cross section. The cuts of Fig. 16(b) are in the invariants

$$C_1\equiv s_{2'3'},\quad C_2\equiv s_{13},\quad C_3\equiv s_{123}. \tag{4.5}$$

This second set of cuts is less familiar, but will play an important role in the following. For large s_{12} and fixed s_{23},s_{31},

$$s_{123}=s_{1'2'3'}\sim s_{12}, \tag{4.6}$$

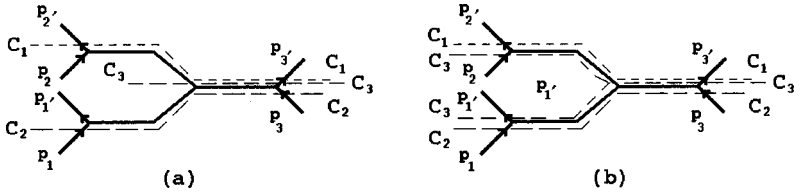

FIG. 16. Hexagraph cuts.

and so, asymptotically, the s_{123} cut can be identified as an s_{12} cut. The Steinmann relations forbid simultaneous cuts in $s_{2'3'}$, s_{31}, and s_{12}. However, we also have $s_{1'2}\sim s_{12'}\sim -s_{12}$, and simultaneous cuts in $s_{2'3'}$, s_{31}, and $s_{1'2}$ are allowed. In the triple-Regge direct-channel physical regions that we are interested in, we cannot have all three of $s_{12'}$, $s_{2'3'}$, and s_{31} positive. Nevertheless, amplitudes with an $s_{1'2}$ cut, in addition to $s_{2'3'}$ and s_{31} cuts, can be regarded as having a left-hand cut in s_{123}, even though it is unphysical, and therefore as having the set of cuts (4.5). This is important for the quark loop amplitudes we discuss in Sec. VII.

The full triple-Regge limit associated with Fig. 14 is the multi-Regge limit of the form (3.7), i.e.,

$$z_1,z_2,z_3\to\infty, \quad t_1,t_2,t_3,u_{31},u_{23} \quad \text{fixed.} \tag{4.7}$$

We can also discuss triple-Regge ''maximal helicity-pole limits'' involving the u_{ij}. Since each hexagraph naturally chooses particular pairs of the u_{ij} as independent variables, it is convenient (and dynamically significant) to associate the helicity-pole limits with particular hexagraphs. For each hexagraph there are two distinct helicity-pole limits.

To discuss the limits associated with the first hexagraph of Fig. 15 we first simplify the notation by writing $u_1\equiv u_{31}$, $u_2\equiv u_{23}$. We can then identify variables with the lines of the hexagraph as illustrated in Fig. 17. The first helicity-pole limit is

$$z_3,u_1,u_2\to\infty \quad (\text{or } u_1,u_2\to 0). \tag{4.8}$$

This is the familiar ''triple-Regge'' limit of the one-particle inclusive cross section. The second helicity-pole limit is

$$z_3,u_1,u_2^{-1}\to\infty \quad (\text{or } u_1u_2^{-1}\to 0). \tag{4.9}$$

For reasons that will soon become apparent, we refer to the first limit as the ''nonflip limit'' and the second as the ''helicity-flip limit.''

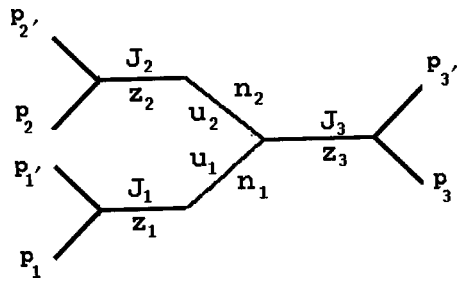

FIG. 17. Hexagraph notation.

From (3B) and (3C) we can see that the following approximations are (essentially) uniformly valid in both helicity-pole limits, as well as the triple-Regge limit (4.7):

$$s_{13}\sim s_{1'3'}\sim -s_{13'}\sim -s_{1'3}\sim z_1z_3(u_1+1/u_1), \tag{4.10}$$

$$s_{23}\sim s_{2'3'}\sim -s_{23'}\sim -s_{2'3}\sim z_2z_3(u_2+1/u_2), \tag{4.11}$$

$$s_{11'3}\sim s_{2'23'}\sim -s_{11'3'}\sim -s_{2'23}\sim z_3, \tag{4.12}$$

$$s_{22'1}\sim s_{3'31'}\sim -s_{22'1'}\sim -s_{3'31}\sim z_1, \tag{4.13}$$

$$s_{33'2}\sim s_{1'12'}\sim -s_{33'2'}\sim -s_{1'12}\sim z_2, \tag{4.14}$$

$$s_{12}\sim s_{1'2'}\sim -s_{12'}\sim -s_{1'2}\sim z_1z_2(u_1/u_2+u_2/u_1). \tag{4.15}$$

Note that all invariants are unchanged when $u_1\to 1/u_1$, $u_2\to 1/u_2$. This is why the limits (4.8) and (4.9) have two equivalent definitions.

B. Special light-cone limits

In later sections it will be useful to have particular realizations of the limits defined in the previous subsection in terms of specific light-cone limits for the momenta involved.

We consider first the triple-Regge limit. Since all three of s_{12}, s_{23}, and s_{31} are large in this limit, P_1, P_2, and P_3 should lie along distinct light cones. In the notation of Fig. 14, we can define a particular version of the the triple-Regge limit, which we call a ''maximally nonplanar'' limit, in which all three momenta are taken to be large and lightlike in orthogonal space directions. We define the following:

L_1,

$$P_1\to P_1^+=(p_1,p_1,0,0), \quad p_1\to\infty,$$

$$Q_1\to q_2-q_3=(0,0,q_2,-q_3),$$

$$P_2\to P_2^+=(p_2,0,p_2,0), \quad p_2\to\infty,$$

$$Q_2\to q_3-q_1=(0,-q_1,0,q_3),$$

$$P_3\to P_3^+=(p_3,0,0,p_3), \quad p_3\to\infty$$

$$Q_3\to q_1-q_2=(0,q_1,-q_2,0). \tag{4.16}$$

(We omit the light-cone components of both the P_i and Q_i that go to zero asymptotically, but are necessary to put both initial and final particles on mass shell.) In terms of invariants, this limit gives

$$s_{12}=(P_1+P_2)^2\to 2p_1p_2,$$

$$s_{23}=(P_2+P_3)^2\to 2p_2p_3,$$

$$s_{31}=(P_3+P_1)^2\to 2p_3p_1,$$

$$s_{122'}=(P_1+Q_2)^2\to 2p_1q_1,$$

$$s_{233'}=(P_2+Q_3)^2\to 2p_2q_2,$$

$$s_{311'}=(P_3+Q_1)^2\to 2p_3q_3, \tag{4.17}$$

and so can be identified with a triple-Regge limit of the form (4.7) in which

$$p_1\sim z_1,\quad p_2\sim z_2,\quad p_3\sim z_3. \tag{4.18}$$

This particular version of the triple-Regge limit illustrates how the limit makes maximal use of four-dimensional Minkowski space. To obtain exactly the above momentum configuration, we clearly have to choose particular values of the u_i and also go to a particular Lorentz frame.

Next, we give some different realizations of the ''helicity-flip'' helicity-pole limit (4.9). The essential feature of this limit, compared to the triple limit, is that, because z_1 and z_2 remain finite, invariants such as $s_{33'1}$ and $s_{33'2}$ remain finite. We first define a limit L_2, in which the finiteness of $s_{33'1}$ and $s_{33'2}$ is very simply achieved. In this limit P_1 and P_2 lie in the same plane, but have opposite space momenta, and this plane is orthogonal to the transverse plane in which Q_3, Q_2, and Q_1 lie. We define the following:
L_2,

$$P_1\to P_1^+=(p_1,p_1,0,0),\ \ p_1\to\infty,$$

$$Q_1\to q_2-q_3=(0,0,q_2,-q_3),$$

$$P_2\to P_2^-=(p_2,-p_2,0,0),\ \ p_2\to\infty,$$

$$Q_2\to q_3-q_2'=(0,0,-q_2',q_3),$$

$$P_3\to P_3^+=(p_3,0,0,p_3),\ \ p_3\to\infty,$$

$$Q_3\to q_2'-q_2=(0,0,q_2'-q_2,0). \tag{4.19}$$

In terms of invariants, this limit gives

$$s_{12}\to 4p_1p_2,\quad s_{23}\to 2p_2p_3,\quad s_{31}\to 2p_3p_1,$$

$$s_{122'}\not\to\infty,\quad s_{233'}\not\to\infty,\quad s_{311'}\to 2p_3q_3. \tag{4.20}$$

Comparing with Eqs. (4.9) and (4.10)–(4.15), we see that this limit can be identified with the ''helicity-flip'' helicity-pole limit (4.9), with

$$p_1\sim u_1,\quad p_2\sim u_2^{-1},\quad p_3\sim z_3. \tag{4.21}$$

Again, special values of the nonasymptotic angular variables (in this case z_1 and z_2) are implicitly involved. However, we will see in the next subsection that, in the leading asymptotic behavior, the dependence on these variables is determined by the SW representation, as it was for the helicity-pole limit (3.28). (For the triple-Regge limit the dependence on the finite angular variables is expanded in infinite partial-wave series and therefore is unknown.)

The following alternative realization of the helicity-flip limit will also be useful. In this case the finiteness of $s_{22'1}$ and $s_{33'2}$ is more subtle. We define the following:
L_2',

$$P_1\to P_1^+=(p_1,p_1,0,0),\quad p_1\to\infty,$$

$$Q_1\to q_2-q_3=(-q_3,-q_3,q_2,-q_3),$$

$$P_2\to P_2^+=(p_2,0,0,p_2,),\quad p_2\to\infty,$$

$$Q_2\to q_3-q_2'=(q_3,q_3,-q_2',q_3),$$

$$P_3\to P_3^-=(p_3,-p_3,0,0),\quad p_3\to\infty,$$

$$Q_3\to q_2'-q_2=(0,0,q_2'-1_2,0). \tag{4.22}$$

The behavior of invariants is essentially identical to Eqs. (4.20). At first sight, the roles of P_2 and P_3 are simply interchanged in going from L_2 to L_2'. However, the crucial difference is that in Eqs. (4.22) the ''transverse momenta'' Q_1 and Q_2 have ''finite lightlike components'' out of the ''transverse plane,'' i.e., the 2-3 plane. Most importantly, if the transverse components of Q_1 and Q_2 vanish, then the lightlike component must vanish also. It will become more significant in the next section that we always identify the transverse plane as the 2-3 plane. (Note that the limits for each of P_1 and P_2 can be taken to be any linear combination of P_1^+ and P_2^+, and provided they are not parallel, the result will be the same. Consequently, the roles of P_1 and P_2 can be smoothly interchanged.)

Finally, we give two corresponding realizations of the ''nonflip'' limit. In this case, if $u_1\sim u_2$, then s_{12} and $s_{12'}$ are also finite. This allows P_1 and P_2 to have parallel limiting values. We first define a limit L_3, in which P_3 lies along a different light cone. We define the following:
L_3,

$$P_1\to P_1^+=(p_1,p_1,0,0),\quad p_1\to\infty,$$

$$Q_1\to q_2-q_3=(0,0,q_2,-q_3),$$

$$P_2\to P_2^+=(p_2,p_2,0,,0),\quad p_2\to\infty,$$

$$Q_2\to q_3-q_2'=(0,0,-q_2',q_3),$$

$$P_3\to P_3^+=(p_3,0,0,p_3),\quad p_3\to\infty,$$

$$Q_3\to q_2'-q_2=(0,0,q_2'-q_2,0). \tag{4.23}$$

The behavior of invariants is now

$$s_{12}\not\to\infty,\quad s_{23}\to 2p_2p_3,\quad s_{31}\to 2p_3p_1,$$

$$s_{122'}\not\to\infty,\quad s_{233'}\not\to\infty,\quad s_{311'}\to -2p_3q_3. \tag{4.24}$$

Comparing with Eqs. (4.8) and (4.10)–(4.15), we see that the L_3 limit is the simple helicity-pole ''nonflip limit'' (4.8) with

$$p_1 \sim u_1, \quad p_2 \sim u_2, \quad p_3 \sim z_3. \tag{4.25}$$

We can also take P_3 to be in the same plane as P_1 and P_2, but with opposite space component. In this case Q_1 and Q_2 again acquire finite lightlike components out of the transverse plane. We define the following:
L_3',

$$P_1 \to P_1^+ = (p_1, p_1, 0, 0), \quad p_1 \to \infty,$$

$$Q_1 \to q_2 - q_3 - q_3^+ = (-q_3^+, -q_3^+, q_2, 0),$$

$$P_2 \to P_2^+ = (p_2, p_2, 0, 0), \quad p_2 \to \infty,$$

$$Q_2 \to q_3 - q_3^+ - q_2' = (q_3^+, q_3^+, -q_2', q_3),$$

$$P_3 \to P_3^- = (p_3, -p_3, 0, 0), \quad p_3 \to \infty,$$

$$Q_3 \to q_2' - q_2 = (0, 0, q_2' - q_2, 0). \tag{4.26}$$

The behavior of invariants is essentially the same as in Eq. (4.24). However, in contrast to L_2', the lightlike component q_3^+ can be chosen independently of q_3 and so does not have to vanish if q_3 vanishes.

From Eqs. (4.19) and (4.23) we see that the ''helicity-flip'' and ''nonflip'' limits L_2 and L_3 can, respectively, be distinguished by whether p_1 and p_2 are in opposite directions or the same direction on one light cone. From Eqs. (4.26) it is also clear that the nonflip limit is truly a ''planar limit.'' Equation (4.22) differs from Eq. (4.26) in that P_2 lies out of the plane.

C. SW representation and Regge behavior

As we outlined in the previous section, the SW representation is obtained by writing appropriate partial-wave expansions for each set of hexagraphs related by twisting. In particular, for the set of all hexagraphs related to Fig. 17 by twisting, we write

$$A_6^H(z_1, z_2, z_3, u_1, u_2) = \sum d^{J_1}_{-n_1,0}(z_1) d^{J_2}_{-n_2,0}(z_2) \times d^{J_3}_{n_1+n_2,0}(z_3) u_1^{n_1} u_2^{n_2} a_{J,n}. \tag{4.27}$$

(As in our discussion of nonsense states in the previous section, $-n_2$ is the t_3-channel center-of-mass helicity. Again, we remark that we choose the present symmetric notation and language to make direct contact with s-channel helicity amplitudes.) The SW transform is obtained by converting the sums over n_1, n_2, and J_3 to integrals. To illustrate the general formalism more simply, we again (temporarily) ignore signature. In this case we can write

$$A_6^H = \int_{>+<} \frac{dn_1 (u_1)^{n_1}}{\sin \pi n_1} \int_{>+<} \frac{dn_2 (u_2)^{n_2}}{\sin \pi n_2} \times \int \frac{dJ_3 d^{J_3}_{0,n_1+n_2}(z_3)}{\sin \pi (J_3 - n_1 - n_2)} \sum_{J_1 - |n_1| = 0}^{\infty} d^{J_1}_{-n_1,0}(z_1) \times \sum_{J_2 - |n_2| = 0}^{\infty} d^{J_2}_{-n_2,0}(z_2) a^{H_6, \gtrless}_{\underset{\sim}{J} \underset{\sim}{n}}, \tag{4.28}$$

where the $\gtrless$ labels indicate the presence of separate integrals to reproduce the positive and negative helicity sums.

The triple-Regge limits and helicity-pole limits can be studied by pulling the contours in Eq. (4.28) to the left in the complex plane. (Again, we do not discuss the subtleties of introducing second-type representation functions, etc., that are necessary to obtain a true asymptotic expansion.) In the triple-Regge limit, Regge poles at $l_1 = \alpha_1$, $l_2 = \alpha_2$, and $l_3 = \alpha_3$ give contributions to each of the terms in the double sum in Eq. (4.28) and we obtain a result very similar to Eq. (3.34) (for simplicity, we omit the denominator sine factors):

$$A_6^H \underset{\substack{z_1, z_2, \\ z_3, \to \infty}}{\sim} z_1^{\alpha_1} z_2^{a_2} z_3^{\alpha_3} \sum_{N_1=0}^{\infty} \sum_{N_2=0}^{\infty} [u_1^{\alpha_1 - N_1} u_2^{\alpha_2 - N_2} \beta_{\alpha_1, \alpha_2, \alpha_3, N_1, N_2} + u_1^{-\alpha_1 + N_1} u_2^{\alpha_2 - N_2} \beta_{-\alpha_1, \alpha_2, \alpha_3, N_1, N_2} + u_1^{\alpha_1 - N_1} u_2^{-\alpha_2 + N_2} \beta_{\alpha_1, -\alpha_2, \alpha_3, N_1, N_2} + u_1^{-\alpha_1 + N_1} \times u_2^{-\alpha_2 + N_2} \beta_{-\alpha_1 - \alpha_2, \alpha_3, N_1, N_2}], \tag{4.29}$$

where $\beta_{\alpha_1, \alpha_2, \alpha_3, N_1, N_2}$ is the Regge-pole residue of the FG (analytically continued) ''nonflip helicity amplitude'' $a^{H_6, > >}_{J_1, J_2, J_3, n_1, n_2}(t_1, t_2, t_3)$ at $J_i = \alpha_i$, $i = 1, 2, 3$, and $n_i = J_i - N_i$, $i = 1, 2$, and $\beta_{-\alpha_1, \alpha_2, \alpha_3, N_1, N_2}$ is the Regge-pole residue of the ''helicity-flip'' amplitude $a^{H_6, > <}_{J_1, J_2, J_3, n_1, n_2}(t_1, t_2, t_3)$ at $J_i = \alpha_i$, $i = 1, 2, 3$, and $n_1 = -J_1 + N_1$, $n_2 = J_2 - N_2$. The $u_i^{\pm \alpha_1}$ contributions come, respectively, from the $\gtrless$ integrals in Eq. (4.28). [The symmetry under $u_1 \to 1/u_1$, $u_2 \to 1/u_2$ implies that the first and last sums in Eq. (4.29) can be identified, as can the second and third. When the hexagraph of Fig. 16 is part of a larger hexagraph, this symmetry is, in general, not present.]

To obtain the complete behavior of M_6 in the triple-Regge limit, we must add contributions corresponding to the additional hexagraphs illustrated in Fig. 2. These contributions will have the same general form as Eq. (4.29), but with the indices 1, 2, and 3 cyclically rotated. We also add twisted graphs by incorporating signature factors properly.

In analogy with Eq. (3.28), the helicity-pole limit (4.8) picks out the first term of the first sum in Eq. (4.29), i.e.,

$$A_6 \underset{\substack{u_1, u_2, \\ z_3, \to \infty}}{\sim} (z_1 u_1)^{\alpha_1} (z_2 u_2)^{\alpha_2} z_3^{\alpha_3} \beta_{\alpha_1, \alpha_2, \alpha_3, 0, 0}, \tag{4.30}$$

while the second limit picks out the first term of the second sum, i.e.,

$$A_6 \underset{\substack{u_1,1/u_2,\\ z_3,\to\infty}}{\sim} (z_1u_1)^{\alpha_1}(z_2u_2^{-1})^{\alpha_2}z_1^{\alpha_3}\beta_{\alpha_1,-\alpha_2,\alpha_3,0,0}, \quad (4.31)$$

and so distinct helicity amplitudes, i.e., nonflip and flip, contribute in the distinct helicity-pole limits, while both amplitudes contribute in the full triple-Regge limit. This is why we refer to Eqs. (4.8) and (4.9), respectively, as nonflip and helicity-flip limits. Note that, as we anticipated in the previous subsection, in both limits the dependence on both z_1 and z_2 is determined by the u_1 and u_2 dependence. This is necessary for the amplitudes to be directly expressible in terms of invariants, as is done in the next subsection.

D. Asymptotic analytic structure

Consider how the cuts of Fig. 16 are represented asymptotically. From Eqs. (4.10)–(4.12), we can write

$$(z_1u_1)^{\alpha_1}(z_2u_2)^{\alpha_2}z_3^{\alpha_3}=(z_1z_3u_1)^{\alpha_1}(z_1z_3u_2)^{\alpha_2}(z_3)^{\alpha_3-\alpha_1-\alpha_2} \sim(s_{13})^{\alpha_1}(s_{2'3'})^{\alpha_2}(s_{11'3})^{\alpha_3-\alpha_1-\alpha_2}, \quad (4.32)$$

showing how the hexagraph cuts of Fig. 3(a) are represented in the limit (4.8). Similarly for the limit (4.9), we can write

$$(z_1u_1)^{\alpha_1}(z_2u_2^{-1})^{\alpha_2}z_3^{\alpha_3}=(z_1z_3u_1)^{\alpha_1}\left(\frac{z_2z_3}{u_2}\right)^{\alpha_2}(z_3)^{(\alpha_3-\alpha_1-\alpha_2)} \sim(s_{13})^{\alpha_1}(s_{2'3'})^{\alpha_2}(s_{11'3})^{\alpha_3-\alpha_1-\alpha_2}, \quad (4.33)$$

and so the cuts of Fig. 16(a) contribute similarly to both the nonflip and helicity-flip limits. However, for the limit (4.9) we can also write

$$\begin{aligned}(z_1u_1)^{\alpha_1}&(z_2u_2^{-1})^{\alpha_2}z_3^{\alpha_3}\\ &\sim(z_1z_3u_1)^{(\alpha_1+\alpha_3-\alpha_2)/2}\\ &\quad\times\left(\frac{z_2z_3}{u_2}\right)^{(\alpha_2+\alpha_3-\alpha_1)/2}\left(\frac{z_1z_2u_1}{u_2}\right)^{(\alpha_1+\alpha_2-\alpha_3)/2}\\ &\sim(s_{31})^{(\alpha_1+\alpha_3-\alpha_2)/2}(s_{23})^{(\alpha_2+\alpha_3-\alpha_1)/2}(s_{12})^{(\alpha_1+\alpha_2-\alpha_3)/2},\end{aligned} \quad (4.34)$$

showing that the cuts of Fig. 16(b) are also present. Both sets of cuts are represented simultaneously by the same asymptotic expression, which is equivalent to saying that asymptotically the two sets of cuts can not be distinguished. It is crucial that there is no expression corresponding to Eq. (4.34) for the limit (4.8). As a result, we conclude that both sets of cuts in Fig. 16 are present in the helicity-flip amplitude appearing in the limit (4.9), while only those of Fig. 16(a) appear in the nonflip amplitude. Conversely, we expect amplitudes with both sets of cuts to appear in the helicity-flip amplitude and not in the nonflip amplitude.

The importance of this last discussion is as follows. The conventional ''triple-Regge'' limit of the one-particle inclusive cross section has been studied [20] in some detail in QCD. As we noted above, it is in fact the nonflip helicity-pole limit (4.8) that is involved. In this limit only triple-Regge behavior associated with the inclusive cross-section discontinuities of Fig. 16(a) appears. The helicity amplitude that appears is the same amplitude that appears in the Reggeon unitarity formula for the two-Reggeon-cut discontinuity. Consequently, the triple-Pomeron vertex that appears in the inclusive cross section can be identified with the vertex, discussed in the next section, that appears in elastic scattering Pomeron diagrams and in RFT. However, there are additional ''helicity-flip'' triple-Regge vertices associated with the helicity-flip amplitude appearing in the limit (4.9) and, more generally, with the full set of helicity-flip amplitudes appearing in the full triple-Regge limit. These vertices appear in amplitudes containing both the usual inclusive cross-section cuts and the second set of cuts illustrated in Fig. 16(b). Such amplitudes have not been discussed within QCD. We will discuss some of the simplest contributing Feynman diagrams in Sec. VII. As we discuss in the next section, the additional vertices make very important contributions to the general solution of Reggeon unitarity for multiparticle amplitudes and, as a result, will play a crucial role in our general construction of hadrons and the Pomeron in QCD.

V. POMERON AND REGGEON DIAGRAM SOLUTIONS OF REGGEON UNITARITY

In Sec. III, we generically described a Regge pole participating in the generation of a Regge cut as a Reggeon and gave the controlling ''Reggeon unitarity'' equations. In this section we discuss the solution of these unitarity equations in terms of ''Reggeon diagrams,'' in analogy with the Feynman diagram solution of conventional momentum-space unitarity. Historically, such diagrams were first introduced [2] to describe the interactions of an even-signature Pomeron Regge pole. Later, they appeared as describing [5,18] the interactions of Reggeized gluons in leading (and next-to-leading) logarithmic calculations in massive gauge theories. Both Pomeron and Reggeized gluon diagrams are often referred to generically as ''Reggeon diagrams.'' In this section, for simplicity, we will use ''Reggeon'' to refer exclusively to an odd-signature (''Reggeized gluon'') Regge pole, with intercept close to unity. Therefore ''Reggeon diagrams'' involve Reggeized gluons and ''Pomeron diagrams'' involve Pomerons. We will also use ''Reggeon unitarity'' exclusively for the unitarity condition on Reggeons and use ''Pomeron unitarity'' to describe the unitarity condition for Pomerons. This will cause no confusion in this section since we will not consider diagrams containing both Reggeons and Pomerons. *A priori* they can certainly appear simultaneously in diagrams. Indeed, our ultimate aim is to first construct a Reggeon diagram description of QCD amplitudes and then, via the analysis of infrared divergences and the use of Pomeron ''phase-transition theory,'' convert to a Pomeron diagram description. At an intermediate stage there will in

fact be diagrams containing both Reggeons and Pomerons.

Pomeron and Reggon unitarity equations differ only in the structure of signature factors, and one purpose of this section is to describe the diagrams for both cases in the same formalism. The most important new result will be the extension of the diagram formalism to solve the unitarity equation (3.49) for a large class of multiparticle FG amplitudes. For the Reggeon case, there is a vector particle (the gluon) which becomes massless as the intercept of the Reggeon goes to 1. Massless particle states give rise to infrared divergences of Reggeon interactions which are very important in our later discussion of QCD. In this section we will consider only massive Reggeons and will only briefly discuss the specific form of Reggeon and Pomeron interactions. We begin with the simplest, and historically oldest, diagrams.

A. Pomeron diagrams for elastic scattering

We emphasize from the outset that we expect to use Pomeron (or Reggeon) diagrams to discuss infrared phenomena involving small t_i's (and small $\underline{k}$'s) only. We denote the Pomeron trajectory by $j=\alpha_{\mathbb{P}}(t)$, with $\alpha_{\mathbb{P}}(0)\sim 1$. Since the Pomeron has even signature, all multi-Pomeron cuts are also even signature and so signature factors can effectively be neglected. That is, for small values of all the t_i we can take, in Eq. (3.49),

$$\sin\frac{\pi}{2}(\alpha_1-\tau_1')\sim\cdots\sim\sin\frac{\pi}{2}(\alpha_M-\tau_M')\sim 1. \tag{5.1}$$

ξ_M simply gives a factor of -1 for each additional Pomeron in the state, and so for an M-Pomeron state,

$$\xi_M\sim(-1)^{M-1}. \tag{5.2}$$

We introduce the usual RFT variables, that is, energies E_i and two-dimensional momenta k_i, as follows. We write

$$J_i=1-E_i \quad \text{and} \quad t_i=k_i^2 \quad \forall i, \tag{5.3}$$

so that [with $\Delta_k=1-\alpha(t_k)$]

$$\delta\left(J-1-\sum_{k=1}^{M}\Delta_k\right)\leftrightarrow\delta\left(E-\sum_{k=1}^{M}\Delta_k\right), \tag{5.4}$$

which we can regard as ''energy conservation'' by Pomeron intermediate states. We can also write

$$\int\frac{dt_j dt_k}{\lambda^{1/2}(t_i,t_j,t_k)}\leftrightarrow 2\int d^2\underline{k}_j d^2\underline{k}_k\delta^2(\underline{k}_i-\underline{k}_j-\underline{k}_k), \tag{5.5}$$

which is ''momentum conservation'' for Pomerons. The Pomeron unitarity equation is initially derived for positive t and the change of variables (5.3) can be made with the k_i taken to be two-dimensional Minkowski momenta. However, the continuation to negative t is most simply done by rotating the plane of the k_i so that they become spacelike and can be straightforwardly identified with the transverse momenta of s-channel Feynman diagram or unitarity calculations. The full continuation of J-plane unitarity from the positive t region, where it is first derived, is actually quite complicated [21] and it is nontrivial, and very important, that the only J-plane singularities that survive at negative t are those due to Regge cuts. This implies that a solution of Pomeron unitarity in the small-t region should be sufficient to satisfy full multiparticle t-channel unitarity equations.

Note that since the amplitudes involved will be functions of the t_i invariants, the ''transverse plane'' involved in Eq. (5.5) can be shifted by the addition of an orthogonal lightlike vector without changing the resulting integrals. That is, the relation of the transverse plane to four-dimensional momenta is ambiguous up to an orthogonal lightlike vector. This point will be important later in the section.

For elastic (particle) scattering the negative t unitarity equation (3.49), with the approximations (5.1) and (5.2), is solved by Pomeron diagrams as follows. The even-signature FG amplitude $a^+(J,t)$ is written in the form

$$a^+(J,t)\equiv F(E,\underline{k}^2)=\sum_{m,n=1}^{\infty}F_{mn}(E,\underline{k}^2), \tag{5.6}$$

where [omitting all factors of $(2\pi)^3$]

$$F_{mn}(E,\underline{k}^2)=\int\prod_{i,j}d^2\underline{k}_i d^2\underline{k}'_j\,\delta^2\left[\underline{k}-\sum_{i=1}^{m}\underline{k}_i\right]\times\frac{g_m g_n A_{mn}(E,\underline{k}_1,\ldots,\underline{k}_m,\underline{k}'_1,\ldots,\underline{k}'_n)}{[E-\Sigma_{i=1}^{m}\Delta(\underline{k}_i)][E-\Sigma_{j=1}^{n}\Delta(\underline{k}'_j)]}. \tag{5.7}$$

The g_m are couplings of Pomerons to the external particles, which, in general, will be functions of the transverse momenta. In the approximation which gives Eqs. (5.1) and (5.2), we should take

$$g_m\sim(i)^m. \tag{5.8}$$

The A_{mn} are Pomeron scattering amplitudes (containing a momentum conserving δ function). To include the simplest diagrams (without Pomeron interactions) in Eq. (5.7), the A_{mn} should include disconnected amplitudes, e.g., the completely disconnected amplitude

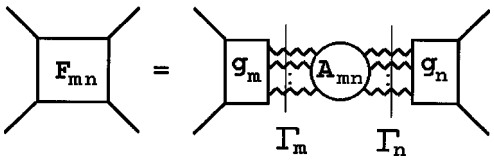

FIG. 18. Multi-Pomeron contribution to elastic scattering.

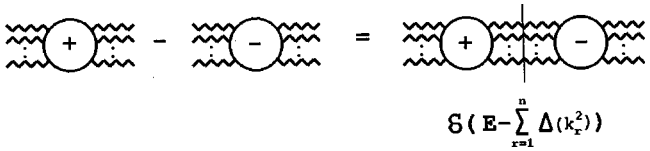

FIG. 19. Unitarity for Pomeron amplitudes.

FIG. 20. Pomeron vertices.

$$A_{mn}(E,\underset{\sim}{k},\underset{\sim}{k}')=\delta_{mn}\delta^2\left(\sum \underset{\sim}{k}_i-\sum \underset{\sim}{k}'_i\right)\Gamma_m^{-1}(E,\underset{\sim}{k}_1,\ldots,\underset{\sim}{k}_m), \tag{5.9}$$

where Γ_m is the m-Pomeron propagator:

$$\Gamma_m(E,\underset{\sim}{k}_1,\ldots,\underset{\sim}{k}_m)=\frac{1}{[E-\Sigma_{r=1}^m\Delta_r(\underset{\sim}{k}_r)]}. \tag{5.10}$$

Equation (5.7) is illustrated in Fig. 18. The amplitudes A_{mn} must satisfy the Pomeron unitarity equation

$$\begin{aligned}A_{mn}(E+i\epsilon,\underset{\sim}{k},\underset{\sim}{k}')-A_{mn}(E-i\epsilon,\underset{\sim}{k},\underset{\sim}{k}')\\ =\sum_r(-1)^r i\int\prod_s d^2\underset{\sim}{k}''_s\,\delta\left[E-\sum_{s=1}^r\Delta_s\right]\\ \times A_{mr}(E+i\epsilon,\underset{\sim}{k},\underset{\sim}{k}'')A_{rn}(E-i\epsilon,\underset{\sim}{k}'',\underset{\sim}{k}').\end{aligned} \tag{5.11}$$

This equation is illustrated in Fig. 19.

It is straightforward to write a general solution to Eq. (5.11) in terms of a (nonrelativistic) graphical expansion involving arbitrary (nonsingular) vertices and propagators for states containing any number of Pomerons. (That interactions are nonsingular is assumed because of the absence of massless particles in the strong interaction.)

In the notation illustrated in Fig. 20, we take, as interaction vertices,

$$\Gamma_{12}(=\Gamma_{21}^*)=ir_0+\cdots,\quad \Gamma_{13}=\lambda_0+\cdots,\quad \Gamma_{22}=\lambda_0'+\cdots, \tag{5.12}$$

etc. The ellipses indicate that we could add transverse momentum dependence to the interaction vertices, but this would actually be inconsistent with making the approximations (5.1), (5.2), and (5.8). It is important that all of these approximations are ultimately justified when the critical Pomeron solution of RFT is formulated [3]. It can be shown that all the neglected terms correspond to irrelevant operators in the renormalization group scaling introduced at the critical point.

A general solution to Eq. (5.11) is then given by the complete set of diagrams having the general form illustrated in Fig. 21. These diagrams involve all possible combinations of propagators Γ_m, given by Eq. (5.10), coupled by the interaction vertices Γ_{mn} given by Eqs. (5.12). There is an integration $\int d^2\underset{\sim}{k}$ for each loop, and momentum conservation is imposed at each vertex. The factor of i in front of r_0 in Eqs. (5.12) and all vertices for odd numbers of Pomerons reproduce the $(-1)^r$ factor in Eq. (5.11) when the usual graph-cutting rules are applied.

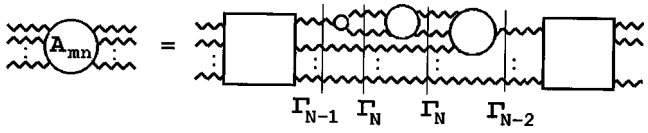

FIG. 21. General form of Pomeron diagrams.

B. Reggeon diagrams for elastic scattering

We consider next the modification of the diagrams of the last subsection when the Pomeron is replaced by an odd-signature Reggeon with trajectory $j=\alpha_R(t)$ such that $\alpha_R(M^2)=1$, where $M^2\sim 0$. The product signature rule says that odd-number Reggeon states appear in the odd-signature amplitude and even-number states appear in the even-signature amplitude. In a (spontaneously broken) gauge theory, the color quantum numbers break the signatured amplitudes up into subamplitudes.

For small values of all the t_i we now take, in Eq. (3.49),

$$\sin\frac{\pi}{2}(\alpha_i-\tau_1')\sim\frac{\pi}{2}\alpha'(t_i-M^2). \tag{5.13}$$

In the same approximation ξ_M gives a factor of $+1$ when two odd-signature states are combined and a factor of -1 when an odd-signature and even-signature state are combined or when two even-signature states are combined. Instead of Eq. (5.6), we write

$$a^{\pm}(J,t)\equiv F^{\pm}(E,\underset{\sim}{k}^2)=\sum_{n,m=\text{even/odd}}^{\infty}F^{\pm}_{nm}(E,\underset{\sim}{k}^2), \tag{5.14}$$

where even/odd summations are, respectively, associated with the $+/-$ sign and [now omitting, in addition to the factors of $(2\pi)^3$, the factors of $(\pi/2)\alpha'$, which compensate for the change in dimensions produced by the particle poles]

$$\begin{aligned}F^-_{m,n=\text{odd}}(E,\underset{\sim}{k}^2)=\int\prod_{i,j}\frac{d^2\underset{\sim}{k}_i}{(\underset{\sim}{k}_i^2+M^2)}\frac{d^2\underset{\sim}{k}'_j}{(\underset{\sim}{k}'^2_j+M^2)}\\ \times\delta^2\left[\underset{\sim}{k}-\sum_{i=1}^m\underset{\sim}{k}_i\right]\\ \times\frac{G_mG_nA^-_{mn}(E,\underset{\sim}{k}_1,\ldots,\underset{\sim}{k}_m,\underset{\sim}{k}'_1,\ldots,\underset{\sim}{k}'_n)}{[E-\Sigma_{i=1}^m\Delta(\underset{\sim}{k}_i)][E-\Sigma_{j=1}^n\Delta(\underset{\sim}{k}'_j)]},\end{aligned} \tag{5.15}$$

The G_m are couplings of Reggeons to external particles and the A^-_{mn} are odd-signature Reggeon scattering amplitudes. The scattering amplitudes A^-_{mn} satisfy the Reggeon unitarity equation

$$A^-_{mn}(E+i\epsilon,\underline{k})-A^-_{mn}(E-i\epsilon,\underline{k})$$
$$=\sum_{r=\text{odd}}(-1)^{(r-1)/2}\int\prod_s\frac{d^2\underline{k}_s}{(\underline{k}_s^2+M^2)}$$
$$\times\delta\left[E-\sum_{s=1}^{r}\Delta_s\right]A^-_{mr}(E+i\epsilon,\underline{k})A^-_{rn}(E-i\epsilon,\underline{k}). \tag{5.16}$$

F^+_{mn} is similarly defined in terms of amplitudes A^+_{mn} satisfying the analogous equation.

The Reggeon unitarity equations can again be solved by Reggeon diagrams. We can introduce general Reggeon interaction vertices in the same way as we did for the Pomeron. Because of signature conservation, there is no Γ_{12} vertex, only Γ_{22} and Γ_{13} vertices. For the m-Reggeon propagator Γ_m, we take

$$\Gamma_m(E,\underline{k}_1,\ldots,\underline{k}_m)=\frac{1}{\Pi(\underline{k}_r^2+M^2)[E-\Sigma_{r=1}^m\Delta_r(\underline{k}_r)]}. \tag{5.17}$$

It is well known that a Reggeon diagram formalism is exactly what emerges [11,18] from leading and next-to-leading logarithmic calculations in gauge theories. This is a very nontrivial result. Indeed, as is explicitly shown in [18], matching sixth-order calculations with Reggeon diagrams allows Γ_{22} to be extracted. The existing higher-order (eighth- and tenth-order) results are then predicted completely by iterating the Reggeon interaction. This is consistent with the requirement that, once the form of the Reggeon interactions is known, the structure of the full set of Reggeon diagrams is determined by Reggeon unitarity. However, the Reggeon interaction obtained is quite complicated, and so in the next subsection we digress from our general formalism to briefly summarize some of the results obtained in massive (i.e., spontaneously broken) gauge theories.

C. Reggeon diagrams in gauge theories

Because of the presence of (close to) massless particles, the Reggeon interaction vertices of a gauge theory (unlike the Pomeron vertices discussed above) contain transverse momentum singularities and cannot be approximated as regular. For simplicity we assume in this section that gauge symmetry breaking has provided all gluons with the same mass. In Sec. VIII we will consider a more complicated situation.

In lowest-order perturbation theory, the trajectory function is given by

$$\alpha(q^2)=1+\Delta(q^2)$$
$$=1+g^2C(q^2+M^2)J_1(q^2), \tag{5.18}$$

where C is a color factor that we give below and

$$J_1(q^2)\sim\int\frac{d^2\underline{k}_1d^2\underline{k}_2}{(\underline{k}_1^2+M^2)(\underline{k}_2^2+M^2)}\,\delta^2[\underline{q}-\underline{k}_1-\underline{k}_2]. \tag{5.19}$$

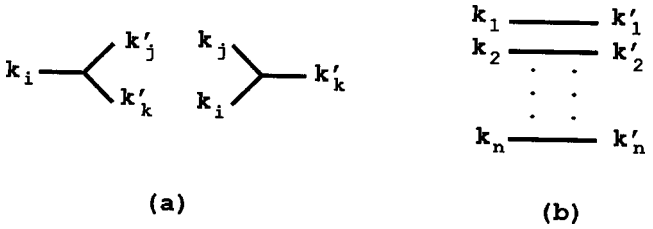

FIG. 22. (a) Vertices and (b) intermediate states in transverse momentum diagrams.

Introducing transverse momenta $\underline{k}_1$, $\underline{k}_2$, $\underline{k}_1'$, $\underline{k}_2'$ that satisfy momentum conservation (i.e., $\underline{k}_1+\underline{k}_2=\underline{k}_1'+\underline{k}_2'$), we can write [18]

$$\Gamma_{22}(\underline{k}_1,\underline{k}_2,\underline{k}_1',\underline{k}_2')=a(\underline{k}_1+\underline{k}_2)^2+bM^2$$
$$-cR_{22}(\underline{k}_1,\underline{k}_2,\underline{k}_1',\underline{k}_2'), \tag{5.20}$$

where a, b, and c are color factors, which we discuss below, and R_{22} has the complicated structure

$$R_{22}(\underline{k}_1,\underline{k}_2,\underline{k}_1',\underline{k}_2')$$
$$=\frac{(\underline{k}_1^2+M^2)(\underline{k}_2^{2'}+M^2)+(\underline{k}_2^2+M^2)(\underline{k}_1^{2'}+M^2)}{(\underline{k}_1-\underline{k}_1')^2+M^2}$$
$$+\frac{(\underline{k}_1^2+M^2)(\underline{k}_1^{2'}+M^2)+(\underline{k}_2^2+M^2)(\underline{k}_2^{2'}+M^2)}{(\underline{k}_1-\underline{k}_2')^2+M^2}. \tag{5.21}$$

The (massive) BFKL equation [5] is simply the color-zero Reggeon ''Bethe-Salpeter'' equation obtained by iterating the Reggeon interaction Γ_{22} in Reggeon diagrams.

In other papers [22] we have outlined a program for constructing Reggeon interactions by beginning with a Γ_{12} vertex which contains a nonsense zero that ensures it does not participate directly as a Reggeon vertex. The singular part of Reggeon interactions [including the massless limit of Eq. (5.21) giving the BFKL kernel] can then be constructed from t-channel particle discontinuities and the Reggeon Ward identities discussed in the next section. This construction implies that we can simultaneously discuss the color structure and the singularities of Reggeon interactions due to particle (gluon) poles by introducing the transverse momentum diagram notation illustrated in Fig. 22. (Transverse momentum diagrams are essentially Reggeon diagrams without Reggeon propagators.)

Amplitudes are obtained by combining vertices and intermediate states according to the following rules.

(i) For each three-point vertex, illustrated in Fig. 22(a), we write a factor

FIG. 23. Trajectory function.

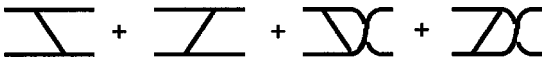

FIG. 24. Reggeon interaction R_{22}.

$$16\pi^3 f_{ijk}\delta^2\Big(\sum k_i - \sum k_i'\Big)\Big[\Big(\sum k_i\Big)^2 + M^2\Big],$$

where f_{ijk} is the usual antisymmetric group tensor.

(ii) For each intermediate state, illustrated in Fig. 22(b), we write a factor

$$(16\pi^3)^{-n}\int \frac{d^2k_1\cdots d^2k_n}{(k_1^2+M^2)\cdots(k_n^2+M^2)}.$$

The trajectory function (5.18), with the color factor included, is now given by the simple transverse momentum diagram shown in Fig. 23.

The interaction term cR_{22} is given by the sum of diagrams in Fig. 24.

We have used a thick line in the above transverse momentum diagrams to specifically indicate that color factors are included in the same notation. Note that the interaction of Fig. 24 is not projected on a particular color channel in the t channel.

The regular part of the Reggeon interaction Γ_{22} is more complicated to include in the diagram formalism. The zero-mass part [i.e., the $(\underline{k}_1+\underline{k}_2)^2$ term] is determined, from the singular part, by the Reggeon Ward identities that we discuss in the next section. In the color channel with gluon quantum numbers, the mass term can be included diagrammatically as shown in Fig. 25.

We also introduce a diagrammatic notation for color factors only that will be useful in the remainder of the paper. This is illustrated in Fig. 26 (since only color factors are involved we use thinner lines). We have included the symmetric d tensor that exists in SU(N) for $N\geqslant 3$ and expressed a number of useful identities, not all of which are independent, in the same notation.

The Reggeization of the gluon implies that in the gluon quantum-number channel, the leading higher-order interactions give only simple Regge-pole exchange. The necessary condition for Reggeization is [5] the ''bootstrap cancellation'' that is expressed in terms of transverse momentum diagrams in Fig. 27. The momentum part of this equation is trivial, given the structure of the vertices. The color part follows from Fig. 26(e). The cancellation of Fig. 27 ensures that when the Reggeon interaction Γ_{22} is included in the triple-Reggeon interaction, only Fig. 25 survives and this simply iterates the Reggeization.

It is interesting to note that, because of Fig. 26(f), the cancelation of Fig. 27 holds also if the left-hand vertex in each diagram is replaced by a vertex containing a d tensor. This implies that in QCD there is an additional ''bound-state'' Reggeon [20] (or colored Pomeron) in the symmetric octet channel with a trajectory that is exchange degenerate with the Reggeized gluon. We will refer frequently to this feature in later sections.

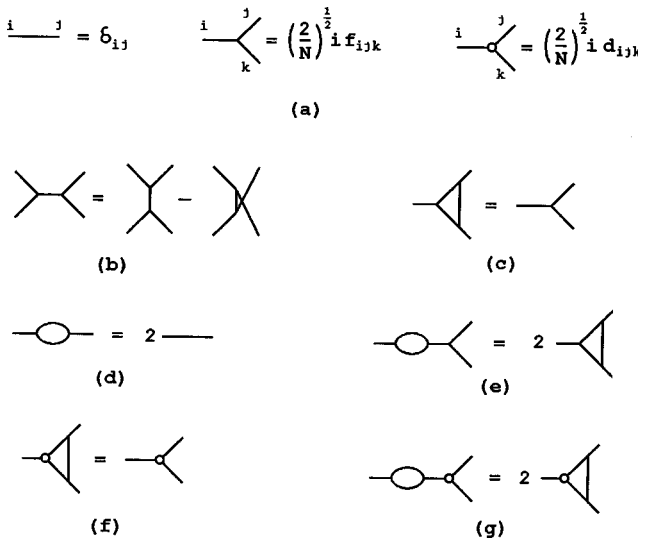

FIG. 26. (a) Color tensors, (b) the Jacobii identity, and (c)–(g) relations between tensors.

It is clear from Eqs. (5.18) and (5.21) that both the trajectory function and the Reggeon interaction are singular as the mass $M\to 0$. We will discuss the significance of this singularity structure in detail in Sec. VIII. In the next subsection we return to our abstract discussion and consider the extension of the elastic scattering formalism to multiparticle amplitudes. We continue to illustrate most of our discussion with Pomeron diagrams because specific examples are simpler to write down. However, we will constantly emphasize the close similarity of Pomeron and Reggeon diagrams.

D. Helicity amplitude Pomeron diagrams and helicity-flip vertices

We begin our discussion of multiparticle amplitudes by considering the implications of Pomeron unitarity for the helicity-pole limits (4.8) and (4.9) discussed in the previous section. In both cases the leading behavior is described by a single (analytically continued) helicity amplitude which satisfies Eq. (3.49) in a straightforward manner.

Pomeron diagrams describing the nonflip limit, which, as we noted, is the usual inclusive cross-section triple-Regge limit, were studied many years ago. The structure of the diagrams was derived directly from Pomeron unitarity [23], as we now describe, and also from hybrid Feynman diagram calculations [24]. The results were the same. For simplicity, we omit signature labels as in Sec. IV and again introduce Reggeon field theory notation by writing for the nonflip am-

FIG. 25. Regular interaction in the Reggeon channel.

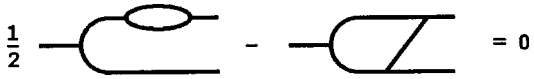

FIG. 27. Bootstrap condition for Reggeization.

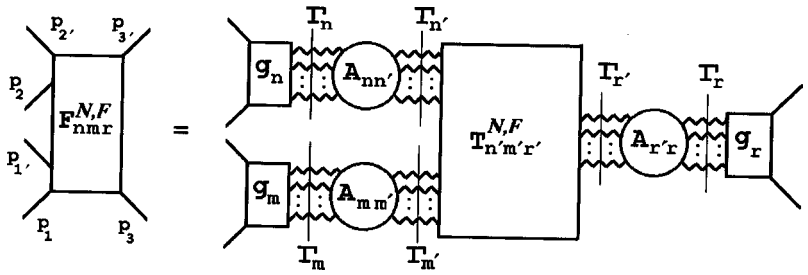

FIG. 28. Triple-Regge Pomeron diagrams for $F^{\mathcal{N},\mathcal{F}}_{mnr}$.

plitude, introduced via Eq. (4.28), as

$$A^{\mathcal{N}}(E_1,E_2,E_3,q_1^2,q_2^2,q_3^2)\equiv a^{H_6,>>}_{J_1,J_2,J_3,n_1,n_2}(t_1,t_2,t_3), \tag{5.22}$$

with $n_1=J_1$, $n_2=J_2$, $J_i=1-E_i$, and $t_i=q_i^2$, $i=1,2,3$. For the helicity-flip amplitude we similarly write

$$A^{\mathcal{F}}(E_1,E_2,E_3,q_1^2,q_2^2,q_3^2)\equiv a^{H_6,><}_{J_1,J_2,J_3,n_1,n_2}(t_1,t_2,t_3), \tag{5.23}$$

where, in this case, $n_1=J_1$, $n_2=-J_2$.

The crucial property of $A^{\mathcal{N}}$ and $A^{\mathcal{F}}$ is that they each satisfy a Pomeron unitarity equation in all three of the E_i channels, which is essentially the same as the unitarity equation for elastic amplitudes. As a result, we can write

$$A^{\gamma}(E_1,E_2,E_3)=\sum_{m,n,r} F^{\gamma}_{mnr}(\underline{E},\underline{t}), \quad \gamma=\mathcal{N},\mathcal{F}, \tag{5.24}$$

where $F^{\mathcal{N},\mathcal{F}}_{mnr}$ is constructed from Pomeron diagrams as illustrated in Fig. 28. The notation is the same as in Fig. 18 and the $A_{nn'}$ are again given by Fig. 21. The new element in Fig. 28 is the central vertex $T^{\mathcal{N},\mathcal{F}}_{m'n'r'}$ coupling the Pomerons in each E_i channel. The Pomeron unitarity equation forces the diagrams to have the essentially factorized form of Fig. 28 where, apart from the $T^{\mathcal{N},\mathcal{F}}$, all the couplings and interactions are identical to those appearing in elastic scattering. Indeed, the flip-nonflip distinction between the amplitudes is carried only by the $T^{\mathcal{N},\mathcal{F}}$ vertices.

If the $T^{\mathcal{N},\mathcal{F}}$ are connected amplitudes which can, like the g_n, be treated as constants independent of all the Reggeon transverse momenta, then the unitarity condition is clearly satisfied. Each E_i channel will have a separate transverse momentum plane and will be completely separate dynamically. Also, when the Pomeron intercept is close to unity and all transverse momenta are small, we have

$$E_1\sim\sum\Delta(k_{m'}^2)\sim E_2\sim\sum\Delta(k_{n'}^2)\sim\sum\Delta(k_{r'}^2)\sim E_3\sim 0, \tag{5.25}$$

and so $T^{\mathcal{N}}_{m'n'r'}$ will coincide with the corresponding elastic scattering Pomeron vertex, in a first approximation. However, as we emphasized in Sec. III, ''helicity-flip vertices'' do not appear internally within the Reggeon unitarity equation. It is important for the dynamical role of the anomaly that we discuss in later sections that there are no vertices corresponding to the $T^{\mathcal{F}}_{m'n'r'}$ in elastic scattering Pomeron diagrams. These vertices appear only in the role of joining scattering channels, as in Fig. 28.

It is not necessary that $T^{\mathcal{N}}_{m'n'r'}$ or $T^{\mathcal{F}}_{m'n'r'}$ be connected. In fact, diagrams involving disconnected $T^{\mathcal{N},\mathcal{F}}$ vertices are the most interesting dynamically since they couple the transverse momentum dependence in the three channels. Such diagrams play a crucial role in our analysis. Therefore we want to be sure we fully understand their construction and their dynamical origin. As the following discussion shows, there are various subtleties when disconnected $T^{\mathcal{N},\mathcal{F}}$ vertices are involved. The relative definition of the transverse momentum planes becomes an issue, as well as the ordering of different disconnected interactions.

The simplest diagram with a disconnected vertex is that shown in Fig. 29. This has the disconnected vertex illustrated in Fig. 30, i.e., one disconnected pomeron line, together with a T_{21} vertex. We have used a square, and the T_{21} notation, in order to emphasize that the $T^{\mathcal{F}}_{21}$ vertex is distinct from the Γ_{21} vertex appearing in elastic scattering Pomeron diagrams.

The diagram of Fig. 29 is particularly simple since there is only one transverse momentum integral. The diagram is written explicitly as

$$F^{\gamma}_{122}(E_1,E_2,E_3,Q_1^2,Q_2^2,Q_3^2)=g_1g_2^2\Gamma_1(E_2)\int d^2\underline{k}\;\Gamma_2(E_1)\Gamma_2(E_3)T^{\gamma}_{21}((Q_1+k)^2,Q_2^2,(Q_3-k)^2)$$
$$=\frac{g_1g_2^2}{[E_2-\Delta(Q_2^2)]}\int\frac{d^2\underline{k}T_{21}((Q_1+k)^2,Q_2^2,(Q_3-k)^2)}{[E_1-\Delta(\underline{k}^2)-\Delta((Q_1-\underline{k})^2)][E_3-\Delta(\underline{k}^2)-\Delta((Q_3-\underline{k})^2)]}, \tag{5.26}$$

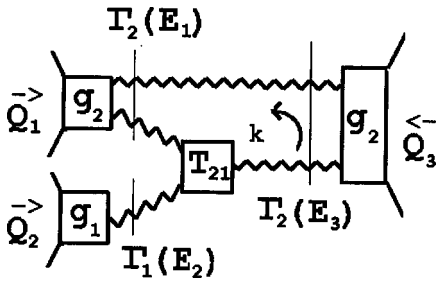

FIG. 29. Simplest disconnected triple-Regge Pomeron diagram.

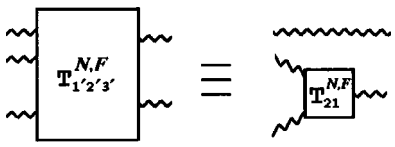

FIG. 30. Disconnected vertex of T_D.

where $\gamma=\mathcal{N},\mathcal{F}$. It is important to have a consistent physical interpretation of the ''transverse momentum'' in this diagram.

As we stated in the previous section, we will always define the ''transverse plane'' to be the 2-3 plane. An immediate question is whether the integration in Eq. (5.26) can be taken to be in the transverse plane. For the Reggeon cuts of Fig. 29 to be generated correctly, both Q_1 and Q_3 must either lie in the k plane or lie outside of it only by an orthogonal lightlike vector. Having in mind the underlying Feynman diagram origin of Regge behavior, we also expect that the presence of the Pomeron connecting the Q_1 and Q_3 external vertices requires the integration to be transverse to large light-cone momenta at these vertices. In principle, this also defines the plane for the integration.

At this point it becomes crucial that we are considering a helicity-pole limit, rather than a triple-Regge limit. The helicity-flip helicity-pole limit is the more complicated case. Consider the particular kinematics of the limit L_2 defined by Eqs. (4.19). In this case the ''transverse plane'' is indeed the the Q_i plane, but it is not orthogonal to P_3^+. However, if we take the realization L_2' given by Eqs. (4.22), then the transverse plane is orthogonal to both P_1 and P_3. Also, Q_3 lies in the transverse plane and Q_1 is obtained by adding an orthogonal lightlike vector to a vector in the transverse plane. Therefore, by using L_2' it is clear that the integration in Fig. 29 can indeed be taken to be the transverse plane (provided we utilize the transverse plane ambiguity).

For the nonflip limit, the L_3' description given in Eqs. (4.26) shows immediately that the transverse momentum integral can be defined to be the transverse plane, once the (lightlike vector) ambiguity for Q_1 is exploited. There is one important difference between the contribution of Fig. 29 in the flip and nonflip limits, apart from the different T_{21} vertices. This is in the implicit lightlike components carried by the Q_i. Using the L_2' and L_3' limits to justify writing the diagram as an integral in the transverse plane implies that if there is an infrared divergence as $Q_1\rightarrow 0$, then in the flip limit this is associated also with a vanishing longitudinal momentum, whereas for the nonflip limit this is not the case. This is important if infrared divergences of this kind are ultimately to be interpreted as related to wee partons and the ambiguities of light-cone quantization at zero longitudinal momentum.

Clearly, it is also important that in a helicity-pole limit the full six-point amplitude becomes dependent on only six of the eight independent variables, i.e., three invariants conjugate to E_1, E_2, and E_3 and the three t_i. The transverse integrals we are describing are able to represent the full amplitude only when it is independent of the remaining angles.

Consider next the diagram of Fig. 31. As indicated, there are now two transverse momentum integrals. The $\underline{k}_1$ integration should be be orthogonal to the light-cone momenta at the Q_1 and Q_3 vertices, while the $\underline{k}_2$ plane should be orthogonal to the light-cone momenta at the Q_2 and Q_3 vertices. However, to construct the diagram we can construct the $\underline{k}_1$ loop first using the L_2' limit for the helicity-flip limit or the L_3' limit for the nonflip limit. Then, having the invariant amplitude expressed as an integral in the transverse plane, we can smoothly interchange the form of P_1 and P_2 and similarly construct the $\underline{k}_2$ loop. The conclusion is that both integrations can be taken to be in the transverse plane.

In the notation illustrated, we can write Fig. 31 (as another relatively simple explicit example) in the form

$$T^{\gamma}(E_1,E_2,E_3,Q_1^2,Q_2^2,Q_3^2)=\int d^2\underline{k}_1 d^2\underline{k}_2 g_2^2 g_3 \Gamma_2(E_1)\Gamma_2(E_2)\Gamma_3(E_3) T_{21}^{\gamma}((Q_1+k_1)^2,(Q_2-k_2)^2,(k_1-k_2)^2)$$

$$=\int d^2\underline{k}_1 d^2\underline{k}_2 \frac{g_2^2 g_3}{[E_1-\Delta(\underline{k}_1^2)-\Delta((Q_1-\underline{k}_1)^2)][E_2-\Delta(\underline{k}_2^2)-\Delta((Q_2-\underline{k}_2)^2)]}$$

$$\times\frac{T_{21}^{\gamma}((Q_1+k_1)^2,(Q_2-k_2)^2,(k_1-k_2)^2)}{[E_3-\Delta((Q_1-\underline{k}_1)^2)-\Delta((Q_2-\underline{k}_2)^2)-\Delta((\underline{k}_1+\underline{k}_2)^2)]}. \tag{5.27}$$

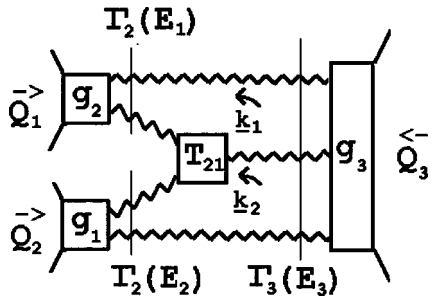

FIG. 31. Another disconnected triple-Regge Pomeron diagram.

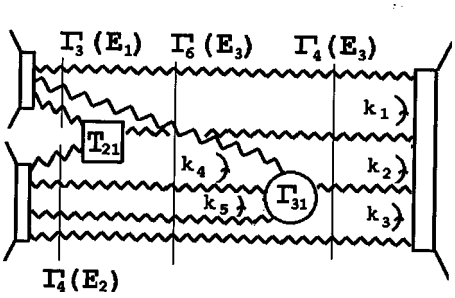

FIG. 33. Diagram of Fig. 32 with a particular nonconserving vertex.

An extension of the above discussion shows that there is no difficulty in constructing transverse momentum integrals for general diagrams of the form of Figs. 28 and 31 in which multiple Pomerons are exchanged, provided there is only a single disconnected vertex. It is important to remember, however, that the ''physical'' transverse momenta involved, in general, contain lightlike momenta orthogonal to the transverse plane that we integrate over. For helicity-flip limits the presence of the lightlike components has a special infrared significance.

Next, we consider Fig. 32 as an example of a diagram of the form of Fig. 28 in which there are apparently two disconnected central vertices. Diagrams of this kind are particularly relevant for the arguments of later sections. In this diagram there are five transverse momentum integrations and four Reggeon propagators. From the above discussion, all of the transverse integrations can be taken to be in the same plane. *A priori* it is not clear, however, which of the T_{21} and T_{31} vertices is ''energy nonconserving.'' By starting at each of the external particle couplings and considering the unitarity condition for each possible cut of the diagram, it is straightforward to show [23] that the diagram must contain only one unique energy-nonconserving vertex. (The same result was obtained for $A^{\mathcal{N}}$ amplitudes by direct calculation of hybrid Feynman diagrams [24].) The vertex occurs where there is a transition from E_1 and E_2 propagators to E_3 propagators. In particular, if we insert propagators as shown in Fig. 33, we determine that, as indicated by the notation, the T_{21} vertex is the energy-nonconserving vertex. Alternatively, as illustrated in Fig. 34, we can insert propagators in the same diagram in such a manner that the T_{31} vertex is nonconserving. In the inclusive cross section this freedom of choice is the freedom to choose the rapidity ordering of the two vertices. From the present perspective it is the topological ambiguity in the insertion of propagators which gives the freedom of choice.

The most general set of diagrams for both $A^{\mathcal{N}}$ and $A^{\mathcal{F}}$ involves all possible connected and disconnected $T^{\mathcal{N}}_{m'n'r'}$ and $T^{\mathcal{F}}_{m'n'r'}$, respectively. As in the last example, one diagram topology will often generate a number of distinct diagrams which differ only by which Reggeon propagators are inserted. All such diagrams are considered as distinct.

E. Helicity amplitude Reggeon diagrams

From our discussion of Reggeon and Pomeron diagrams for elastic scattering, it is clear that we can construct helicity amplitude Reggeon diagrams in close parallel with the construction of Pomeron diagrams. For Reggeon diagrams signature plays an important role, and so the new vertices $T^{\mathcal{N},\mathcal{F}}_{m'n'r'}$ carry signature labels for each E_i channel. Signature is not conserved by the new vertices (in addition to energy), although $T^{\mathcal{N}}_{m'n'r'}$ will carry a nonsense zero at $E_3-E_2-E_1=0$ when signature is not conserved. The signature-nonconserving $T^{\mathcal{F}}_{m'n'r'}$, i.e., the helicity-flip vertices, need not contain such a factor.

A particularly interesting situation occurs when a nonsense zero appears in one (or more) Reggeon vertices involved in an ordering ambiguity of the kind discussed for Pomeron vertices in the previous subsection. As discussed in [22], Reggeon interactions involving nonsense zero vertices can be constructed by simply allowing the zeros to cancel a corresponding Reggeon propagator. The logic behind this is that the zero will not appear in unsignatured amplitudes and that in such amplitudes the corresponding Reggeon diagram can be constructed with the Reggeon propagator present.

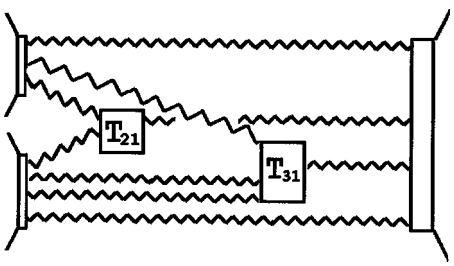

FIG. 32. Triple-Regge Pomeron diagram with two central vertices.

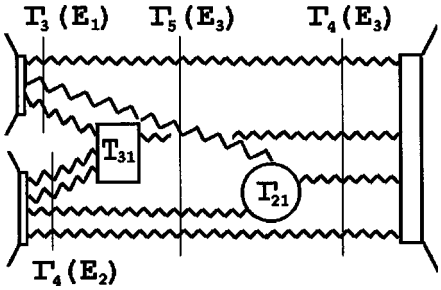

FIG. 34. Diagram of Fig. 32 with an alternative nonconserving vertex.

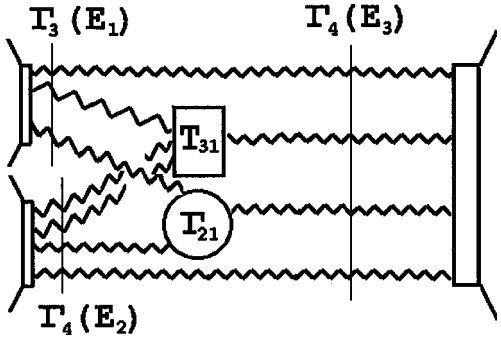

FIG. 35. Reggeon diagram with a disconnected nonconserving vertex

When the signatured amplitude is formed, the cancelation of the Reggeon propagator by the nonsense zero will occur. For example, if we consider Fig. 34 to be a Reggeon diagram, then Γ_{12} will be a signature-nonconserving, energy-conserving, vertex with a nonsense zero. This nonsense zero will effectively cancel the $\Gamma_5(E_3)$ propagator, and so the Γ_{12} and T_{31} vertices should simply be combined to obtain a single disconnected, energy-nonconserving, vertex as illustrated in Fig. 35.

We must determine the new $T^{\mathcal{N},\mathcal{F}}_{m'n'r'}$ vertices, by direct calculation in QCD. We will construct important massless quark components of these new vertices in Sec. VII. They play a crucial role in our infrared analysis.

F. Higher-order amplitudes

Consider next the hexagraph amplitude H_8 shown in Fig. 36. We consider both nonflip and helicity-flip limits at both vertices. A sufficient description of the behavior of invariants in both limits is

$$P_1\cdot P_2\sim\left(\frac{u_1}{u_2}+\frac{u_2}{u_1}\right),\quad P_1\cdot P_3\sim z\left(u_1u_3+\frac{1}{u_1u_3}\right),$$

$$P_3\cdot P_4\sim\left(\frac{u_3}{u_4}+\frac{u_4}{u_3}\right),\quad P_1\cdot Q_3\sim z\left(u_1+\frac{1}{u_1}\right),$$

$$Q_1\cdot Q_3\sim z,\quad P_4\cdot Q_1\sim z\left(u_4+\frac{1}{\mu_4}\right)\cdots,$$

$$P_1\cdot Q,P_2\cdot Q,P_3\cdot Q,P_4\cdot Q\quad\text{finite.}\tag{5.28}$$

The double nonflip limit is

$$u_1,u_2,u_3,u_4\to\infty,\tag{5.29}$$

while if the left-hand vertex, say, is helicity flip, the limit is

$$u_1,u_2^{-1},z,u_3,u_4\to\infty.\tag{5.30}$$

If $u_1\sim u_2$ and $u_3\sim u_4$, then we see from Eqs. (5.28) that in the double nonflip limit (5.29) both $P_1\cdot P_2$ and $P_3\cdot P_4$ are finite, whereas in the limit of Eq. (5.30) $P_1\cdot P_2\to\infty$.

Both limits are maximal helicity-pole limits, and so the SW representation shows that only a single helicity amplitude is involved. We can write the amplitude that appears in the double nonflip limit (5.29) as

$$A^{\mathcal{N}_\mathcal{L}\mathcal{N}_\mathcal{R}}(E_1,E_2,E,E_3,E_4),\tag{5.31}$$

where $J_i=n_i=1-E_i$, $i=1,2,3,4$, and $J=1-E$. Similarly, we can write the flip-nonflip amplitude appearing in the limit (5.30) as

$$A^{\mathcal{F}_\mathcal{L}\mathcal{N}_\mathcal{R}}(E_1,E_2,E,E_3,E_4),\tag{5.32}$$

where now $J_i=n_i=1-E_i$, $i=1,3,4$, $J_2=-n_2=1-E_2$, and $J=1-E$. We have used an obvious generalization of notation in which, for example, $\mathcal{F}_\mathcal{L}\mathcal{N}_\mathcal{R}$ denotes nonflip at the right vertex and helicity flip at the left vertex.

To understand how two-dimensional transverse momentum diagrams describe the limit, we discuss the realization of the limits (5.29) and (5.30) in terms of light-cone momenta as follows. For the double nonflip limit (5.31), we take, as external light-cone momenta,

$$P_1\to P_1^+=(p_1,p_1,0,0),$$

$$P_2\to P_2^+=(p_2,p_2,0,0),$$

$$P_3\to P_3^-=(p_3,-p_3,0,0),$$

$$P_4\to P_4^-=(p_4,-p_4,0,0),\quad p_i\to\infty\quad\forall i.\tag{5.33}$$

It is clear from Eqs. (5.28) that to realize the internal $z\to\infty$ limit the Q_i must also carry light-cone momenta, i.e.,

$$Q_1\to q_1^++Q_1^\perp,\quad Q_2\to -q_1^++Q_2^\perp,$$

$$Q_3\to q_3^-+Q_3^\perp,\quad Q_4\to -q_3^-+Q_4^\perp,\tag{5.34}$$

where the $q_i^\pm$ lie in the plane of the light-cone momenta (5.33). The $q_i^\pm$ are large, but not as large as the p_i. As we discussed after defining L_3' in the previous section, when the limit is nonflip (at both vertices), there is no problem in choosing the light-cone momenta independently from the

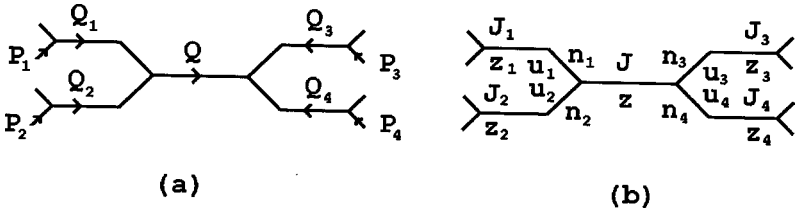

FIG. 36. A hexagraph H_8 for M_8: (a) momenta and (b) angular variables, angular momenta, and helicities.

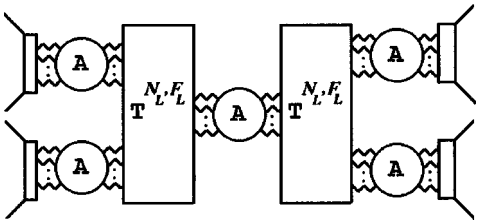

FIG. 37. Structure of Pomeron and Reggeon diagrams for $A^{\mathcal{N}_L\mathcal{N}_R}$, $A^{\mathcal{F}_L\mathcal{N}_R}$,... .

transverse momenta. The $Q_i^\perp$ are orthogonal to the light-cone momenta and lie in the transverse plane. Momentum conservation gives

$$Q = Q_1^\perp + Q_2^\perp = Q_3^\perp + Q_4^\perp . \tag{5.35}$$

For the nonflip-flip limit of Eq. (5.32), one possibility is to utilize L_2' and take

$$\begin{aligned} P_1 &\to P_1^+ = (p_1, p_1, 0, 0), \\ P_2 &\to P_2^+ = (p_2, 0, 0, p_2), \\ P_3 &\to P_3^- = (p_3, -p_3, 0, 0), \\ P_4 &\to P_4^- = (p_4, -p_4, 0, 0), \end{aligned} \tag{5.36}$$

while for the internal momenta we take Q_3 and Q_4 as above except that now we require specifically that

$$Q_3^\perp + Q_4^\perp = Q = (0, 0, q_2, 0), \tag{5.37}$$

so that Q is still orthogonal to all four of the P_i (this condition determines that we are considering a helicity-pole limit). For Q_1 and Q_2 we take

$$Q_1 \to \tilde{q}_1^- + Q_1^\perp , \quad Q_2 \to -\tilde{q}_1^+ + Q_2^\perp , \tag{5.38}$$

where $Q_1^\perp$ and $Q_2^\perp$ again lie in the transverse plane, but $\tilde{q}_1^+$ is chosen to ensure orthogonality to both P_1 and P_2; i.e., if

$$Q_1^\perp = (0, 0, q_{12}, q_{13}), \quad Q_2^\perp = (0, 0, q_2 - q_{12}, -q_{13}), \tag{5.39}$$

then

$$\tilde{q}_1^+ = (q_{13}, q_{13}, 0, 0). \tag{5.40}$$

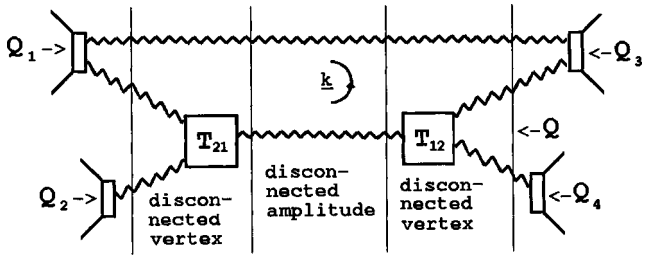

FIG. 38. Diagram with disconnected components.

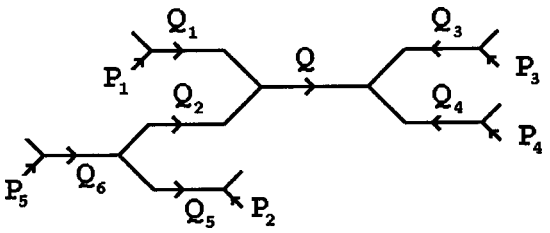

FIG. 39. Higher-order hexagraph.

Taking a helicity-flip limit at a vertex again requires the introduction of lightlike components determined by the spacelike components, for the corresponding Q_i. To realize the internal $z \to \infty$ limit, it would suffice to take only q_3^- large. We can not take $\tilde{q}_1^+$ large, i.e., take $q_{13} \to \infty$, since with the definitions (5.39) and (5.40) this would imply $Q_1^2, Q_2^2 \to \infty$. To contribute to or to realize the $z \to \infty$ limit with $\tilde{q}_1^+$, we must instead apply a Lorentz boost simultaneously to P_2 and $\tilde{q}_1^+$ that preserves their orthogonality. We write

$$P_2 \to (p_2 C, p_2 S, 0, p_2), \tilde{q}_1^+ \to (q_{13}(C+S), q_{13}(C+S), 0, 0), \tag{5.41}$$

where $C = \cosh \zeta$ and $S = \sinh \zeta$. We can then take $\zeta \to \infty$ as (all or) part of the limit $z \to \infty$. We notice that relative to P_2, the lightlike component of $\tilde{q}_1^+$ continues to vanish as $q_{13} \to 0$.

The double flip limit

$$u_1, u_2^{-1}, z, u_3, u_4^{-1} \to \infty \tag{5.42}$$

introduces the amplitude $A^{\mathcal{F}_L\mathcal{F}_R}(E_1, E_2, E, E_3, E_4)$. To introduce a light-cone realization, we proceed similarly. However, we now have the extra subtlety that $\tilde{q}$ momenta have to be introduced for both vertices and a Lorentz boost ζ is essential at one (or both) of the vertices to realize the internal $z \to \infty$ limit.

It seems that in a general helicity-pole limit we can always find a kinematic representation in which each of the internal Q_i momenta is out of the transverse plane only by an orthogonal lightlike vector. As the foregoing and following discussion shows, this feature underlies the fact that helicity-pole limits can be described by helicity amplitudes that satisfy Pomeron and Reggeon unitarity via transverse momentum integrals. We repeat that, for the QCD physics of divergences associated with the anomaly that we discuss in later sections, it is important to remember that in helicity-flip limits the physical ''transverse momenta'' involve a closely related lightlike longitudinal component.

G. Pomeron and Reggeon diagrams for higher-order amplitudes

The general form of the diagrams for each of the helicity amplitudes corresponding to Fig. 36 is illustrated in Fig. 37. (For simplicity, we have not explicitly included propagators.) As implied by the notation, the $T^{\mathcal{N},\mathcal{F}}$ vertices are the same as those that appear in the $A^{\mathcal{N},\mathcal{F}}$ discussed above—including disconnected vertices. *A priori* it is not obvious

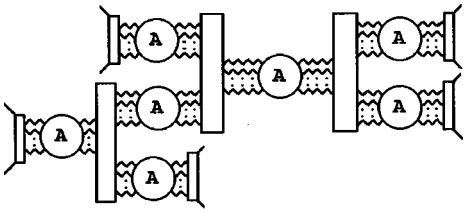

FIG. 40. Form of Reggeon-Pomeron diagrams for Fig. 38.

that the resulting diagrams involving disconnected vertices coupling disconnected interactions actually make sense. To see that this is the case, it will be helpful to consider further specific examples.

Consider next the diagram of Fig. 38, which involves both disconnected vertices and and a disconnected amplitude, first as a contribution to $A^{\mathcal{N}_\mathcal{L}\mathcal{N}_\mathcal{R}}$, then as a contribution to $A^{\mathcal{F}_\mathcal{L}\mathcal{N}_\mathcal{R}}$. To make sense within our formalism, it must be possible to write this diagram as a single integral in the transverse plane. According to our previous discussion, the k integration should be orthogonal to the large momenta at the Q_1 and Q_3 vertices. Also, for the Regge cuts in each of the Q_1, Q, and Q_3 channels, to have the correct discontinuity each of these momenta should either lie in the plane or be outside only by a lightlike vector.

To discuss $A^{\mathcal{N}_\mathcal{L}\mathcal{N}_\mathcal{R}}$ we use the kinematics of Eqs. (5.33)–(5.35). It is then clear that all of the requirements we have just listed are straightforwardly satisfied if we indeed take the k integration to be in the transverse plane. (Note that if we remove the external vertices, the same Reggeon amplitude appears within elastic scattering Pomeron diagrams except that the rapidities of the T_{21} and T_{12} vertices are integrated over to produce energy conservation.) To consider $A^{\mathcal{F}_\mathcal{L}\mathcal{N}_\mathcal{R}}$ we instead use the kinematics of Eqs. (5.36)–(5.40). Again, the necessary requirements are satisfied if the integration is in the transverse plane. We conclude that Fig. 28 gives a well-defined contribution to each of $A^{\mathcal{N}_\mathcal{L}\mathcal{N}_\mathcal{R}}$, $A^{\mathcal{F}_\mathcal{L}\mathcal{N}_\mathcal{R}}$, $A^{\mathcal{N}_\mathcal{L}\mathcal{F}_\mathcal{R}}$, and $A^{\mathcal{F}_\mathcal{L}\mathcal{F}_\mathcal{R}}$. As we have emphasized, whether the amplitude is flip or nonflip at each vertex is determined by whether the T_{21} and T_{12} vertices are flip or nonflip. When helicity-flip vertices are involved, the amplitude has no relationship to elastic scattering amplitudes.

As an example with an important new feature, we consider contributions to the hexagraph of Fig. 39. We consider the helicity-pole limit in which all the vertices are nonflip. The general form of Pomeron and Reggeon diagrams contributing in this limit is shown in Fig. 40. The internal box couplings once again indicate either $T^{\mathcal{N}}$ or $T^{\mathcal{F}}$ vertices which are both connected and disconnected.

We can set up a light-cone kinematic realization of the full nonflip limit by extending the discussion of the double nonflip limit of Fig. 36. We take $P_1,\ldots,P_4$ to have the same form as in Eqs. (5.33) and in addition take

$$P_5 \to P_5^+ = (p_5,0,0,p_5). \tag{5.43}$$

We also take $Q,Q_1,\ldots,Q_4$ as in Eqs. (5.34) and (5.37). In addition to Q_1 and Q_2, Q_5 and Q_6 must also be orthogonal to P_1 and P_2. Q_6 must be orthogonal to P_5, while Q_2 and Q_5 should not be. We therefore take Q_5 and Q_6 to have the form

$$\begin{aligned} Q_5 &\to Q_5^\perp + q_1^+ - \tilde{q}_6^- , \\ Q_6 &\to Q_6^\perp + \tilde{q}_6^- , \end{aligned} \tag{5.44}$$

where $Q_5^\perp$ and $Q_6^\perp$ lie in the transverse plane, but $\tilde{q}_6^-$ is chosen to ensure orthogonality of Q_6 to P_5^*; i.e., if

$$Q_6^\perp = (0,0,q_{62},q_{63}), \tag{5.45}$$

then

$$\tilde{Q}_6^- = (q_{63},q_{63},0,0). \tag{5.46}$$

We see from Eqs. (5.45) and (5.46) that to realize a sufficiently complicated nonflip limit we have had to introduce a lightlike component for some of the Q_i which are correlated with the transverse plane component. Previously, this was only necessary to realize helicity-flip limits. The internal Regge and helicity-pole limits, associated with the Q and Q_2 lines, respectively, can be realized by taking q_1^+ and q_3^- to be large appropriately. Alternatively, a Lorentz boost ζ could be applied as in Eqs. (5.41). To preserve the orthogonality conditions the boost has to be applied simultaneously to all of P_2, P_5, Q_5, and Q_6.

Now consider the contribution of the Pomeron diagram of Fig. 41 to the limit under discussion. With the above kinematics, both the $\underline{k}$ and $\underline{k}'$ integrations can be taken to be in the transverse plane. The internal boxes of Fig. 40 are indicated as thin-line boxes in Fig. 41. We now observe that, while the overall helicity-pole limit is entirely nonflip, the $\tilde{T}_{21}$ vertex in Fig. 41 must actually be a helicity-flip vertex. Although not directly coupled in the hexagraph of Fig. 39,

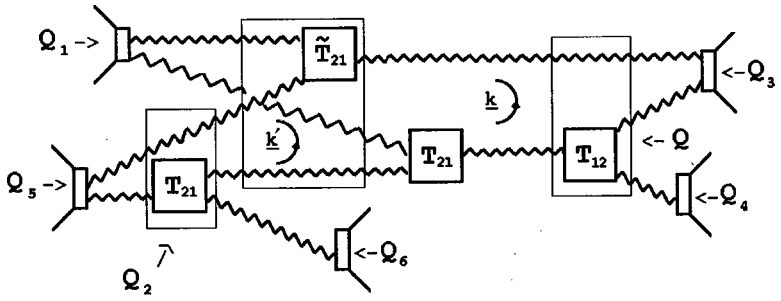

FIG. 41. Pomeron diagram having the form of Fig. 40.

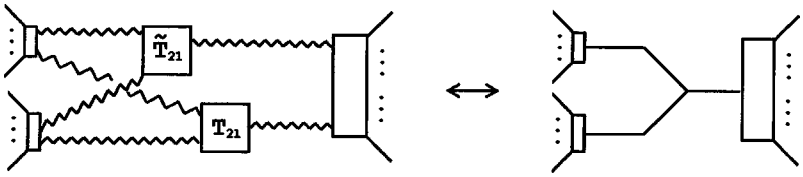

FIG. 42. Pomeron diagram and corresponding hexagraph.

P_1 and P_5 are in a relative helicity-flip limit. To see this we simply compare the form we have given for P_1, P_5, and P_3 with P_1, P_2, and P_3 in the L_2' limit (4.22). Therefore, if we introduce an internal vertex coupling, the corresponding external vertices it must be a helicity-flip vertex. Comparing with Fig. 38, we see that the addition of the additional P_5 momentum, in a new plane, has produced a helicity-flip interaction accompanying a helicity-nonflip interaction (i.e., the T_{21} vertex to the right of the $\tilde{T}_{21}$ vertex in Fig. 41).

The Pomeron diagram of Fig. 41 and the hexagraph of Fig. 39 have the general form illustrated in Fig. 42. The point made in our discussion of Fig. 41 extends to general diagrams having the form of Fig. 42. That is, in a nonflip helicity-pole limit, corresponding to the exposed vertex of the hexagraph of Fig. 42, a helicity-flip vertex can appear as an energy-nonconserving vertex accompanying an energy-conserving nonflip vertex, provided the left-hand external couplings have sufficient structure. Since the $\tilde{T}_{21}$ vertex is the only one enclosed by a box in Fig. 41, this appears to violate our rule that the nonflip nature of the limit is correlated with that of the vertex. However, the two vertices picked out in Fig. 42 have (at first sight) an ordering ambiguity and should be thought of as an overall disconnected vertex. That the vertex is nonflip is then determined by the presence of the T_{21} vertex.

The ordering ambiguity in the Pomeron diagram of Fig. 42 is of the kind we have discussed earlier. Apparently, the $\tilde{T}_{21}$ vertex can appear to the left or to the right of the T_{21} vertex. However, the helicity-flip vertex $\tilde{T}_{21}$ must be energy nonconserving for the diagram to be consistent with Pomeron unitarity. This is not the case when the $\tilde{T}_{21}$ vertex is to the right of the T_{21} vertex. Therefore there is no diagram corresponding to this possibility. In general, we need not distinguish the ordering of the vertices in Fig. 42 if we select specific Pomeron states in each of the hexagraph channels and regard the combination of disconnected vertices as a single Pomeron interaction. For example, if we consider the two-Pomeron state in each of the channels in Fig. 42, we can regard the $\tilde{T}_{21}$ and T_{21} vertices as combining to produce a single disconnected vertex coupling the three two-Pomeron states. If the Pomerons are replaced by Reggeons, then, as we discussed in Sec. V E, T_{21} contains a nonsense zero, and the ordering is similarly irrelevant.

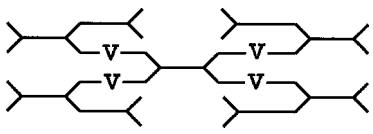

FIG. 43. Hexagraph containing four V subgraphs.

The importance of our discussion of Figs. 41 and 42 will become apparent in our QCD analysis when we are looking for bound-state amplitudes in Sec. VIII. We will be looking for nonflip amplitudes within Reggeon diagrams which also have infrared divergences associated with helicity-flip vertices. The crucial dynamics will be produced by accompanying helicity-flip processes that occur as we have just discussed.

In Sec. III G we noted that internal particle poles occur only in association with internal V subgraphs. The simplest hexagraph that contains an internal scattering amplitude associated entirely with internal Regge-pole particle poles is that illustrated in Fig. 43. In this hexagraph we have added, to each of the Q_i lines of Fig. 36, the same additional vertices that we added to the Q_2 line to obtain the hexagraph of Fig. 39. When Regge poles (with trajectories close to particle poles) are inserted for each of the V lines, the four-particle amplitude enclosed in the thin-line box can be factorized off, first as a four-Reggeon amplitude and then as a four-particle amplitude as the Reggeons generate particle poles. In our QCD analysis the Regge poles we will be looking for will (eventually) be those of bound-state hadrons and the amplitude will be that for Pomeron exchange. The general form of Pomeron and Reggeon diagrams for the hexagraph of Fig. 43 is illustrated in Fig. 44. The internal boxes once again contain $T^{\mathcal{N}}$ and $T^{\mathcal{F}}$ vertices.

H. General helicity amplitudes

It should now be clear how our discussion generalizes to any hexagraph. We isolate a single helicity amplitude by an appropriate helicity-pole limit (which in general will involve a combination of nonflip and flip limits for the relevant u_{ij} variables). Given the $T^{\mathcal{N}}$ and $T^{\mathcal{F}}$ vertices, the associated Pomeron and Reggeon diagrams can then be constructed. A relatively simple example of the more complicated graphs that we will discuss in Sec. VIII is shown in Fig. 45. We again emphasize that while the diagrams are constructed as

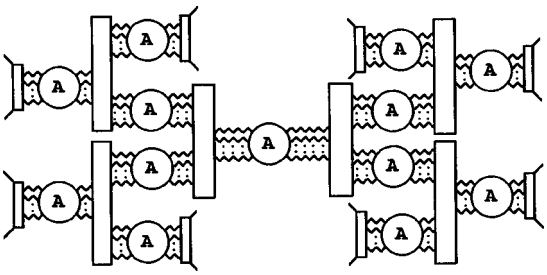

FIG. 44. Structure of Pomeron and Reggeon diagrams for the hexagraph of Fig. 43.

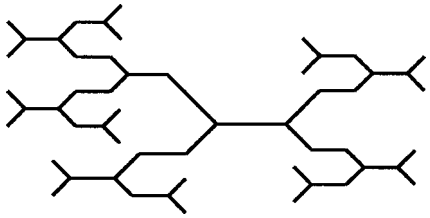

FIG. 45. Relatively simple example of a class of hexagraphs.

two-dimensional integrals in a single transverse plane, when a helicity-flip vertex is involved, a correlated lightlike vector is implicitly added to this plane to obtain the ''physical'' transverse momentum. This is presumably deeply connected with the relationship between the QCD infrared divergence results we will obtain and the zero-mode longitudinal momentum ambiguities of light-cone quantization.

VI. QUARK-REGGEON COUPLINGS AND REGGEON WARD IDENTITIES

In this and the following sections, we will be concerned exclusively with QCD. The Reggeons we consider are specifically the Reggeized gluons of QCD. In the infrared analysis of Sec. VIII, we will discuss setting the gluon mass to zero in some detail. In this section we will simply omit the mass because we want to discuss some of the simplest infrared divergences that occur when quarks are involved. We particularly focus on the interrelation of such divergences with ''Reggeon Ward identities.''

We begin by constructing the lowest-order ''quark-Reggeon'' couplings, i.e., the couplings for multi-Reggeon exchange in on-shell quark scattering. Since a Reggeon reduces to a gluon at $\underline{k}^2=0$, multi-Reggeon amplitudes are, in general, necessarily given by corresponding (on-shell) gluon amplitudes at zero transverse momentum. It follows from the formula for FG amplitudes [10] that the particular (nonsense) Reggeon amplitudes which provide the couplings for Regge cuts can be expressed as integrals of discontinuities, i.e., in terms of on-shell *s*-channel intermediate states. We have not given this formula here because, for multi-Reggeon couplings, it is quite cumbersome. Here we will simply utilize the outcome. That is, the lowest-order contribution of a particular multi-Reggeon exchange to a scattering amplitude is given by that part of the corresponding high-energy multigluon exchange amplitude having the appropriate (Regge cut) signature and in which all intermediate *s*-channel states are put on shell; i.e., no logarithms (of the energy) are generated. This is what we will exploit to calculate Reggeon couplings. We will also note the even-signature color octet case discussed in Sec. V C. In this case there is effectively an ''AFS cancellation'' and the anticipated two-Reggeon cut contribution is replaced by a new Regge pole.

A. Elementary Reggeon couplings

Consider the coupling G_1 of a fast (massive) quark to a single gluon—temporarily ignoring color factors. The quark propagator gives

$$\frac{\gamma\cdot p+m}{p^2-m^2}\underset{p_+\to\infty}{\sim}\frac{\gamma_- p_+ + p_\perp+\cdots}{p^2-m^2}$$

$$\equiv\frac{\gamma_- +\gamma_\perp\cdot(p_\perp/p_+)+0(1/p_+^2)}{\left[p_- -\dfrac{p_\perp^2-m^2}{p_+}\right]}. \quad (6.1)$$

For a quark initially and finally on shell, we remove the $(p^2-m^2)^{-1}$ factor, and so, in lowest-order perturbation theory,

$$G_{1\mu}\sim g\,\gamma_- p_+\gamma_\mu\gamma_- p_+\sim\gamma_- p_+^2 \quad \text{if } \gamma_\mu=\gamma_+. \quad (6.2)$$

Choosing the frame in which the initial quark has $p_\perp=0$, we have $\gamma_- p_+=m$ and obtain

$$G_{1\mu}\sim gmp_+\delta_{-\mu}\equiv G_1 p_+. \quad (6.3)$$

Therefore we anticipate that, in a scattering process, the leading power behavior (for $p_+\to\infty$) will be obtained if the spin of the scattering quark is conserved; that is, there is helicity conservation. In particular, for the scattering via single-gluon exchange of a fast quark with momentum p_1 off a quark with momentum p_2, we obtain the helicity-conserving amplitude

$$g^2m^2p_{1+}\delta_{-\mu}\left[\frac{g_{\mu\nu}}{q_\perp^2}\right]\delta_{\nu+}p_{2-}\sim\frac{g^2m^2s}{q_\perp^2}=G_1^2\,\frac{s}{t}. \quad (6.4)$$

Lorentz invariance requires, of course, that this result hold independently of whether p_{2-} is large or not. If p_{2-} is not large, the spin structure for the fast quark simply picks out, via gluon exchange, the relevant spin component of the slow quark.

Next, we look for the lowest-order two-Reggeon coupling within the amplitude for a fast quark to exchange two gluons. As we described above, we ignore logarithms and place each intermediate-state propagator on shell (via k_- and k_+ integrations). The denominator is thus removed from Eq. (6.1) also for intermediate states, and in analogy with Eq. (6.3), we obtain

$$G_{2\mu_1\mu_2}\sim g^2\gamma_- p_+\gamma_{\mu_1}\gamma_- p_+\gamma_{\mu_2}\gamma_- p_+\sim g^2\gamma_- p_+$$

$$\text{if } \mu_1=\mu_2=+, \quad (6.5)$$

giving the coupling illustrated in Fig. 46(a).

So the quark spin structure is again preserved and the unsignatured (helicity-conserving) amplitude for two-Reggeon exchange has the lowest-order form

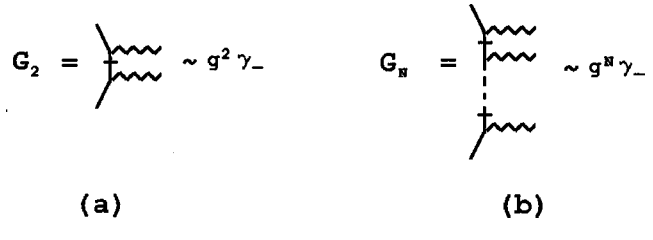

FIG. 46. Quark-Reggeon couplings.

$$A_2 \sim iG_2^2 s \int \frac{d^2\underline{k}_1 d^2\underline{k}_2}{\underline{k}_1^2 \underline{k}_2^2}\, \delta^2[\underline{q}-\underline{k}_1-\underline{k}_2]. \tag{6.6}$$

[Note that we should not cross the gluon lines in obtaining Eq. (6.6)—the corresponding Feynman diagram gives only a real logarithm that we are not interested in.]

In the J plane Eq. (6.6) gives (writing $E=1-J$)

$$A_2(E,q^2) \sim \frac{G_2^2}{E} \int \frac{d^2\underline{k}_1 d^2\underline{k}_2}{\underline{k}_1^2 \underline{k}_2^2}\, \delta^2[\underline{q}-\underline{k}_1-\underline{k}_2]. \tag{6.7}$$

Higher-order contributions convert E^{-1} to a two-Reggeon propagator, and Eq. (6.7) takes the usual two-Reggeon form

$$A_2(E,q^2) \sim G_2^2 \int \frac{d^2\underline{k}_1 d^2\underline{k}_2}{\underline{k}_1^2 \underline{k}_2^2} \frac{\delta^2[\underline{q}-\underline{k}_1-\underline{k}_2]}{[E-\Delta(\underline{k}_1^2)-\Delta(\underline{k}_1^2)]}. \tag{6.8}$$

The Reggeon interactions described in Sec. V C (in particular the full BFKL kernel) also appear as higher-order contributions.

Proceeding in the same way, we obtain the N-Reggeon coupling illustrated in Fig. 46(b),

$$\begin{aligned} G_{N\mu_1\cdots\mu_N} &\sim g^N \gamma_- p_+ \gamma_{\mu_1} \gamma_- p_+ \cdots \gamma_- p_+ \gamma_{\mu_N} \gamma_- p_+ \\ &\sim g^N \gamma_- p_+ \quad \text{if } \mu_1=\mu_2=\cdots=\mu_N=+, \end{aligned} \tag{6.9}$$

and for the unsignatured N-Reggeon amplitude,

$$\begin{aligned} A_N \sim (i)^{N-1} m^2 G_N^2 s \int d^2\underline{k}_1 \cdots d^2\underline{k}_N \\ \times \delta^2[\underline{q}-\underline{k}_1-\underline{k}_2\cdots-\underline{k}_N] \frac{1}{\underline{k}_1^2} \cdots \frac{1}{\underline{k}_N^2}, \end{aligned} \tag{6.10}$$

so that helicity remains conserved. Again, Eq. (6.10) is the lowest-order component of the E-plane amplitude:

$$A_N(E,q^2) \sim G_N^2 \int \frac{d^2\underline{k}_1 \cdots d^2\underline{k}_N}{\underline{k}_1^2 \cdots \underline{k}_N^2} \frac{\delta^2[\underline{q}-\underline{k}_1-\underline{k}_2\cdots-\underline{k}_N]}{[E-\Delta(\underline{k}_1^2)\cdots-\Delta(\underline{k}_N^2)]}. \tag{6.11}$$

Note that, once an overall factor of m^2 is absorbed by the normalization of the scattering states, the Reggeon couplings are independent of the quark mass m. It is also important for the discussion in the next section that we need take only one of the scattering quarks to be fast in order to derive the kinematic structure of the lowest-order multi-Reggeon exchange diagrams. The kinematic structure of the fast quark coupling to the exchanged gluons always imposes the same kinematic structure on the slow quark couplings.

Positive (or negative) signatured amplitudes are obtained by adding (or subtracting) the corresponding CPT twisted amplitude. That is, we make a CPT transformation on one vertex or the other to which the multi-Reggeon state is coupled and add (or subtract) the amplitude obtained. For the two-Reggeon state we replace the fast quark coupling G_2 of a quark with a particular helicity by the coupling of a fast antiquark with the opposite helicity. Helicity conservation makes the parity part of the twist trivial since parity conservation implies that the vertices for both helicities are equal. Consequently, the only effect of the CPT transformation is to replace the color factor of the quark by that for the antiquark. For an Abelian theory (QED) this simply changes the sign of the charge. As a result, the exchange of an even (odd) number of Reggeons contributes to the even (odd) signatured amplitude. This is the normal signature rule for Regge cuts. (Of course, the photon is not actually Reggeized in QED.) When color factors are introduced, the CPT twist also involves (color) charge conjugation. In this case, provided helicity is conserved, signature can be identified with color charge parity.

B. Color factors

We define the color charge conjugation operation on the color matrix of the gluon field by

$$A^i_{\alpha\beta} \rightarrow -A^i_{\beta\alpha}. \tag{6.12}$$

The minus sign indicates an intrinsic odd color parity for the gluon. Quarks are transformed into antiquarks. We will discuss color parity for quarks in more detail in our second paper. For the purposes of this paper, it is sufficient that color charge conjugation simply reverses the order of multiplication of color matrices in internal quark loops.

For SU(2) color, quark-quark scattering (via two-gluon exchange and higher) contains two t-channel color representations; i.e., in the t channel,

$$2 \otimes 2 \rightarrow 1 \oplus 3. \tag{6.13}$$

The singlet representation is symmetric (even color parity), while the triplet is antisymmetric (odd color parity). It is well known [11,18] that at next-to-leading logarithmic order the singlet amplitude contains the two-Reggeon cut, while the triplet contains only the Reggeizing gluon. This follows from the bootstrap cancellation of Fig. 27. For gluon-gluon scattering we can have

$$3 \otimes 3 \rightarrow 1 \oplus 3 \oplus 5, \tag{6.14}$$

and the $I=2$, symmetric, five-dimensional representation also gives a two-Reggeon cut. For three-gluon exchange and higher, helicity conservation implies that in quark-quark scattering, the odd-number Reggeon exchanges appear in the color triplet channel while the even-number exchanges appear in the color singlet channel.

For SU(3) color, quark-quark scattering contains three t-channel representations:

$$3 \otimes \bar{3} \rightarrow 1 \oplus \frac{1}{2}(8_a \oplus 8_s). \tag{6.15}$$

Again (at next-to-leading logarithmic order), the symmetric singlet gives a two-Reggeon cut and the antisymmetric octet gives the Reggeized gluon. However, as we noted in our discussion following Fig. 27, in the symmetric octet channel

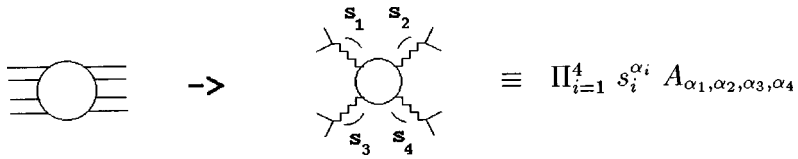

FIG. 47. Reggeon amplitude extracted from the eight-particle amplitude.

the kernel is identical with the Reggeizing antisymmetric kernel and there is an ''AFS cancellation.'' That is, the two-Reggeon cut is replaced by an even-signature Regge pole [20]. The lowest-order amplitude is still Eq. (6.7), but in higher orders it is converted to the form

$$A_2(E,q^2)\sim \frac{J_1(q^2)}{E-g^2q^2J_1(q^2)}, \tag{6.16}$$

where $J_1(q^2)$ is given by Eq. (5.19). Ultimately, this will be very important for our construction of the QCD Pomeron. It will also be important that, when helicities are not conserved, the TCP twisting process involves both parity and color charge parity. In general, helicity conservation implies that even-signature combinations of odd-signature and even-signature Reggeons will appear in both the singlet and 8_s channels, while the odd-signature combinations will appear only in the 8_a channel.

It is clear from Eqs. (6.6) and (6.10) that Reggeon diagrams involving the scattering of on-shell quarks are infrared divergent with the divergence arising from the integral over (gluon) transverse momenta. This divergence is present even when the Reggeon state carries zero color. It is important to understand the origin of this divergence and how it relates to gauge invariance. For this purpose we now discuss the ''Reggeon Ward identities'' that, for Reggeon amplitudes, are a direct requirement of gauge invariance.

C. Reggeon Ward identities

Reggeon amplitudes can be defined directly in terms of analytically continued partial-wave amplitudes or by the relevant multi-Regge or helicity pole limit. In terms of multiparticle partial-wave amplitudes, it is straightforward to write

$$a_{J_1,J_2,J_3,J_4,J_5,\ldots} \xrightarrow[J_i\to\alpha_i,\ i=1,\ldots,4]{} \prod_{i=1}^{4}\frac{\beta_i}{(j_i-\alpha_i)}A_{\alpha_1,\alpha_2,\alpha_3,\alpha_4}(J_5,\ldots) \tag{6.17}$$

and to define $A_{\alpha_1,\alpha_2,\alpha_3,\alpha_4}(j_5,\ldots)$ as a multi-Reggeon amplitude. (For simplicity, we omit the labels N_i, which give the differences between angular momenta and helicity labels in the FG continuation involved.) Multi-Reggeon scattering amplitudes can be defined in momentum space by writing a SW representation involving the remaining J_i or by simply taking a multi-Regge limit in which the Regge poles involved are exchanged. As we have illustrated in previous sections, we can define such limits in terms of invariants and also in terms of light-cone momenta in a particular Lorentz frame.

To make our general discussion specific, we consider an eight-point function, as in Fig. 47, and suppose that the multi-Regge or helicity-pole limit considered involves $s_i\to\infty$, $i=1,\ldots,4$, where each s_i is associated with a particular Reggeon as illustrated. Consider the Reggeon associated with s_1. We can choose a Lorentz frame in which the limit $s_i\to\infty$ is defined by $p_+\to\infty$, $k\to\underline{k}$, where p and k are the momenta labeled in Fig. 48 and $\underline{k}$ is the transverse momentum carried by the Reggeon. Since the four-momentum k is reduced to a transverse momentum $\underline{k}$ by the Regge limit, the further limit $\underline{k}\to 0$ is equivalent to setting $k=0$. Because of Reggeization, the Reggeon amplitude must, as illustrated, give a $k=0$ gluon amplitude. Since the Reggeon amplitude is embedded in an on-shell S-matrix amplitude, we obtain the zero-momentum limit of the amplitude ($\langle A_\mu(k)\cdots\rangle$) for an off-shell gluon to couple to an S-matrix element.

Gauge invariance implies directly that the gluon amplitude $\langle A_\mu(k)\cdots\rangle$ satisfies the simple Ward identity [25]

$$k_\mu\langle A_\mu(k)\cdots\rangle=0. \tag{6.18}$$

Differentiating this identity (treating each component of k as independent), we obtain

$$\langle A_\mu\cdots\rangle+\left[\frac{\partial\langle A_\nu\cdots\rangle}{\partial k_\mu}\right]_{k=0}k_\nu=0$$
$$\Rightarrow\langle A_\mu\cdots\rangle\xrightarrow[k_\mu\to 0]{}0 \quad \text{if}\quad \left[\frac{\partial\langle A_\nu\cdots\rangle}{\partial k_\mu}\right]_{k=0}\to\infty, \tag{6.19}$$

implying that the gluon amplitude and also (if there is no subtlety with the Regge limit) the Reggeon amplitude should vanish at zero transverse momentum. This is what we refer

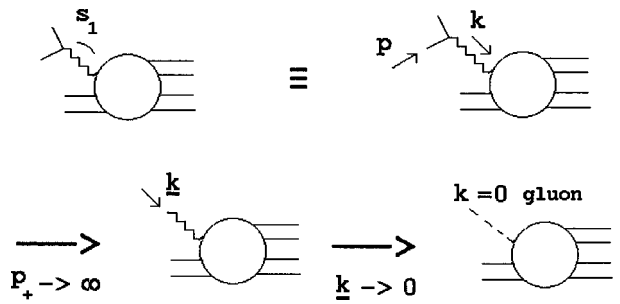

FIG. 48. Reduction of a Reggeon amplitude to a gluon amplitude.

to as a Reggeon Ward identity. By similarly defining the additional $s_i \to \infty$ limits as light-cone limits, the argument can (*a priori*) be extended to an arbitrary number of Reggeon transverse momenta vanishing.

In general, therefore, (massless) Reggeon amplitudes vanish linearly in $\underline{k}$ when any transverse momentum $\underline{k} \to 0$. This is a direct consequence of gauge invariance. It is straightforward to check that Γ_{22} defined by Eqs. (5.20) and (5.21) has this property when $M=0$. However, if the quark-Reggeon couplings discussed above had this property, the infrared divergences of Eqs. (6.6) and (6.11) would not occur. So why do the quark-Reggeon couplings not satisfy Reggeon Ward identities?

D. On-shell quarks

In parallel with our discussion of fast quarks above, we consider the coupling of a gluon to on-shell quarks in the form

$$\Gamma_\mu(p,p') = (\gamma\cdot p + m)\gamma_\mu(\gamma\cdot p' + m). \tag{6.20}$$

The Ward identity (6.18) is easily shown to hold:

$$\begin{aligned}(p-p')_\mu \Gamma_\mu(p,p') &= (\gamma\cdot p + m)(\gamma\cdot p - m - \gamma\cdot p + m)(\gamma\cdot p' + m) \\ &= (p^2 - m^2)(\gamma\cdot p' + m) - (\gamma\cdot p + m)(p'^2 - m^2) \\ &= 0,\end{aligned} \tag{6.21}$$

after applying the on-shell condition for the initial and final quarks.

To compare with the argument of the previous subsection, we should evaluate the Reggeon coupling G_1 by calculating quark-quark scattering in a frame in which one quark has infinite momentum, but the momentum of the quark we are considering has finite momentum. The fast quark can then be identified with the line carrying momentum p in Fig. 48 and the finite-momentum quark vertex identified with the remaining amplitude that satisfies the Reggeon Ward identity. Therefore we identify the quark momentum p in Eq. (6.20) with p_2 in Eq. (6.9) and take

$$\begin{aligned} p \equiv p_2, \quad p' \equiv p_2 + k, \\ p_2 = (p_{2+}, p_{2-}, p_{22}, 0), \\ k = (0, k_-, k_2, k_3). \end{aligned} \tag{6.22}$$

The remnant of the fast quark Regge limit is that $k_- \to 0$. *A priori*, since all the momenta involved are finite, Eq. (6.19) goes through straightforwardly. However, since both p_2 and p' are on mass shell,

$$p_2^2 = m^2, \quad (p_2+k)^2 = m^2 \to 2p_{2+}k_- = 2p_{22}k_2 + k_3^2. \tag{6.23}$$

Therefore, if we keep p_2 finite, we cannot treat k_- and the components of $\underline{k}$ as independent variables. In particular,

$$\left[\frac{\partial k_3}{\partial k_-}\right]_{k=0} \sim (k_-)^{-1/2}, \tag{6.24}$$

so that

$$\left[\frac{\partial}{\partial k_-}\Gamma_3\right]_{k=0} \sim \frac{\partial k_3}{\partial k_-}\frac{\partial}{\partial k_3}\Gamma_3 \sim k_-^{-1/2}\frac{\partial}{\partial k_3}\Gamma_3, \tag{6.25}$$

implying that

$$G_1 \equiv \Gamma_+ \sim k_3 \frac{\partial}{\partial k_-}\Gamma_3 \sim \frac{\partial}{\partial k_3}\Gamma_3 \underset{k\to 0}{\not\to} 0. \tag{6.26}$$

Since Eq. (6.23) also requires $k_- \sim k_2$, the transverse component Γ_2 similarly satisfies

$$\Gamma_2 \sim k_3 \frac{\partial}{\partial k_2}\Gamma_3 \sim \frac{\partial}{\partial k_3}\Gamma_3 \sim \Gamma_+. \tag{6.27}$$

In the gluon Ward identity the contributions of Γ_+ and Γ_2 cancel, while the Regge limit picks out just Γ_+.

Clearly, the mass-shell constraint conflicts with the derivation of the Reggeon Ward identity. Note that, since G_N is given by a sequence of on-shell quark scatterings, this coupling also need not vanish when any, or all, of the $\underline{k}_i \to 0$. We conclude that the Reggeon Ward identity does not hold for Reggeons coupling directly to on-shell quarks—even though the related gluon Ward identity implied by gauge invariance still holds. Conversely, when Reggeons couple through off-shell quarks or gluons, as is in general the case, the Reggeon Ward identities follow directly from gluon Ward identities. (Note that all of the above discussion goes through straightforwardly when the quark mass m is set to zero.)

E. Reggeon Ward identities in Reggeon diagrams

The vanishing of massless Reggeon interactions at $\underline{k}=0$, as a result of the Reggeon Ward identities, is crucial for the infrared properties of Reggeon diagrams when the gluon is massless. As elaborated in [22], the infrared finiteness of the BFKL kernel, as well as next-to-leading order corrections, is a direct consequence of this property. Explicit next-to-leading order calculations have verified [19] that the Reggeon Ward identities hold also for the quark production amplitudes that produce next-to-leading order quark loop interactions in the BFKL kernel. From the above discussion it is clear, however, that we could expect a violation of the Reggeon Ward identities (but not the gluon Ward identities) if there is an infrared divergence within a Reggeon interaction due directly to a loop of on-shell quarks. The Reggeon interaction would then involve the on-shell quark couplings discussed above.

Note that a violation of the Reggeon Ward identities cannot be produced by a loop of on-shell (massless) gluons. This is because we can use t-channel helicities to describe the polarizations of the on-shell gluons. Since a Reggeon, at zero $\underline{k}$, is also a t-channel gluon, it follows from helicity conservation that the Reggeon cannot couple to a pair of on-shell gluons in the loop. Hence the Reggeon must decouple from

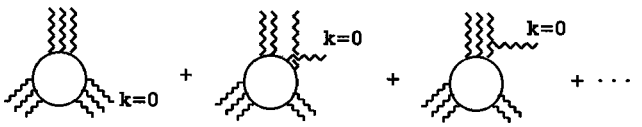

FIG. 49. Ward identity diagram sum.

the gluon loop at $\underline{k}=0$. Consequently, any divergence due to an internal loop of on-shell quarks cannot be canceled by an internal gluon loop. Not surprisingly perhaps, a quark loop divergence occurs only in very special situations (related to the infrared triangle anomaly) and is a subtle phenomenon to isolate. The purpose of the remaining sections is to establish that such a phenomenon can indeed occur.

We can describe how the Reggeon Ward identities are normally satisfied diagrammatically (for quark-loop interactions of the kind that we are interested in) as follows. It is well known that to obtain the gluon Ward identity (6.18) for a multigluon amplitude it is necessary, at the Feynman diagram level, to sum diagrams in which the gluon involved is attached in all possible ways to the remainder of the diagram. This is illustrated for a class of diagrams containing a quark loop in Fig. 49. (Diagrams of this kind will be of particular interest to us in the next section.) If some or all of the gluons are replaced by Reggeons, then, in general, a similar sum over all related Reggeon-Feynman diagrams gives the Reggeon Ward identity. The number of diagrams involved is much smaller if we generalize the argument we gave above for putting intermediate-state particles on shell to obtain particle-Reggeon couplings. To obtain a multi-Reggeon coupling from diagrams such as those of Fig. 49, we first consider which hexagraph is involved and then put corresponding quark lines on shell to obtain the relevant multiple discontinuity. We will not elaborate the argument for this procedure—which we follow through in more detail in the next section—but note only that it is directly due to the fact that multiparticle FG amplitudes are expressed in terms of the multiple discontinuities of the hexagraph involved. (From the discussion of Secs. III and IV, we have seen how multi-Regge behavior explicitly reflects the hexagraph cut structure of amplitudes.)

As an important example, suppose we replace all the gluons in the first diagram of Fig. 49 by Reggeons and embed the diagram in a six-quark amplitude, as illustrated in Fig. 50. (We evaluate this diagram explicitly in the next section.) If we associate this diagram with the hexagraph of Fig. 17, the cuts shown as dashed lines in Fig. 50 correspond to the triple discontinuity of Fig. 16(b). Since some quarks remain off shell, after the triple discontinuity is taken, Reggeon Ward identities should hold after we sum over all related diagrams having the same triple discontinuity. The most direct way to show this is to follow Fadin and Lipatov [19] and introduce Reggeon-Reggeon-gluon effective vertices in addition to the quark-Reggeon couplings we have already introduced. The results of [19] can then be applied to show that, provided the quark-loop integration introduces no problems, the diagrams of Fig. 51 combine to give a Reggeon Ward identity zero as $k\rightarrow 0$. (k is the transverse momentum carried by a single Reggeon.) In the first two diagrams all Reggeons couple directly to the quark loop. In the third diagram there is a gluon line coupling a two-Reggeon–gluon ''effective vertex'' to the quark loop.

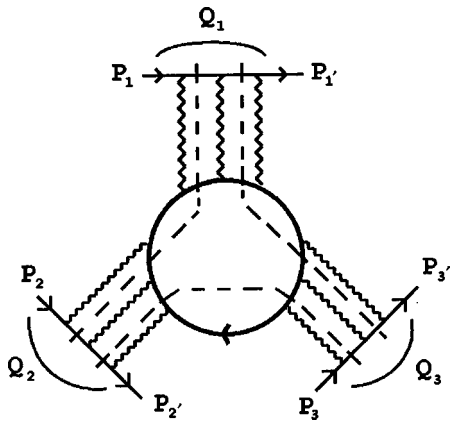

FIG. 50. Triple discontinuity.

F. Pauli-Villars regulator quarks

There is a very important difference between the quark-loop Reggeon interaction vertices appearing in Figs. 50 and 51 and those appearing in elastic scattering [19]. In both cases the process of obtaining Reggeon vertices from Feynman diagrams involves putting quark lines on shell. However, for a quark loop contributing as an elastic scattering interaction, there is always a sufficient number of discontinuities taken through the loop to effectively reduce the dimension of the loop integration. In contrast, in the example of Fig. 50 the quark lines can be put on shell by using only the longitudinal momentum integrations for the other loops involving Reggeized gluons. Consequently, the quark loop remains as a four-dimensional integration. This feature is associated with the fact that the multi-Regge limit of interest can be defined with the complete quark loop at rest (as we will explicitly do in the next section).

As the quark lines are put on shell, the ultraviolet convergence of the quark loop is significantly reduced. In the first two diagrams of Fig. 51, there are three quark propagators remaining off shell, while in the third diagram only two quark propagators remain off shell. Therefore in all three diagrams the quark loops are power divergent with the third diagram being particularly badly divergent. Although higher-order diagrams may provide additional convergence, there is no *a priori* reason why this should be the case. Because there is no loss of dimension in the loop integration, in general we can expect that the reduced quark loops (produced by the multi-Regge kinematics we discuss) are no more convergent than the quark loops encountered in the original definition of the theory. This implies that a regulator is necessary to define these loops. While a regulator can straightforwardly be applied in the definition of the theory, we cannot do this here. In our case, the need for a regulator implies that the multi-Regge behavior of the underlying Feynman diagrams is not correctly given by the reduction to Reggeon diagrams that we are implicitly assuming.

If the reduction of Feynman diagrams to a Reggeon diagram gives infinite coefficients involving power-divergent

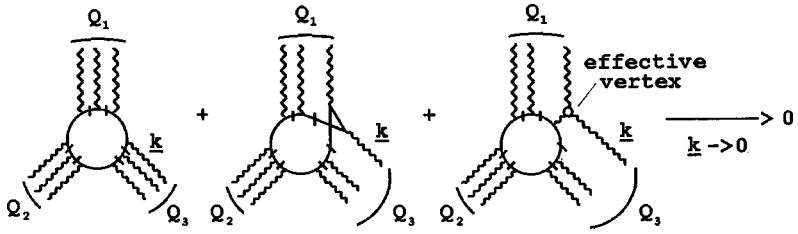

FIG. 51. Quark-loop couplings giving a Reggeon Ward identity.

subdiagrams, then the multi-Regge behavior of the underlying diagrams must be larger by a power than that of the Reggeon diagram. This phenomenon provides a real threat to the unitarity boundedness of the theory. (We will return to the significance of this in our second paper.) As will become clear from our discussion in the next two sections, it is the infrared contribution of the triangle diagram which will eventually dominate the dynamical picture that we develop. However, we would like a starting point in which we have both gauge invariance and a finite Reggeon diagram formalism. This requires a definition of the contribution of quark loops to Reggeon interactions which, when the quarks are massive, is finite and satisfies the Reggeon Ward identities. To achieve this we introduce large mass Pauli-Villars regulator ''quarks,'' in addition to the light quarks that we ultimately take to be massless. The regulator quark loops have the opposite sign to the physical light-quark loops. To ensure there are no Reggeon diagram ultraviolet divergences, the safest procedure is to keep the regulator mass finite. In the following we will make only occasional reference to the regulator quark mass m_λ, which will provide a finite ultraviolet cutoff in the quark sector. Its presence means that, in the quark sector, the theory is not unitary at this mass scale. We will ultimately remove m_λ after we have extracted infrared divergences associated with the massless quarks.

With the Pauli-Villars cutoff, the Reggeon Ward identities will be satisfied straightforwardly, as illustrated in Fig. 51, as long as the light-quark mass is nonzero. When the quarks are massless, an infrared divergence problem arises, which leads to another important difference between the diagrams of Fig. 51. The three off-shell propagators in the first two diagrams will generate a triangle Landau singularity, enhancing zero-transverse-momentum quark threshold singularities. In the first diagram this singularity occurs when

$$Q_1, Q_2, Q_3 \to 0. \tag{6.28}$$

In the third diagram there is no triangle singularity. In the next two sections we will see how the presence of the triangle singularity produces a violation of the Reggeon Ward identities when the zero-quark-mass limit is taken. We will also see that the presence of the ultraviolet regulator sector plays an important role in the way the limit is realized.

VII. TRIPLE-REGGE HELICITY-FLIP VERTICES

In this section we study Feynman and Reggeon diagrams of the kind discussed at the end of the last section, all of which involve a quark loop. We will study such diagrams in the variety of triple-Regge limits discussed in Sec. IV. Our aim is to extract parts of the helicity-flip Reggeon vertices $T^{\mathcal{F}}_{m'n'r'}$ discussed in Sec. V which have special (singular) zero-quark-mass properties with respect to the Reggeon Ward identities. As anticipated in the last section, we initially consider particular Feynman diagram contributions involving on-shell quarks and then deduce the structure of corresponding Reggeon couplings. We will build up to diagrams with the complexity of Fig. 50. We begin, however, with the diagram of Fig. 52 involving single-gluon exchange.

A. Feynman diagram limits

Consider the behavior of Fig. 52 in the limits defined in Sec. IV B. Since each limit is defined in terms of fast external quarks, we obtain a contribution if we simply apply Eq. (6.1) to these quarks and leave the quark loop to be evaluated at finite momentum. Initially, we omit color factors and take the quark mass $m \neq 0$. In this case the quark loop gives (apart from a normalization factor) the usual vertex function

$$\Gamma_{\mu_1\mu_2\mu_3}(q_1,q_2,q_3,m) = i\int \frac{d^4k\ \mathrm{Tr}\{\gamma_{\mu_1}(\not q_3+\not k+m)\gamma_{\mu_2}(\not q_1+\not k+m)\gamma_{\mu_3}(\not q_2+\not k+m)\}}{[(q_1+k)^2-m^2][(q_2+k)^2-m^2][(q_3+k)^2-m^2]}. \tag{7.1}$$

(Since we implicitly consider Pauli-Villars regulator quarks to be present as we discussed in the last section, we ignore ultraviolet divergence problems.) Denoting the full amplitude corresponding to Fig. 52 by T^{111} and using Eq. (6.1), we obtain a result analogous to Eq. (6.4) for the limit L_1, i.e.,

$$T^{111} \to T^{111}_{L_1} \sim g^6 \frac{p_1 p_2 p_3}{t_1 t_2 t_3} \Gamma_{1^+2^+3^+}(q_1,q_2,q_3), \tag{7.2}$$

where $t_1 = Q_1^2$, etc., and $\Gamma_{1^+2^+3^+}$ is defined by $\gamma_{i^+} = \gamma_0$

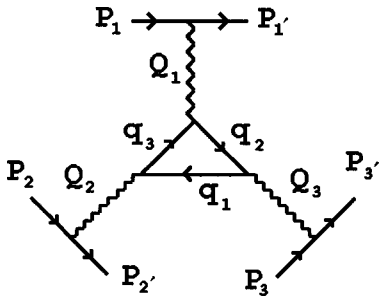

FIG. 52. Triple-gluon vertex.

$+\gamma_i$, $i=1,2,3$. In this section, for simplicity, we continue to omit the gluon mass. For the limit L_2 we similarly obtain

$$T^{111}\to T^{111}_{L_2}\sim g^6\,\frac{p_1p_2p_3}{t_1t_2t_3}\,\Gamma_{1^+1^-3^+}(q_2',q_2,q_3), \quad (7.3)$$

and for the limit L_3

$$T^{111}\to T^{111}_{L_2}\sim g^6\,\frac{p_3}{t_1t_2t_3}\,\Gamma_{1^+1^+3^+}(q_2',q_2,q_3). \quad (7.4)$$

Our further discussion of infrared divergences and Reggeon Ward identities in the next section will center on that part of the vertex functions (7.2)–(7.4) that behaves nonuniformly with respect to the two further limits

$$\text{(i)}\ \ q_1\sim q_2\sim q_3\sim Q\to 0, \quad \text{(ii)}\ \ m\to 0. \quad (7.5)$$

We will be studying effects that are closely related to the infrared triangle anomaly [26]. At first sight it might seem that we should not encounter such behavior. First, Eqs. (7.2)–(7.4) involve $\Gamma_{\mu_1\mu_2\mu_3}$ evaluated with (transverse) momenta orthogonal to the appropriate (light-cone) Lorentz indices. Therefore Eqs. (7.2)–(7.4) do not contribute to the divergence of the triangle graph in which the anomaly resides. However, as we discussed in Sec. VI D, if on-shell quarks are involved, transverse and longitudinal components of vertex functions are linked by the underlying gluon Ward identities, even though the Regge limit picks out just the longitudinal component. Consequently, if the transverse component contains an infrared divergence of the triangle graph, associated with the anomaly, in which the quarks are placed on shell, this will also appear in the longitudinal component. Even so, since only vector (rather than axial vector) couplings appear in $\Gamma_{\mu_1\mu_2\mu_3}$, we again would not expect the anomaly to appear. In fact, as we build up multi-Reggeon interactions in the following, we will consider (originally) nonlocal couplings to the triangle graph that are ''axial vector like'' in the Regge limit, infrared, region of interest.

The most singular behavior in the the limit (i) involves all three denominator poles and the minimum internal momentum dependence from the numerator. Since the trace of an odd number of γ matrices vanishes, the only m dependence of the numerator of $\Gamma_{\mu_1\mu_2\mu_3}$ comes from the terms containing a factor of m^2. Denoting this ''m^2 part'' by $\Gamma_{\mu_1\mu_2\mu_3,m^2}$, we have

$$\Gamma_{\mu_1\mu_2\mu_3,m^2}\underset{Q\to 0}{\to} im^2\int\frac{d^4k}{[k^2-m^2]^3+O(Q)}$$
$$\times\mathrm{Tr}\{\gamma_{\mu_1}(\not q_3+\not k)\gamma_{\mu_2}\gamma_{\mu_3}$$
$$+\gamma_{\mu_1}\gamma_{\mu_2}(\not q_1+\not k)\gamma_{\mu_3}$$
$$+\gamma_{\mu_1}\gamma_{\mu_2}\gamma_{\mu_3}(\not q_2+\not k). \quad (7.6)$$

In the leading term, the numerator terms that are odd in k vanish after integration and so

$$\Gamma_{\mu_1\mu_2\mu_3,m^2}\underset{Q\to 0}{\to}\Gamma_{\mu_1\mu_2\mu_3,0}(q_1,q_2,q_3)$$
$$\equiv iR\ \mathrm{Tr}\{\gamma_{\mu_1}\not q_3\gamma_{\mu_2}\gamma_{\mu_3}+\gamma_{\mu_1}\gamma_{\mu_2}\not q_1\gamma_{\mu_3}$$
$$+\gamma_{\mu_1}\gamma_{\mu_2}\gamma_{\mu_3}\not q_2\}, \quad (7.7)$$

where

$$R=m^2\int\frac{d^4k}{[k^2-m^2]^3}=\int\frac{d^4y}{[y^2-1]^3}. \quad (7.8)$$

Clearly,

$$\Gamma_{\mu_1\mu_2\mu_3,0}(q_1,q_2,q_3)\underset{Q\to 0}{\sim}Q. \quad (7.9)$$

If we reverse the order of the limits (i) and (ii), we obtain, instead of Eq. (7.7),

$$\Gamma_{\mu_1\mu_2\mu_3,m^2}\underset{m\to 0}{\sim}m^2\to 0. \quad (7.10)$$

If we consider T^{111} as an isolated Feynman diagram, defined directly in the massless theory, Eq. (7.7) will not be present. However, we will shortly consider Reggeon interactions containing $\Gamma_{\mu_1\mu_2\mu_3,m^2}$. In the next section we will see that the nonuniformity of Eqs. (7.7) and (7.10) implies that if the Reggeon Ward identities are satisfied for $m\neq 0$, then $\Gamma_{\mu_1\mu_2\mu_3,0}$ is present in these interactions when $m=0$. Note that the presence of m^2 in the numerator of $\Gamma_{\mu_1\mu_2\mu_3,m^2}$ indicates two helicity flips of the quarks in the loop. That the helicity-flip processes do not decouple in the limiting process, where the limit (i) is taken before the limit (ii), is clearly a consequence of the triangle singularity infrared divergence produced as all three internal quark propagators go on shell. The presence of this divergence is therefore crucial.

Consider now the contribution of Eq. (7.7) to Eqs. (7.2)–(7.4). In Eq. (7.2) we will have a contribution

$$T^{111}_{L_1,0}\sim g^6\,\frac{p_1p_2p_3}{t_1t_2t_3}\,\Gamma_{1^+2^+3^+,0}(q_1,q_2,q_3), \quad (7.11)$$

where

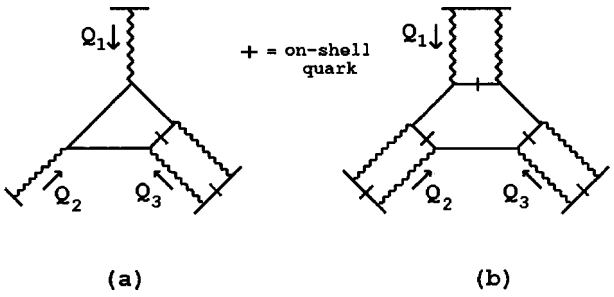

FIG. 53. Triple couplings involving two-gluon exchange.

$$\Gamma_{1^+2^+3^+,0}\sim(\mathrm{Tr}\{\gamma_{1^+}\gamma_{2^+}\gamma_1\gamma_{3^+}\}q_1+\mathrm{Tr}\{\gamma_{1^+}\gamma_{2^+}\gamma_{3^+}\gamma_2\}q_2 + \mathrm{Tr}\{\gamma_{1^+}\gamma_3\gamma_{2^+}\gamma_{3^+}\}q_3) \sim(q_1+q_2+q_3). \tag{7.12}$$

Similarly, in Eq. (7.3) we will have a contribution

$$T^{111}_{L_2,0}\sim\frac{p_1p_2p_3}{t_1t_2t_3}\,\Gamma_{1^+1^-3^+,0}(q_2',q_2,q_3) \sim\frac{p_1p_2p_3}{t_1t_2t_3}\,\mathrm{Tr}\{\gamma_{1^+}\gamma_{1^-}\gamma_2\gamma_{3^+}\}q_2' +(\mathrm{Tr}\{\gamma_{1^+}\gamma_{1^-}\gamma_{3^+}\gamma_2\}q_2+\mathrm{Tr}\{\gamma_{1^+}\gamma_3\gamma_{1^-}\gamma_{3^+}\}q_3) \sim\frac{p_1p_2p_3}{t_1t_2t_3}\,q_3, \tag{7.13}$$

and in Eq. (7.4) we will have

$$T^{111}_{L_3,0}\sim\Gamma_{1^+1^+3^+,0}(q_2',q_2,q_3)\sim\mathrm{Tr}\{\gamma_{1^+}\gamma_{1^+}\gamma_2\gamma_{3^+}\}q_2' +\mathrm{Tr}\{\gamma_{1^+}\gamma_{1^+}\gamma_{3^+}\gamma_2\}q_2+\mathrm{Tr}\{\gamma_{1^+}\gamma_3\gamma_{1^+}\gamma_{3^+}\}q_3 =0. \tag{7.14}$$

We conclude from Eq. (7.11) that when the additional limits (7.5) are taken after the triple-Regge limit, there is a nonzero contribution of the helicity flip process (7.7). There are three terms. Equation (7.13) suggests that just one of the three terms appearing in the triple-Regge limit appears in the helicity-flip helicity-pole limit. [We will see shortly that this is the case. It cannot be straightforwardly deduced from Eqs. (7.11) and (7.13) since we redefined the momentum components of the Q_i in going from one limit to the other.] The result of Eq. (7.14) shows that there is no contribution of the helicity flip process (7.7) in the simple nonflip helicity-pole limit.

Next, we consider some higher-order Feynman diagrams in order to determine how they contribute to higher-order Reggeon couplings. Suppose first that we replace one or more of the gluons in Fig. 52 by two-gluon exchange, as illustrated in Fig. 53. We again evaluate the quark loop at finite momentum. Our interest in two-gluon states is to extract two-Reggeon (Regge cut) couplings and so we calculate the diagram with on-shell intermediate states as illustrated. (We can justify this by evaluating the appropriate multiple discontinuity to calculate the relevant FG amplitude or we can simply suppose that we have carried out the related longitudinal integrations.) Denoting now the full amplitude for Fig. 53(a) by T^{112}, we obtain for the limit L_1, in analogy with Eq. (6.6),

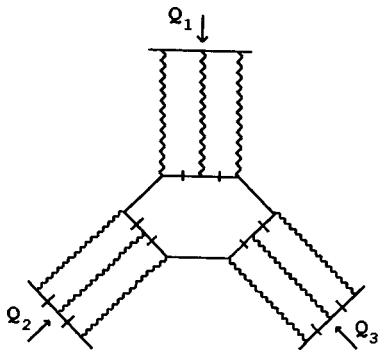

FIG. 54. Triple vertex for three gluons.

$$T^{112}\to T^{112}_{L_1}\sim ig^8\,\frac{p_1p_2p_3}{t_1t_2}\,J_1(t_3)\Gamma_{1^+2^+3^+}(q_1,q_2,q_3), \tag{7.15}$$

and so again, after the further limits (7.5) are taken, there is a contribution of the form (7.7), i.e.,

$$T^{112}_{L_i,0}\sim -it_3J_1(t_3)T^{111}_{L_i,0},\quad i=1,2,3. \tag{7.16}$$

Denoting the full amplitude for Fig. 53(b) by T^{222}, we similarly obtain

$$T^{222}\to T^{222}_{L_1}\sim(i)^3g^{12}p_1p_2p_3J_1(t_1)J_1(t_2)J_1(t_3) \times\Gamma_{1^+2^+3^+}(q_1,q_2,q_3), \tag{7.17}$$

and so

$$T^{222}_{L_i,0}\sim -it_1t_2t_3J_1(t_1)J_1(t_2)J_1(t_3)T^{111}_{L_i,0},\quad i=1,2,3. \tag{7.18}$$

We can continue adding gluons (as we did for single-quark couplings in the last section) and obtain corresponding results. The diagram of Fig. 54 contains the triple coupling of three-gluon states which we anticipate will give the first multi-Reggeon coupling appearing in Fig. 51. This coupling will be very important in the following.

In this case we obtain, as above, for the limit L_1,

$$T^{333}\to T^{333}_{L_1}\sim i^6g^{16}p_1p_2p_3J_2(t_1)J_2(t_2)J_2(t_3) \times\Gamma_{1^+2^+3^+}(q_1,q_2,q_3), \tag{7.19}$$

where (continuing to omit normalization factors)

$$J_2(q^2)=\int\frac{d^2k}{(k-q)^2}\,J_1(k^2) \tag{7.20}$$

and, in all the L_i limits,

$$T^{333}_{L_i,0}\sim -t_1t_2t_3J_2(t_1)J_2(t_2)J_2(t_3)T^{111}_{L_i,0},\quad i=1,2,3. \tag{7.21}$$

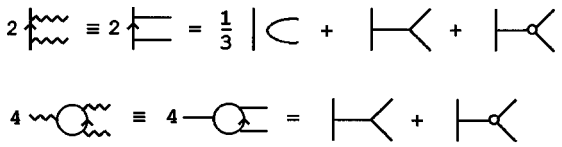

FIG. 55. Color factors for quark-gluon couplings.

Note that in extracting the $T^{333}_{L_i,0}$ from the diagram of Fig. 54, we have put on shell (the denominators of) all those quark propagators that we had not already put on shell in converting the multigluon coupling to a multi-Reggeon coupling. Therefore the $T^{333}_{L_i,0}$ couplings actually involve a loop of on-shell quark propagators and so, from the discussion of the last section, might be anticipated to be associated with a violation of the Reggeon Ward identities. To establish that such contributions actually appear in multi-Reggeon couplings, we must first consider the color factors involved.

B. Color factors

In this subsection we discuss the color factors that should be added to the diagrams considered in the last subsection. We use the tensor notation introduced in Fig. 26. The quark relations shown in Fig. 55 are then sufficient to evaluate the color factors for any number of gluons coupling to a single-quark loop. We can form multigluon (multi-Reggeon) states with color 1, 8_a, and 8_s by combining δ, f, and d tensors appropriately with gluon fields. The color parity of such a state will then be given by a product of factors of (-1) for each gluon field and (-1) for each f tensor.

From the second relation of Fig. 55, the quark loop in Fig. 52 gives a color factor proportional to

$$d_{i_1 i_2 i_3} + i f_{i_1 i_2 i_3}, \tag{7.22}$$

where i_1 is the color label for the gluon carrying momentum Q_1, etc. Consider next the addition of the diagram of Fig. 56 (which is the only other topologically distinct quark-loop three-gluon interaction). The diagram of Fig. 56 differs from that of Fig. 52 by permutation of the color matrices, which (within the trace) is the same as reversal of the direction for multiplication. The result is complex conjugation of the color factor. Since the sign of the q_i is also reversed, Fig. 56 can, as illustrated, be obtained directly from Fig. 52 by replacing the quark loop by an antiquark loop. For the $O(m^2)$ part with which we are concerned, the two diagrams combine to give

$$T^{111}_{L_1,0} \sim g^6 \frac{p_1 p_2 p_3}{t_1 t_2 t_3} [(d_{i_1 i_2 i_3} + i f_{i_1 i_2 i_3})(q_1+q_2+q_3) - (d_{i_1 i_2 i_3} - i f_{i_1 i_2 i_3})(q_1+q_2+q_3)]$$
$$= 2 g^6 i f_{i_1 i_2 i_3} \frac{p_1 p_2 p_3}{t_1 t_2 t_3} (q_1+q_2+q_3). \tag{7.23}$$

The color factors for the diagrams of Fig. 53 are, of course, more complicated. The two gluons can form states with t-channel color 1, 8_a, and 8_s. For Fig. 53(a) the color factor contains each of the color tensors illustrated in Fig. 57. To extract the full discontinuity giving the Regge cut coupling, we must also add the contribution obtained by replacing the quark loop of Fig. 53(a) with an antiquark loop. The factor of i associated with the on-shell quark now also changes sign. As a result, only the real part of the color factor remains, i.e., the first three diagrams in Fig. 57, which contain an even number of f tensors. These color factors describe, successively, the coupling of 1, 8_a, and 8_s two-gluon states to the two single gluons.

Moving on to Fig. 53(b), we again add the corresponding diagram with an antiquark loop and, because of the factor of $(i)^3$ for each on-shell antiquark, select the color diagrams containing an even number of f tensors, i.e., the diagrams shown in Fig. 58. The first diagram in Fig. 58 gives an antisymmetric coupling of three two-Reggeon states, each carrying odd color parity. The second gives an antisymmetric coupling of two even-color-parity states and one odd-color-parity state, and so on.

Finally we consider color factors for the triple coupling of three-gluon states shown in Fig. 54. Now we have an even number of factors of i from on-shell quarks and so color diagrams with an odd number of f vertices survive when we add the antiquark loop. Three particular color factors that we will be interested in are those of Fig. 59. These are couplings which contain an odd number of f vertices, but provide a symmetric triple coupling of three-gluon states which each carry even color charge parity.

C. Reggeon interaction vertices: Kinematic structure

We discuss now the implications of the results of the last two subsections for Reggeon interaction vertices. First, we consider how the structure of the $T_{L_i,0}$ that we have discussed relates to the general triple-Regge analysis of Sec. IV.

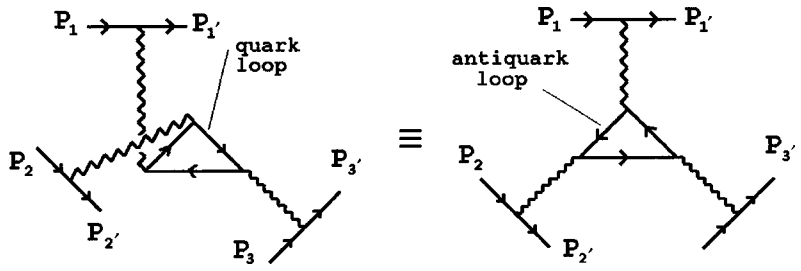

FIG. 56. Additional quark-loop interaction.

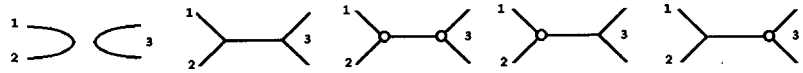

FIG. 57. Color factors for Fig. 53(a).

We can rewrite the above formulas in terms of invariants either by writing, for example,

$$p_1p_2p_3q_1=(p_1p_3)(p_2p_3)(p_3q_3)^{-1}q_3^2 \equiv(s_{23})(s_{31})(s_{11'3})^{-1}q_3^2, \tag{7.24}$$

or we can instead write

$$p_1p_2p_3q_3=(p_1p_3)^{1/2}(p_2p_3)^{1/2}(p_1p_2)^{1/2}q_3 \equiv(s_{31})^{1/2}(s_{23})^{1/2}(s_{12})^{1/2}q_3. \tag{7.25}$$

It then remains to express q_3 directly in terms of invariants. For the special kinematics of the triple-Regge limit L_1, this is particularly simple; i.e., we can write

$$q_3=[Q_1\cdot Q_2]^{1/2}. \tag{7.26}$$

Comparing with Eqs. (4.33) and (4.34), we recognize Eqs. (7.24) and (7.25) as having the form appropriate for a triple-Regge helicity-flip amplitude with $\alpha_1=\alpha_2=\alpha_3=1$. The two expressions (7.24) and (7.25) correspond to the lowest-order contribution from the cuts of Figs. 16(a) and 16(b) if we suppose that the α_i can be expanded perturbatively around unity (as is the case for the trajectory of the Reggeized gluon). Therefore we can potentially associate the q_3 term in $T_{L_1,0}$ [see Eq. (7.4)] with the first of the three hexagraphs in Fig. 15. Similarly, the other two q_i terms could be associated with the other two hexagraphs. Of course, the Feynman diagram of Fig. 52 has no cuts. The cuts appear only as the gluons Reggeize in higher orders. The higher-order loop diagrams of Figs. 53 and 54 do have cuts, and in particular the diagram of Fig. 54 (with the quark lines initially uncut) clearly has all the relevant cuts necessary to contribute to the helicity-flip limit. (See the discussion in Sec. IV D.) If the cuts through this diagram generate Regge cut couplings, as we are anticipating, then we can directly associate the three q_i terms in Eq. (7.19) with the three hexagraphs of Fig. 15.

In the L_2 limit we can proceed similarly and again use Eqs. (7.24) and (7.25) to argue that $T_{L_2,0}$ can be associated with the first of the three hexagraphs in Fig. 15. So just as the general arguments imply, each of three terms appearing in the triple-Regge limit is separately picked out by the corresponding helicity-flip limit. Again, higher-order contributions can produce Reggeization of the gluons and convert Eqs. (7.24) and (7.25) to the form (4.33) and (4.34), respectively.

In the L_2 limit q_3 has a slightly more complicated expression in terms of invariants, i.e.,

$$q_3=\pm\frac{[-\lambda(Q_1^2,Q_2^2,Q_3^2)]^{1/2}}{2[Q_3^2]^{1/2}}. \tag{7.27}$$

[We will discuss shortly the significance of the choice of sign in Eq. (7.27).] Note that Eq. (7.27) satisfies Reggeon Ward identities in that it vanishes linearly when either $Q_1\to0$ or when $Q_2\to0$. When the Q_i are spacelike, $[-\lambda(Q_1^2,Q_2^2,Q_3^2)]^{1/2}$ is the area of the triangle formed by the three momenta and so it vanishes when any one of them vanishes. The denominator spoils the vanishing for $Q_3\to0$. In fact, if $q_3\neq0$, the numerator of the corresponding quark propagator in Eq. (7.7) is off shell. This is what allows two of the Reggeon Ward identities to hold. In contrast, both of the quark propagators which form the Q_3 channel are strictly on shell, and so the $Q_3\to0$ limit gives the on-shell result. In anticipation of the next section, we note that if all three reggeon Ward identities hold, we expect the vertex to have dimension 2 in the Q_i [as would be obtained, for example, by simply removing the denominator in Eq. (7.27)].

D. Reggeon interaction vertices: Signature

The discussion of the previous subsection shows that, kinematically, each of the $T_{L_2,0}$ that we have considered could appear in the corresponding lowest-order multi-Reggeon helicity-flip amplitude. However, we have not yet discussed color parity and signature. As we noted in Sec. IV, signature is defined via a CPT twist that combines color (charge) parity and space parity. Since we are discussing helicity-flip amplitudes, we expect that space parity plays a nontrivial role. The helicity flip is reflected in the presence of the q_i factors, and indeed the sign of q_3, as given by Eq. (7.27), is changed under the parity transformation associated with signature. This change takes place for each of the three t_i channels.

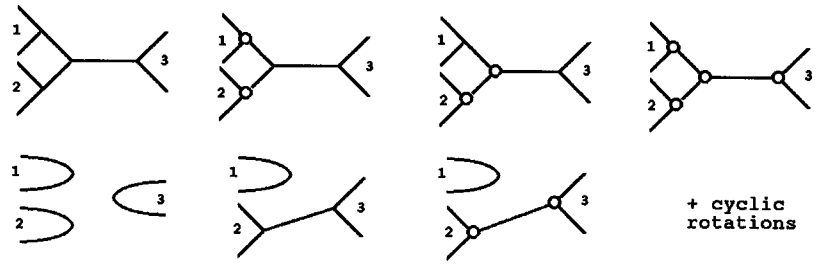

FIG. 58. Color factors for the six-gluon vertex.

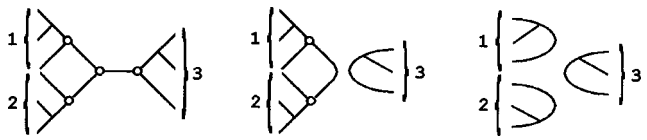

FIG. 59. Color factors for the triple coupling of three-gluon states.

Consider first $T^{111}_{L_2,0}$, with the color factor (7.23) included. The denominator factors of t_i are, of course, the usual gluon particle poles. We use Eq. (7.25) to extract the (potential) helicity-flip Reggeon vertex

$$T^{\mathcal{F},0}_{111} = i f_{i_1 i_2 i_3} q_3, \tag{7.28}$$

with q_3 given by Eq. (7.27). We keep the 0 superscript to indicate both that this is a particular contribution to the general vertex and that it is defined at zero quark mass. Note that since Eq. (7.25) expresses the triple-Regge behavior in terms of invariants that have no kinematic singularities in the Q_i, it defines the appropriate vertex to extract if we wish to consider singular behavior as the $Q_i \to 0$.

By considering signature we implicitly sum over a large number of quark loop diagrams, many of which have a much more complicated discontinuity structure than the ''planar'' loops we have discussed. We introduce signature in the t_i channel by making a CPT transformation of the corresponding initial and final scattering states together with the vertex involved. For the t_3 channel, therefore, we regard Reggeon 1 as scattering into Reggeon 2 by exchanging Reggeon 3. Interchanging 1 and 2 gives a factor of -1 from the color parity of the f tensor and a further factor of -1 from the parity change of sign of q_3. Consequently, Reggeon 3 should be even rather than odd signature if $T^{\mathcal{F},0}_{111}$ is to appear in the vertex. We conclude that $T^{\mathcal{F},0}_{111}$ cannot contribute to the triple-Reggeon vertex. Equivalently, when we sum over all the diagrams for quark and antiquark scattering necessary to define signatured amplitudes, the pieces we have extracted are canceled. The combination of external quark and antiquark vertices requires odd signature for the (Reggeized) gluons to couple while the central vertex requires even signature.

Consider next $T^{\mathcal{F},0}_{112}$ with the color factor given by the first three diagrams of Fig. 57. To give a Reggeon coupling the factor of $J_1(t_3)$ must be converted to a two-Reggeon propagator in higher orders [or for the 8_s Regge pole discussed in the last section, $J_1(t_3)$ must contribute to Reggeization]. In the first color diagram, there is no color factor and so the change of sign of the momentum factor is in direct conflict with the required even signature of the two-Reggeon state. In the second diagram, one f tensor forms an 8_a two-Reggeon state which then couples to the two single Reggeons via a vertex of the same form as Eq. (7.28). In this case the color and momentum factors do combine to give even signature in the t_3 channel. In the t_1 (and t_2) channel, the situation is more complicated. Because the Reggeon states in the t_2 and t_3 channels are distinct, there is no simple parity property for their interchange. However, in the next section we will be interested in the situation in which all Reggeons in a Reggeon state carry zero transverse momentum and the state itself produces a universal canonical transverse momentum dependence. In this case we need not distinguish between distinct Reggeon states when interchanging them to obtain signatured couplings. Consequently, in discussing the signature effects of color factors, we only need consider the symmetry of the color tensor in the Reggeon vertex and not the tensors involved in forming the Reggeon states. In particular, in the t_1 and t_2 channels we only need consider the symmetry of the tensor in the vertex (7.28). Combined with the negative parity of q_3, this gives even signature for the t_1 and t_2 channels, where odd signature is required. So again there is no vertex. The third diagram of Fig. 57 replaces the f tensor of Eq. (7.28) with a d tensor and so gives odd signature for the t_3 channel where even signature is required.

E. Reggeon interaction vertices: Anomalous Reggeon states and the anomalous odderon

Now consider $T^{\mathcal{F},0}_{222}$ with the color factors given by the diagrams of Fig. 58. In this case the vertex color factor has to provide a change of sign to compensate for the change of sign of the momentum factor, in order to give even signature in each of the channels. The first diagram of Fig. 58, which exists in both SU(2) and SU(3), achieves this by coupling three 8_a two-Reggeon states with a vertex of the form (7.28). Therefore $T^{\mathcal{F},0}_{222}$ can appear in a triple coupling of two-Reggeon states that have ''anomalous color parity''; i.e., the color parity is not equal to the signature. Normally (i.e., in next-to-leading logarithmic perturbation theory), because of helicity conservation, there is no 8_a two-Reggeon state. As we noted in Sec. VI B, the two-Reggeon state has color parity $+1$ and signature $+1$. We refer to states with anomalous color parity as ''anomalous Reggeon'' states. Such Reggeon states will will not appear when quarks scatter with their helicity conserved (as is the case for the leading-order perturbative couplings discussed in the last section and must be the case to all orders when the quarks are massless). However, these states will couple between $T^{\mathcal{F},0}_{222}$ vertices.

The second diagram of Fig. 58 also provides an interesting coupling. It does not exist in SU(2), but in SU(3) it gives a $T^{\mathcal{F},0}_{222}$ vertex of the form (7.28) that couples an anomalous 8_a state to two even-signature 8_s states that are not anomalous. As we discussed in Secs. V C and VI B, the 8_s even signature channel contains a bound-state Reggeon that is exchange degenerate with the Reggeized gluon. If we denote an anomalous Reggeon state by ''A'' and a normal reggeon state by ''N,'' the first two diagrams of Fig. 58, respectively, produce

$$\text{``}AAA\text{''} \quad \text{and} \quad \text{``}ANN\text{''}$$

couplings. This is analogous to the well-known ''$AAA+AVV$'' structure of the triangle anomaly, where A denotes an axial vector coupling and V denotes a normal vector coupling. All the remaining diagrams in Fig. 58 contain a symmetric vertex color factor that cannot offset the odd-parity property of q_3.

Finally, we consider $T^{\mathcal{F},0}_{333}$. Again, this has the kinematic structure of Eq. (7.29), but now with color factors such as the three diagrams shown in Fig. 59. These are the only diagrams giving a triple coupling of anomalous three-Reggeon

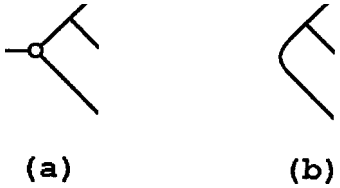

FIG. 60. SU(3) color tensors for (a) the octet odderon and (b) the singlet odderon.

states (i.e., *AAA* couplings). The anomalous color parity three-Reggeon state will play an important role in the next section. We refer to it as the ''anomalous odderon'' state. In SU(3) we can form an anomalous odderon either as a color octet or a color singlet by using the tensors shown in Fig. 60.

The first diagram of Fig. 59 couples three color octet anomalous odderons. We obtain odd signature for each three-Reggeon state by combining the even color parity of the central d tensor with the odd parity of the momentum factor; i.e., the three-Reggeon states couple with an effective triple vertex

$$T^{\mathcal{F},0}_{333}=d_{i_1 i_2 i_3}q_3, \tag{7.29}$$

where, again, q_3 is given by Eq. (7.27). The three-Reggeon states have even color parity since they are obtained by combining an odd df factor with an odd number of gluons (Reggeons).

The second diagram of Fig. 59 couples two color octet anomalous odderons and one color singlet. The third diagram in Fig. 59 couples three color singlet anomalous odderons and simply leads to a vertex

$$T^{\mathcal{F},0}_{333}=q_3, \tag{7.30}$$

with no color factor. Equation (7.30) exists in both SU(2) and SU(3). In SU(2) there is only a color singlet anomalous odderon. However, the SU(3) color octet anomalous odderon has a component that transforms as an SU(2) singlet with respect to an SU(2) subgroup. For this component the SU(2) version of the third diagram of Fig. 59 is obtained from the first two SU(3) diagrams by projecting onto the SU(2) subgroup. Since the three-Reggeon states carry anomalous color parity, they also will not couple to single quarks scattering with their helicity conserved. Again, these states will couple between $T^{\mathcal{F},0}_{333}$ vertices.

The above arguments generalize to any number of gluons coupling via a single-quark loop. It is straightforward to show that there are *AAA* $T^{\mathcal{F},0}_{223}$ vertices of the form (7.29) and (7.30) that couple anomalous color octet [triplet for SU(2)] two-Reggeon states to color octet and color singlet anomalous odderons, respectively. The first possibility exists only in SU(3), of course. A $T^{\mathcal{F},0}_{233}$ vertex of the form (7.28) exists in SU(3) with color octet anomalous odderon states. There is no corresponding vertex for color singlet anomalous odderons. Although we have discussed only the lowest-order couplings explicitly, it is clear that there is a large set of even- and odd-signature anomalous color parity multi-Reggeon states that couple through helicity-flip vertices of the kind that we have isolated. Such vertices can appear in reggeon diagrams only within the $T^{\mathcal{F}}_{m'n'r'}$ vertices discussed in Sec. V.

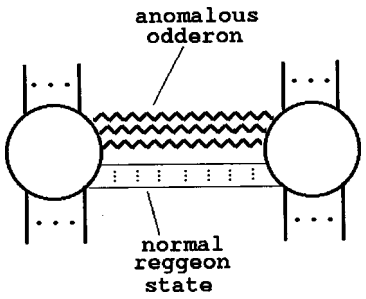

FIG. 61. General amplitude containing the anomalous color parity three-Reggeon state—the ''anomalous odderon.''

In addition to the $T^{\mathcal{F},0}$ *AAA* vertices, there will also be a corresponding variety of *ANN* vertices. In most of our discussion in the next section, we will specifically consider only the *AAA* couplings of anomalous Reggeon states. We will see that the dynamics is determined by the *AAA* couplings, most importantly because the *AAA* coupling (7.28) provides the only $T^{\mathcal{F},0}$ coupling (either *AAA* or *ANN*) of color-zero states within SU(2) and ultimately it is SU(2) color singlet couplings and infrared divergences that will interest us.

F. General couplings of anomalous Reggeon states

Note that while the anomalous Reggeon states do not couple to helicity-conserving elastic scattering states, they will couple in general multiparticle amplitudes, provided only that the initial and final states have different parity properties. A general amplitude of this kind is illustrated in Fig. 61. In such amplitudes the anomalous Reggeon couplings will automatically satisfy the Reggeon Ward identities. The distinctive feature of the helicity-flip couplings we have discussed in this section is that they are associated with a violation of these identities in the massless quark theory. This is the subject of the next section.

VIII. INFRARED DIVERGENCES AND CONFINEMENT

In the last section we found that anomalous color parity Reggeon states can couple through the special helicity-flip vertices that we isolated. These vertices appear in massless quark Feynman diagrams only when the $m\rightarrow 0$ limit is taken after a zero-transverse-momentum limit. In this section we describe how, within Reggeon diagrams containing the relevant interactions, imposition of the Reggeon Ward identities with $m\neq 0$ implies that these vertices survive the $m\rightarrow 0$ limit. We will then indicate how, in the particular circumstances that the SU(3) gauge symmetry of QCD is broken to SU(2), infrared divergences appear as $m\rightarrow 0$. These divergences produce what we call ''a confinement phenomenon.'' By ''confinement'' we mean that a particular set of color-zero states is selected that contains no massless multigluon states and has the necessary completeness property to consistently define an S matrix. That is, if two or more of this set of states initially scatter via QCD interactions, the final states consist only of arbitrary numbers of the same set of

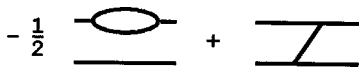

FIG. 62. Singular part of the BFKL kernel.

states. Our discussion is no more than an outline argument and certainly is not a rigorous proof that this form of confinement occurs. Nevertheless, we believe that the argument is straightforward and that there is no reason to believe it cannot be improved significantly.

A. Properties of massless Reggeon interactions

Before discussing the effects of the helicity-flip quark loop interactions, we first summarize what is known from existing calculations about the general properties of the elastic scattering Reggeon amplitudes A^{τ}_{mn} discussed in Sec. V when the gluon mass $M\to 0$. The best-known example of an elastic scattering Reggeon amplitude is, of course, the BFKL kernel [5]. We first recall the infrared properties of this kernel.

Taking the massless limit in Eq. (5.21) and including the trajectory contribution (5.18) as part of the interaction, we obtain the leading-order singular part of the color zero kernel. This can be written in terms of transverse momentum diagrams as in Fig. 62. (The full kernel is obtained by adding the diagrams with the initial states interchanged.) We have not shown the regular part of the kernel. As we remarked earlier, the regular part is uniquely determined [22] from the singular part by the requirement that the full kernel satisfy the reggeon Ward identities. Since the notation includes momentum-conserving δ functions, the diagrams are formally scale invariant (even though potentially infrared divergent). The infrared cancelation that provides the finiteness of the kernel is illustrated diagrammatically in Fig. 63. The dashed line carries zero transverse momentum. This cancellation is present only in the color-zero channel. When higher-order corrections to the kernel are calculated, the infrared finiteness and Reggeon Ward identities persist [19]. Therefore, for our purposes, it is sufficient to frame our discussion in terms of the leading-order diagrams.

As we have emphasized in previous sections, the helicity-flip interactions do not appear in elastic scattering Reggeon diagrams. As a consequence, when $M\to 0$, gauge invariance implies that the Reggeon Ward indentities hold for all the A^{τ}_{mn}. For $t=Q^2\neq 0$, the resulting zeros are sufficient to compensate for any internal infrared divergences of the A_{mn} due to the Reggeon propagators [i.e., due to the particle pole factors of $(k_r^2+M^2)^{-1}$ that we have included in Eq. (5.17) as defining a Reggeon propagator]. Therefore, for $Q^2\neq 0$, all infrared divergences arise only from particle singularities within the Reggeon interactions.

We anticipate that the above features of the BFKL kernel generalize as follows. When Reggeization effects are included as part of the interaction, all color-zero interactions are infrared finite for $Q^2\neq 0$. For nonzero color all interactions are infrared divergent, even when $Q^2\neq 0$. As discussed in [11], Reggeon unitarity implies that these divergences necessarily exponentiate amplitudes to zero as $M\to 0$. Therefore only Reggeon states with zero t-channel color survive in the massless limit. Note that this is not equivalent to confinement since the multi-Reggeon states are still present and produce a branch point at $Q^2=0$. Most important for our purposes, the infrared finiteness of the interactions implies that the canonical divergence of the multi-Reggeon state $Q^2=0$; i.e.,

$$\int d^2\underline{k}_1\cdots d^2\underline{k}_N\,\delta^2(\underline{Q}-\underline{k}_1-\underline{k}_2-\cdots-\underline{k}_N)\times\frac{1}{\underline{k}_1^2}\cdots\frac{1}{\underline{k}_N^2}\sim\frac{1}{Q^2} \tag{8.1}$$

persists in the presence of interactions. Normally, this divergence is eliminated (e.g., in discussions of the BFKL equation) by using gauge-invariant couplings [the external particle-Reggeon couplings G_m in Eq. (5.15)] that have Reggeon Ward identity zeros.

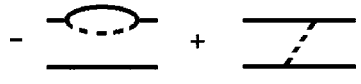

FIG. 63. Infrared finiteness of the BFKL kernel.

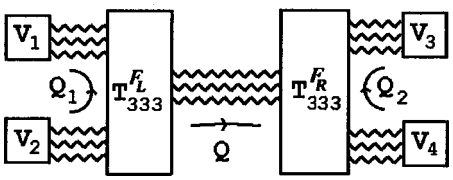

FIG. 64. Reggeon diagram involving anomalous odderon Reggeon states.

B. Infrared scaling of helicity-flip vertices

We now begin our discussion of an infrared phenomenon involving massless Reggeons and massless quark helicity-flip vertices. A focal point for most of the following discussion will be the Reggeon diagram shown in Fig. 64 in which anomalous odderon Reggeon states containing three massless Reggeized gluons are coupled by two helicity-flip vertices. We suppose that this diagram is embedded in a larger diagram so that Q, Q_1, and Q_2 are each integrated over. The V_i boxes represent the remainder of the full diagram (in general, they will be indirectly coupled by additional Reggeons). An example of such an embedding is the diagram shown in Fig. 65. In this diagram, the thick lines represent the anomalous odderon Reggeon state, and for the moment, the thin lines represent any normal (i.e., nonanomalous) combination of Reggeons. We take both the thick and thin lines to be color singlets. For our initial discussion the gauge group could be either SU(3) or SU(2). Although we do not show (A_{mn}) interactions within the Reggeon states, they can be present within both the odderon and normal states without modifying our discussion. We will discuss later interactions that link Reggeons in the normal state with those in the odderon state. Figure 65 will correspond to the hexagraph in Fig. 43 and will be of the form illustrated in Fig. 44 provided

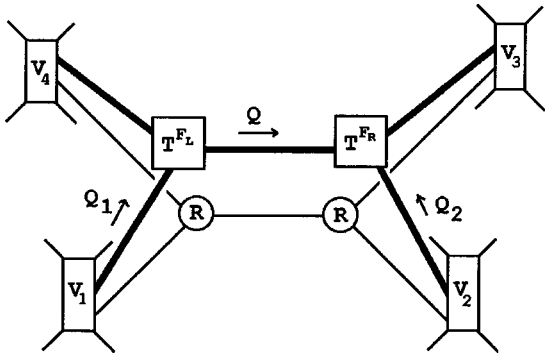

FIG. 65. Embedding Fig. 64 in a larger diagram.

the V_i have the necessary structure. Comparing with the diagram of Fig. 41, it is then clear that T^{F_L} ($\equiv T^{\mathcal{F}_L}_{333}$) and T^{F_R} ($\equiv T^{\mathcal{F}_R}_{333}$) can contribute as helicity-flip vertices. (These vertices must, of course, be energy-nonconserving and couple distinct scattering channels as shown. In all the diagrams we discuss, there will be a combination of a ''regular'' vertex R and a T^F vertex that appear together as a single disconnected Reggeon interaction. The regular vertex will be a nonflip, energy-conserving vertex that could appear in elastic scattering Reggeon diagrams.)

We suppose that $T^{\mathcal{F}_L}_{333}$ and $T^{\mathcal{F}_R}_{333}$ contain all the diagrams analogous to those of Fig. 51, together with the corresponding Pauli-Villars regulator diagrams, which are needed to obtain the full range of Reggeon Ward identities when the quark mass $m\neq 0$. Both vertices contain $\Gamma\mu_1\mu_2\mu_3$, m^2 contributions. We concentrate on the infrared region where we expect the presence of the $T^{\mathcal{F},0}_{333}$ vertices to be most significant; i.e., we consider the region

$$Q_1\sim Q_2\sim Q\to 0. \tag{8.2}$$

We also consider the internal phase-space region of the Reggeon states where each Reggeon carries transverse momentum $k_i\sim Q$. In this region, as we discussed above, color-zero Reggeon interactions can be present, but because they are infrared finite, the full Reggeon state scales canonically as ''$1/Q^2$.'' Figure 64 then gives

$$\begin{aligned}\int \cdots \frac{d^2Q_1}{Q_1^2}\frac{d^2Q_2}{Q_2^2}\, V_1(\ldots,Q_1)V_2(\ldots,Q-Q_1)V_3(Q_2,\ldots)\\ \times V_4(Q-Q_2,\ldots)\int \frac{d^2Q}{Q^2(Q-Q_1)^2(Q-Q_2)^2}\\ \times T^{\mathcal{F}_L}_{333}(Q_1,Q)T^{\mathcal{F}_R}_{333}(Q,Q_2)\\ \times[\text{Reggeon propagators}].\end{aligned} \tag{8.3}$$

A vital property of the $T^{\mathcal{F},0}$ vertices is that they have dimension 1 with respect to transverse momentum. This should be contrasted with the dimension 2 of the elastic Reggeon interaction vertices which appear in the A_{mn}, for example, Γ_{22} given by Eqs. (5.20) and (5.21). When combined with the momentum-conserving δ function, dimension-2 interactions naturally produce a scale-invariant massless Reggeon theory in the infrared region. As we observed following Eq. (7.27), the loss of a dimension is coupled to the loss of a Reggeon Ward identity. Since this identity is reinstated by the addition of the extra diagrams of Fig. 51, we expect the full $T^{\mathcal{F}}_{333}$ to have the normal dimension-2 infrared behavior. Therefore, when $m\neq 0$, the limit (8.2) will give

$$T^{\mathcal{F}}_{333}\sim Q^2, \tag{8.4}$$

whereas

$$T^{\mathcal{F},0}_{333}\sim CQ, \tag{8.5}$$

where C is a constant which depends on precisely how the limit (8.2) is defined in terms of the Q_i and also contains a color factor.

Let us first ignore the Q_1 and Q_2 dependence of the V_i vertices, and consider the behavior of the remainder of Eq. (8.3) in the region (8.2). If we insert Eq. (8.4) for $T^{\mathcal{F}}_{333}$, we obtain

$$\begin{aligned}\int \frac{d^2Q}{Q^2}\left(\int \frac{d^2Q}{Q^4}\, T^{\mathcal{F}_L}_{333}(Q,Q)\right)\left(\int \frac{d^2Q}{Q^4}\, T^{\mathcal{F}_R}_{333}(Q,Q)\right)\\ \sim \int_0 \frac{d^6Q}{Q^6},\end{aligned} \tag{8.6}$$

which is only logarithmically divergent, and so any power convergence provided by the V_i will be sufficient to give a finite integral. Since each of the V_i will, in general, satisfy a Reggeon Ward identity giving

$$V_i(Q)\underset{Q\to 0}{\sim} Q \quad [\equiv V(Q)], \tag{8.7}$$

we expect no infrared divergence problem—provided Eq. (8.4) holds. [We will use $V(Q)$ generically in the following to indicate a coupling that vanishes linearly in Q.]

If we instead insert the behavior (8.5) for $T^{\mathcal{F}}_{333}$ and now include the V_i, we find that Eq. (8.6) is replaced by

$$\int_0 \frac{d^6Q}{Q^8}\prod_i V_i(Q). \tag{8.8}$$

In this case at least three of the V_i must satisfy Eq. (8.7) to ensure convergence. If we choose, say, V_1 and V_2 to not vanish as Q_1, $Q_2\to 0$, there will be a logarithmic divergence of the form

$$\begin{aligned}\int \frac{d^2Q}{Q^2}\left(\int \frac{d^2Q}{Q^4}\, V(Q)T^{\mathcal{F}_L,0}_{333}(Q,Q)\right)\\ \times\left(\int \frac{d^2Q}{Q^4}\, V(Q)T^{\mathcal{F}_R,0}_{333}(Q,Q)\right)\\ \equiv \int \frac{d^2Q}{Q^2}\, K[T^{\mathcal{F}_L,0}_{333}]K[T^{\mathcal{F}_R,0}_{333}],\end{aligned} \tag{8.9}$$

where the functional

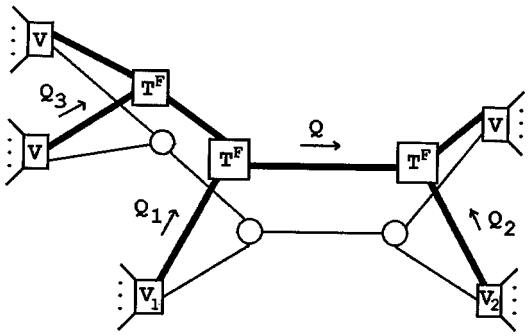

FIG. 66. Reggeon diagram containing three $T^{\mathcal{F}}$ vertices.

$$K[T^{\mathcal{F}}]=\int \frac{d^2Q}{Q^4}\,V(Q)T^{\mathcal{F}}(Q) \tag{8.10}$$

will occur again in the following. If $T^{\mathcal{F}}(Q)$ satisfies Eq. (8.5), then $K[T^{\mathcal{F}}]$ is logarithmically divergent in the infrared region.

Consider next a diagram with an additional $T^{\mathcal{F}}$ vertex and having the structure of Fig. 66. With the vertices appropriately chosen, this diagram can be associated with the hexagraph of Fig. 45. Again, thick lines represent the anomalous odderon Reggeon state, thin lines are any normal Reggeon state, and both can contain interactions. Now, as indicated, there are four independent transverse momenta integrated over. If we again choose V_1 and V_2 to be finite when $Q_1,\ Q_2\to 0$, we obtain, from Fig. 66,

$$\int \frac{d^2Q}{Q^2}\,K^3[V,T^{\mathcal{F}}], \tag{8.11}$$

and if we insert Eq. (8.5), the overall logarithmic divergence persists.

Before proceeding further we consider how Eqs. (8.4) and (8.5) are interrelated by the Reggeon Ward identities as $m\to 0$. We discuss this in terms of a simple model that illustrates the general behavior to be expected.

C. Triangle anomaly and Reggeon Ward identities

We first make the separation

$$T^{\mathcal{F}}_{333}=T^{\mathcal{F},m^2}+\tilde{T}^{\mathcal{F}}, \tag{8.12}$$

where $T^{\mathcal{F},m^2}$ contains the contribution from $\Gamma\mu_1\mu_2\mu_3$, m^2, and $\tilde{T}^{\mathcal{F}}$ does not contain any singular behavior associated with the quark triangle diagram. If we write, in the region (8.2),

$$T^{\mathcal{F},m^2}(m^2,Q)=T^{\mathcal{F},0}F(Q/m)=CQF(Q/m), \tag{8.13}$$

an oversimplified model for $F(x)$, which nevertheless gives the essential behavior of the triangle graph, is

$$F(x)=\frac{1}{(1+x)^2}. \tag{8.14}$$

The Pauli-Villars quarks in $\tilde{T}^{\mathcal{F}}$ will give the same singular behavior, but with the opposite sign and with the light-quark mass scale replaced by the cutoff scale m_λ. Therefore we can take

$$\tilde{T}^{\mathcal{F}}(m,Q)=-CQ\left(\frac{m_\lambda^2}{(m_\lambda+Q)^2}\right)+\cdots, \tag{8.15}$$

and so for the full $T^{\mathcal{F}}$ we obtain

$$T^{\mathcal{F}}(m,Q)=CQ\left(\frac{m^2}{(Q+m)^2}-\frac{m_\lambda^2}{(Q+m_\lambda)^2}\right)+\cdots$$

$$\underset{Q\to 0}{\to} CQ^2\left(\frac{2}{m_\lambda}-\frac{2}{m}\right)+\cdots. \tag{8.16}$$

Now consider

$$I(m)=K[VT^{\mathcal{F}}G]\equiv\int \frac{d^2Q}{Q^3}\,T^{\mathcal{F}}(m,Q)G(m,Q), \tag{8.17}$$

where $G(m,Q)$ is regular at $m\sim Q\sim 0$ and represents the remainder of some Reggeon diagram. Substituting our model for $T^{\mathcal{F}}(m,Q)$, we obtain

$$\begin{aligned}I(m)&=C\int_0\frac{d^2Q}{Q^2}\left(\frac{m^2}{(m+Q)^2}-1+\frac{2Q}{m_\lambda}+\cdots\right)G(m,Q)\\&=-C\int_0\frac{d^2Q}{(m+Q)^2}\,G(m,Q)\\&\quad -C\int_0\frac{d^2Q}{Q^2}\left(\frac{2Qm}{(Q+m)^2}-\frac{2Q}{m_\lambda}+\cdots\right)G(m,Q)\\&\equiv I_1(m)+I_2(m).\end{aligned} \tag{8.18}$$

$I_2(m)$ is finite as $m\to 0$, while $I_1(m)$ gives

$$I_1(m)\to -C\,\ln[m^2]G(0,0). \tag{8.19}$$

Therefore we have a logarithmic divergence with the residue given by the remainder of the Reggeon diagram evaluated at $Q=0$.

In the above model we have

$$T^{\mathcal{F}}(0,Q)\sim -CQ+O(Q^2), \tag{8.20}$$

where the leading term can simply be identified with $-T^{\mathcal{F},0}$. The model illustrates simply the general situation. The use of a Pauli-Villars ultraviolet cutoff implies that in the infrared region, where all transverse momenta are uniformly small, the Reggeon Ward identities are satisfied by a simple cancellation between the light-quark triangle graph and the corresponding regulator graph. However, the nonuniformity in the neighborhood of $Q\sim m\sim 0$ implies that the limits $Q\to 0$ and $m\to 0$ do not commute for the light-quark graph. Consequently, the satisfaction of the Reggeon Ward identities when $m\neq 0$ implies that they are partially lost in the limit $m\to 0$. However, the offending contribution, i.e., $T^{\mathcal{F},0}$, can be evaluated in terms of a loop of on-shell massless quarks. As we discussed in Sec. VI, such a contribution can violate the Reggeon Ward identities while not violating the underlying Ward identities that give the gauge invariance of the theory.

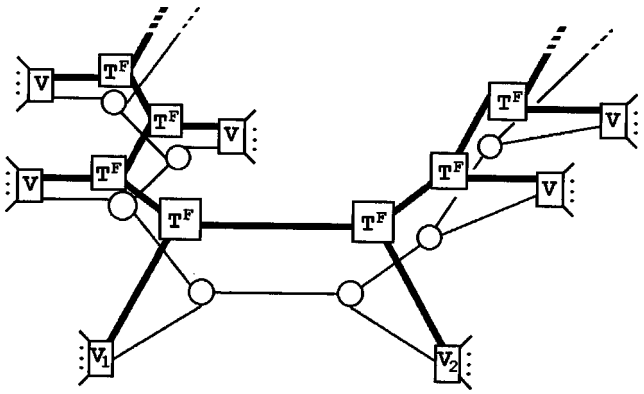

FIG. 67. Reggeon diagram involving many helicity-flip vertices.

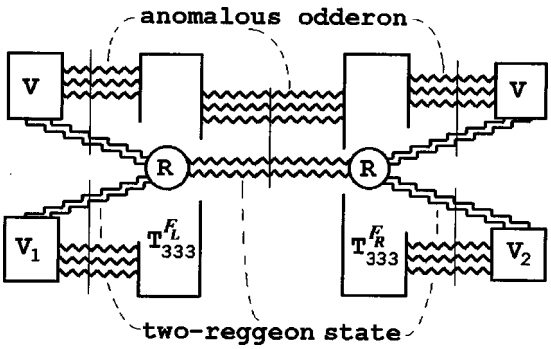

FIG. 68. Infrared-divergent diagram.

It is apparent from Eqs. (8.15)–(8.20) that we are seeing the infrared presence [26] of the anomaly in the triangle graph reflected in Reggeon interactions involving anomalous parity Reggeon states. This happens for the reasons discussed in Sec. VII A. Gluon Ward identities relate the longitudinal Regge limit interactions to transverse interactions that can be sensitive to the anomaly. In addition, the anomalous color parity of, for example, the anomalous odderon three-Reggeon state determines that, effectively, it has an infrared ''axial vector coupling'' via on-shell quark states. (As we stated would be the case, in this section we have considered only *AAA* couplings. We recall from the last section that, as for the normal anomaly, we also have *ANN* couplings.)

We can also view our ultraviolet regularization procedure, using Pauli-Villars regulator fermions, as responsible for introducing the anomaly in the infrared region. If we consider all the quark loops implicitly involved in our discussion, it is straightforward to see that for many of them the γ-matrix structure will generate reduced loops containing the conventional ultraviolet anomaly. From general arguments we expect the fermion anomaly to introduce an ambiguous interplay between infrared and ultraviolet behavior in the massless quark theory. Our manipulations can be viewed as fixing this ambiguity by requiring a finite Reggeon theory and Reggeon Ward identities for the massive quark theory. In fact, as we discuss further in the next paper, this is very likely to be the only resolution of this ambiguity that gives a unitary solution to the theory.

D. Infrared divergence of diagrams with many helicity-flip vertices

Consider now an arbitrary reggeon diagram containing many $T^{\mathcal{F}}$ vertices, for example, the diagram shown in Fig. 67. Once again, the thick lines represent the anomalous odderon Reggeon state and the thin lines are any normal Reggeon state. As illustrated, for every new $T^{\mathcal{F}}$ vertex introduced there is inevitably an accompanying V vertex which, from normal QCD interactions, will satisfy a Reggeon Ward identity. Consequently, if we impose that V_1 and V_2 are nonzero when the anomalous Reggeon state carries zero momentum and consider $T^{\mathcal{F}}$ to be the full massless quark vertex,the diagram will have an overall infrared logarithmic divergence of the form

$$\int \frac{d^2Q}{Q^2} (K[V,T^{\mathcal{F}}])^{n_T}, \tag{8.21}$$

where n_T is the number of $T^{\mathcal{F}}$ vertices in the diagram. From Eq. (8.18), it is clear that the residue involves evaluating every $T^{\mathcal{F}}$, and therefore every anomalous Reggeon state, at zero transverse momentum. As before, including interactions within the anomalous or the normal Reggeon states does not change the discussion. Recall also that, as we emphasized in Sec. V, because the divergence involves helicity-flip vertices, there is implicitly a zero longitudinal component also associated with the zero transverse momentum of the anomalous Reggeon state.

Imposing that V_1 and V_2 be nonzero when the anomalous Reggeon state carries zero momentum is equivalent to choosing two initial Reggeon scattering states that contain a zero-momentum anomalous component. Figure 67 shows that if these states are allowed to scatter (within QCD) into general Reggeon states, an overall logarithmic divergence selects final states having the same property. This is potentially a completeness property for this class of Reggeon states. The crucial question is then whether the infrared divergence we have found in the class of diagrams we have studied can be canceled by a similar divergence in some further class of diagrams. This is the subject of the next two subsections.

E. Cancellation of infrared divergences

In this subsection we will give an argument suggesting that if all Reggeons are massless, i.e., if SU(3) gauge symmetry is fully restored, then the infrared divergence that we have discussed cancels when all diagrams are summed over. We formulate the argument by discussing the Reggeon diagram of Fig. 68. This is the lowest-order diagram that is most obviously of the form we have discussed. All Reggeon lines represent a single Reggeized (massless) gluon, and since this is a ''lowest-order diagram,'' we specifically exclude interactions within either the anomalous odderon or the normal Reggon states. The multi-Reggeon states, for which Reggeon propagators are present, are indicated by the thin vertical

FIG. 69. Potential canceling configurations.

line. To avoid the exponentiation of infrared divergences in higher orders, these states must carry color zero. In lowest-order, the ''regular'' interaction R between the normal Reggeon states will actually be disconnected. Figure 68 clearly has the form illustrated in Fig. 65 once the anomalous odderon three-Reggeon state is identified with the thick lines and the remaining two-Reggeon state is identified with the thin lines. The logarithmic divergence is present (as $m\to 0$) provided only that V_1 and V_2 are appropriately chosen.

In the previous discussion of this section, we have assumed that the anomalous odderon state separately carries zero color. In this case the two-Reggeon state must also carry zero color. Figure 68 is then the lowest-order diagram containing Fig. 64. However, as we discussed in the previous section, in SU(3) the anomalous odderon can also carry octet color. We also showed that helicity-flip $T^{\mathcal{F},0}$ triple-odderon couplings exist when either all the odderons, or two of the three, carry octet color. In addition, there are anomalous Reggeon states, with $T^{\mathcal{F},0}$ couplings, that contain only two Reggeons and carry octet color. In fact, once we allow anomalous Reggeon states that are not color singlets, Figure 68 is not the lowest-order diagram containing the $m=0$ divergence. The lowest-order diagrams involve combinations of normal one- and two-Reggeon states with anomalous two- and three-Reggeon states. Because the lowest-order R vertices contain only gluon internal interactions, the lowest-order diagrams involve only Reggeized gluon Reggeons. When internal quark interactions are included in the R vertices (or we consider the scattering of multiquark Reggeon states, as we will do in the next paper), the symmetric octet bound-state Reggeon also appears. In this case a particularly simple potential cancellation is between the Reggeon states illustrated in Fig. 69. This cancellation will be particularly relevant for our discussion of deep-inelastic scattering in the next paper.

Since, as we have already said, Fig. 68 is the lowest-order diagram that fits specifically into our previous discussion, we will concentrate on finding diagrams that cancel the divergence of this particular diagram. Since the R vertices are lowest order, they cannot involve internal quark interactions. Consequently, the symmetric octet Reggeon cannot appear in canceling diagrams. Note also that, since color parity is conserved and we have chosen each of the Reggeon channels in Fig. 68 to carry anomalous color parity overall, we do not need to consider AVV vertices (in addition to AAA vertices) when looking for cancellations. We proceed by considering possible alternative couplings for the Reggeons originating from V_1.

If Reggeons within the anomalous and normal Reggeon states interact, additional Reggeon propagators are introduced and a cancellation with Fig. 68 is not possible. The

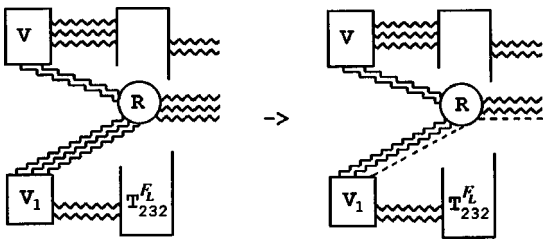

FIG. 70. Divergences to be produced by the regular Reggeon interaction.

most obvious possibility for a cancellation is that a Reggeon participating in the anomalous odderon interaction instead participates in the regular Reggeon interaction, as illustrated in Fig. 70. To produce a zero-quark-mass divergence identical to that in Fig. 68, the regular Reggeon interaction must give an infrared divergence involving the indicated dashed lines. Because the anomalous states with just two Reggeons must carry octet color, the regular Reggeon interaction also carries net octet color. A normal Reggeon interaction carrying nonzero color is necessarily divergent. The simplest divergence will be produced by a massless R_{22} interaction, as in Fig. 71(a). Since the anomalous odderon Reggeons are participating in a helicity-flip interaction, it is also possible for an infrared-divergent interaction to occur as in Fig. 71(b). As we discussed in Sec. VI E, similar Reggeon infrared-divergent interactions to those of Fig. 71 are involved in producing the Reggeon Ward identities for the T^F vertices, for example, the third diagram of Fig. 51.

For $m\neq 0$, the complete cancellation of all divergences related to those of Fig. 71 will necessarily involve all possible interactions between the color-zero five-Reggeon states. This is achieved if we combine all left- and right-side diagrams of the form of Fig. 70 with the corresponding diagrams forming Fig. 68. In this way we obtain a set of diagrams containing triple anomalous Reggeon vertices, which each have the $m=0$ divergence and which, when $m\neq 0$, are related by the cancellation of divergences of the form of Fig. 70. In the infrared region producing the $m=0$ divergence, the cancellation of divergences related to Fig. 70 is between Reggeon interactions having the distinct forms shown in Fig. 72 (all dashed lines carry zero transverse momentum).

Each of the interactions in Fig. 72 contains the $m=0$ anomalous interaction and scales appropriately to generate the logarithmic divergence in individual diagrams. However, the additional infrared cancellation between the complete set of diagrams should survive the $m\to 0$ limit and be sufficient to ensure that there is no $m=0$ divergence. If we go to higher-order and incorporate Reggeon interactions within

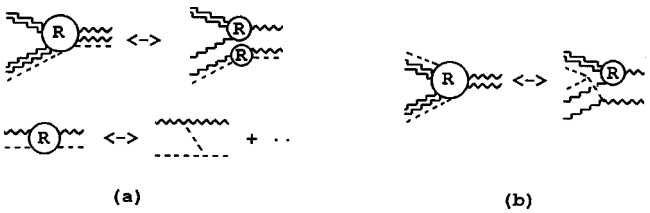

FIG. 71. Regular Reggeon interactions producing divergences.

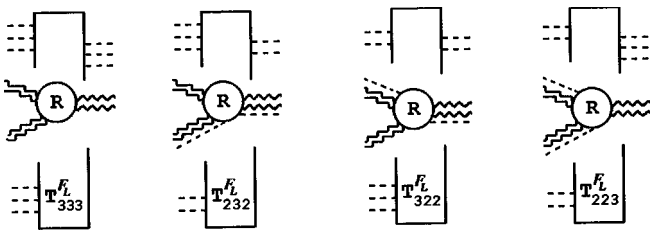

FIG. 72. Reggeon interactions producing the infrared cancellation.

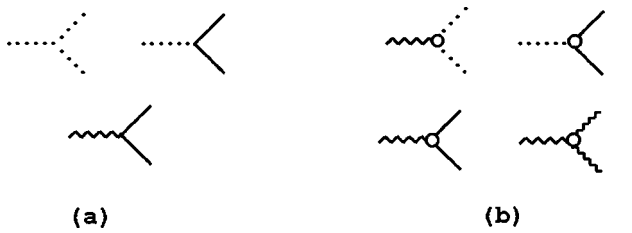

FIG. 74. (a) *f* couplings and (b) *d* couplings after symmetry breaking.

and between the normal and anomalous states, we can expect more elaborate cancellations to hold. We can also expect the *ANN* vertices to play a role. We note that the crucial feature of the cancellation is the existence of infrared-divergent interactions between the Reggeons in the anomalous odderon state and the Reggeons in the normal state. This will be an important dynamical element of our further discussion.

F. Symmetry breaking and confinement

Suppose now that the SU(3) gauge symmetry is only partially restored to SU(2). In this case five of the eight SU(3) gluons remain massive. There is one SU(2) singlet and two SU(2) doublets. We use the notation of Fig. 73. The *f* and *d* couplings of the different representations are illustrated in Fig. 74. The resulting trajectory function transverse momentum diagrams are shown in Fig. 75.

The SU(2) singlet trajectory function contains no massless Reggeon contributions and so is manifestly infrared finite. Therefore this gluon is a simple massive Reggeon which, if color charge parity is carried over from the unbroken theory, carries negative color parity. The two SU(2) doublets form SU(2) singlets with both even and odd SU(3) color parity. The odd-color-parity combination gives the Reggeization of the color singlet Reggeon shown in Fig. 75. The even-color-parity doublet forms a separate infrared finite, even-signature, ''bound-state'' Reggeon with a trajectory that is exchange degenerate with the singlet Reggeized gluon trajectory. The cancellation of Fig. 76 demonstrates simultaneously the infrared finiteness and the Reggeization of this trajectory, provided we omit the contribution of the massless Reggeons. The reason for this omission will soon become apparent. In the massless limit, i.e., as the full SU(3) gauge symmetry is restored, this bound-state trajectory becomes the even-signature octet trajectory, which we referred to in Sec. V C and VI B.

Initially, we consider the complete set of Reggeon diagrams containing both massless and massive Reggeons. *A priori* the $m=0$ logarithmic divergence we have discussed will still be present in individual diagrams containing the

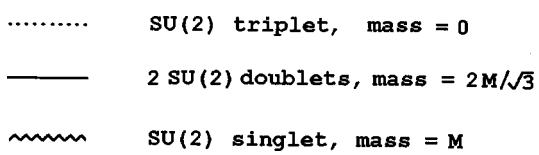

FIG. 73. Notation for the gluon spectrum when the gauge symmetry is broken.

relevant configurations of massless SU(2) Reggeons. For example, if we consider Fig. 68 to be composed entirely of SU(2) massless Reggeons, then the divergence will be present. However, the Reggeon infrared cancellation of Figs. 70–72 also remains valid. In fact, the necessary infrared-divergent interactions will exist, and so, presumably, an analogous cancellation will take place, provided only that one of the normal Reggeon states in the diagram contains massless Reggeons.

An obviously divergent class of diagrams is those of the form of Fig. 77. This diagram is an SU(2) version of Fig. 68, except that the normal Reggeon states contain no massless Reggeons. The Reggeons indicated by the dotted lines are massless and form an SU(2) singlet anomalous odderon state. [From now on we use the dotted line notation to indicate Reggeons that both belong to the massless SU(2) triplet and carry zero transverse momentum in the overall infrared divergence of the diagram.] All the multi-Reggeon states cut by a thin vertical line are SU(2) singlets if, in particular, the additional Reggeon states indicated by a thick unbroken Reggeon line are (some number of) the SU(2) singlet, massive, Reggeized gluons. We recall from the last section that since we now discuss SU(2) color only, to contain $T^{\mathcal{F},0}$ color-zero interactions the $T^{\mathcal{F}}$'s must be *AAA* couplings of anomalous odderons. Since there is no triple coupling for the singlet Reggeon, we cannot take all the normal states to contain only a single Reggeon. (It would be sufficient for some normal states to be a single bound-state Reggeon, but these states require an internal quark regular interaction in order to couple. As we shall see shortly, there is also an additional subtlety involved.)

Figure 77 is obviously of the form of Fig. 65 and so contains the logarithmic divergence. The anomalous odderon three-Reggeon state once again corresponds to the thick lines, while the thin lines are now identified with Reggeon states that, in lowest order, consist of massive SU(2) singlet

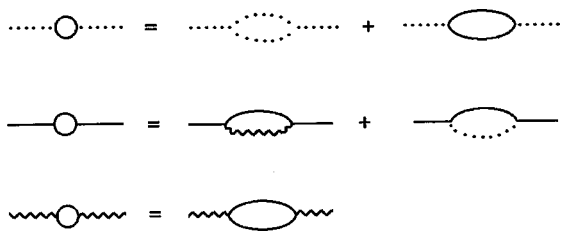

FIG. 75. Trajectory functions for the different representations.

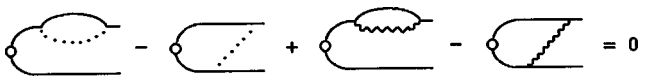

FIG. 76. Reggeization of the bound-state Reggeon.

gluons. From Fig. 74(a) it is clear that, at lowest order, the singlet simply has no coupling to the massless sector. As a result, there are no infrared-divergent interactions analogous to Fig. 71 and no cancellation corresponding to Fig. 72. The analogue of the interactions of Fig. 71 involves the exchange of a massive SU(2) doublet. That is, the divergent interactions that were part of the cancellation with the SU(3) symmetry unbroken now contain massive propagators. This implies that the logarithmic divergence as $m\to 0$ is qualitatively of the form

$$\int_{m^2} dQ^2\left(\frac{1}{Q^2}-\frac{1}{Q^2+M^2}\right)\sim\ln\left(\frac{M^2}{m^2}\right) \tag{8.22}$$

and so is clearly a direct consequence of the symmetry breaking.

All diagrams having the form of Figs. 66, 67, etc., will similarly contain an uncanceled overall logarithmic divergence (with V_1 and V_2 appropriately chosen) if the state represented by the thick lines contains any number of (interacting) massless Reggeons forming a state with the quantum numbers of the anomalous odderon and the thin lines are any combination of (interacting) massive SU(2) singlet Reggeon states. Interactions between the massless and massive Reggeons can take place, but since they are infrared finite, they simply produce Reggeon Ward identity zeros that eliminate the overall infrared divergence. Therefore such interactions do not appear in the divergent diagrams. If the anomalous Reggeon state carries color, interactions within this state will exponentiate the diagram to zero.

Clearly, the thin lines could also be a multiquark Reggeon state, but we will leave a discussion of quark Reggeon states until the next paper. As preparation for our discussion of chiral symmetry breaking, it will be interesting to discuss here how the bound-state Reggeon avoids an infrared interaction of the form of Fig. 70. At lowest order the bound-state Reggeon couples to infrared divergences via the two diagrams illustrated in Fig. 78. Because of the antisymmetry of the gauge coupling, if the two massive Reggeons are in a completely symmetric state, the two diagrams of Fig. 78 cancel. Since it is even signature and symmetric with respect to color, this requires that the bound state carry positive parity (which it does).

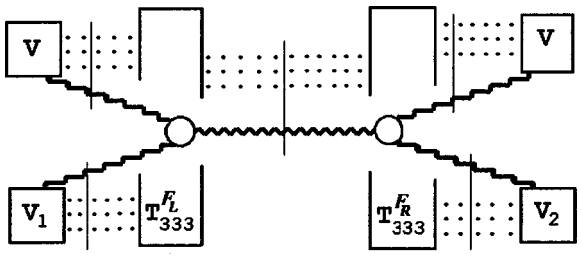

FIG. 77. Diagram containing SU(2) singlet Reggeons.

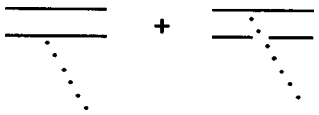

FIG. 78. Bound-state coupling to infrared divergences.

We now take all the amplitudes containing the logarithmic divergence as our physical amplitudes. We remove the divergence as a normalization factor and also factorize off all the V couplings. We are left with a set of multi-Reggeon diagrams in which every Reggeon state has the form shown in Fig. 79, where now the wee-parton component, indicated by the four rows of dots, contains arbitrary numbers of massless Reggeons with odd signature, color zero, and positive color parity. Each massless reggeon carries zero transverse momentum. The wavy line is any combination of massive SU(2) singlet Reggeon states. Note that the odd-signature nature of the wee-parton component switches the signature of the massive Reggeon component of states. In particular, the odd-signature elementary Reggeon gives an even-signature ''Pomeron,'' while the bound-state Reggeon gives an odd-signature, exchange-degenerate, partner to the Pomeron. Because of signature factors, the Pomeron will not generate a vector particle, while the odd-signature bound-state Regge pole will give such a particle at the mass of the SU(2) singlet. In effect, while the Reggeized gluon becomes the Pomeron, the unconfined massive single-gluon vector particle, which in perturbation theory lies on the Reggeized gluon trajectory, is replaced by a composite bound state of confined massive gluons.

We have thus demonstrated the ''confinement phenomenon'' which we referred to earlier. If we insist that two initial scattering Reggeon states have the form of Fig. 79, then these states scatter into arbitrary numbers of the same states only. Also, since the wee-parton component of the state acts like a background ''Reggeon condensate,'' the dynamical properties of the Reggeon states are identical to that of the SU(2) singlet Reggeon component of the state. Therefore we also have confinement in the sense that we have only massive Reggeon states composed of elementary Regge-pole constituents.

As we have emphasized throughout this paper, the zero transverse momenta involved in producing the infrared divergences and Reggeon condensate are implicitly accompanied by longitudinal zero momenta. The presence of this longitudinal component implies that the condensate can potentially be understood as a light-cone zero-mode contri-

FIG. 79. Confinement Reggeon states

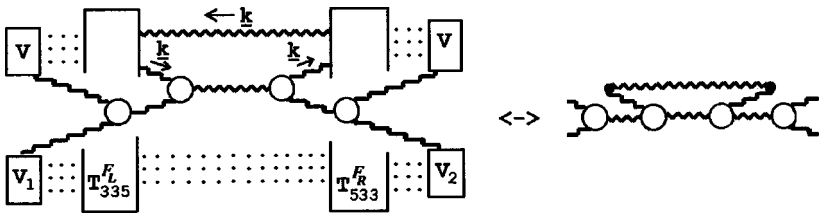

FIG. 80. Diagram with vacuum production of SU(2) singlet Reggeons.

bution at finite momentum or, in the language of the Introduction, as a ''wee-parton'' component at infinite momentum.

G. Supercritical Pomeron

Finally, we note that the divergent diagrams will also include those of the form illustrated in Fig. 80 in which the helicity-flip $T^{\mathcal{F}}$ vertices, in addition to coupling the zero-transverse-momentum anomalous odderon massless Reggeons, produce an additional pair of massive Reggeons carrying zero net transverse momentum. The $T^{\mathcal{F}}$ vertices involved will also contain the triangle anomaly we have discussed. The Reggeon lines in the right-hand diagram of Fig. 80 are ''physical'': i.e., they correspond to either the Pomeron or its odd-signature partner. Diagrams such as Fig. 80, together with all the obvious generalizations, are, effectively, responsible for ''vacuum production'' of massive Reggeon states within the Reggeon diagrams describing our confining theory.

We can, therefore, summarize our confining solution of partially broken QCD as containing exchange-degenerate even- and odd-signature Reggeons, with vacuum production of multi-Reggeon states. These are the defining characteristics of supercritical Pomeron RFT [10]. We have shown that the appearance of this RFT phase is a consequence of the confinement produced by the infrared divergence associated with the massless quark anomaly. (Having derived the massless theory, it should be possible to add effective quark masses to the theory, for example, by chiral perturbation theory, and still remain in the supercritical phase.) We have postponed discussion of the RFT formulation of the supercritical phase to the following paper because we want to emphasize the self-contained nature of the QCD infrared analysis.

We have explicitly associated the supercritical phase with the breaking of SU(3) gauge symmetry to SU(2). The restoration of SU(3) symmetry should follow if we take the zero-mass limit for the SU(2) singlet Reggeon. This is equivalent to setting the intercept of the Pomeron to zero. The principle of complementarity [13] implies that the symmetry can be smoothly restored provided only that an ultraviolet cutoff is introduced. However, since the massless quark divergence has selected only a part of the broken theory, restoration of full SU(3) symmetry is clearly nontrivial. Nevertheless, provided we can completely identify our solution of partially broken QCD with the supercritical Pomeron, setting the Pomeron intercept to zero corresponds to taking the critical limit from within the supercritical phase. Note that two additional important features of this limit must also be realized. That is, both the odd-signature Reggeon partner for the Pomeron and the vacuum production of Fig. 79 must simultaneously decouple as the Pomeron intercept vanishes. The reinstatement of the infrared cancellation of Figs. 69–71 is presumably involved in these effects in a subtle manner.

An inescapable conclusion from our construction is that the Pomeron carries odd color charge parity. The odd and even color parity of the Reggeized gluon and the wee-parton component, respectively, combine to give overall odd color parity. This property will persist after the SU(3) gauge symmetry is restored. Note that to obtain an SU(3) color singlet, the anomalous odderon that appears in the Pomeron has to be an SU(3) octet (rather than the singlet discussed initially in Sec. VIII E). For an odd-color-parity Pomeron to describe total cross sections, the scattering hadrons cannot be eigenstates of color parity. We will show in our next paper that the pion is a mixture of states with even and odd color parity (but odd physical parity). The quark-antiquark and anomalous odderon components are, correspondingly, in either a color singlet or a color octet state. The Pomeron scatters the odd (even) state into the even (odd) state.

The RFT formalism also tells us that the transverse momentum cutoff is a relevant parameter for the critical limit. Therefore, if this (gauge-invariant) cutoff is varied, it is possible for the supercritical phase to appear even when the full gauge symmetry is restored. In this case the direction of the SU(2) wee-parton component is effectively averaged over within SU(3). In the next paper, we will discuss how this can be understood as an average over the SU(2) direction of the anomaly (or instanton effects) in SU(3). It is also possible to regard the large Q^2 of deep-inelastic scattering as introducing a ''finite-volume'' effect which removes the critical phase transition. As a result, the theory remains in the ''single-gluon-dominated'' supercritical phase as the SU(3) symmetry is restored. With the wee-parton component included, this feature can be seen explicitly by studying the Reggeon-gluon diagrams involved [8]. Deep-inelastic scattering is another subject that will be covered in depth in the following paper.

ACKNOWLEDGMENTS

I am particularly grateful to Mark Wüsthoff for extensive discussions of the contents of this paper. I have also benefited, over the years, from many discussions with Jochen Bartels and Lev Lipatov. This work was supported by the U.S. Department of Energy, Division of High Energy Physics, Contracts No. W-31-109-ENG-38 and DEFG05-86-ER-40272.

[1] A. R. White, in *Proceedings of the XVIth Rencontre de Moriond*, Les Arcs, France, edited by J. Tran Thanh Van (Editions Frontières, Dreux, France, 1981), Vol. 2.
[2] V. N. Gribov, Sov. Phys. JETP **26**, 414 (1968); H. D. I. Abarbanel, J. B. Bronzan, R. L. Sugar, and A. R. White, Phys. Rep., Phys. Lett. **21C**, 119 (1975).
[3] A. A. Migdal, A. M. Polyakov, and K. A. Ter-Martirosyan, Zh. Eksp. Teor. Fiz. **67**, 848 (1974) [Sov. Phys. JETP **40**, 420 (1974)]; H. D. I. Abarbanel and J. B. Bronzan, Phys. Rev. D **9**, 2397 (1974).
[4] K. G. Wilson, T. S. Walhout, A. Harindranath, Wei-Min Zhang, S. D. Glazek, and R. J. Perry, Phys. Rev. D **49**, 6720 (1994); L. Susskind and M. Burkardt, hep-ph/9410313, Proceedings of the 4th International Conference on the Theory of Hadrons and Light-Front QCD (Polona Light Cone Quantization, 1994).
[5] E. A. Kuraev, L. N. Lipatov, and V. S. Fadin, Sov. Phys. JETP **45**, 199 (1977); Ya. Ya. Balitskii and L. N. Lipatov, Sov. J. Nucl. Phys. **28**, 822 (1978).
[6] ZEUS Collaboration, Phys. Lett. B **315**, 481 (1993); H1 Collaboration, Nucl. Phys. **B429**, 477 (1994).
[7] H1 Collaboration, C. Adloff *et al.*, in *ICHEP '96*, Proceedings of the 28th International Conference on High Energy Physics, Warsaw, Poland, edited by Z. Ajduk and A. Wroblewski (World Scientific, Singapore, 1997); for a final version of this analysis see Z. Phys. C **76**, 613 (1997).
[8] This issue will be discussed in detail in the second paper. It is briefly discussed in A. R. White , in *Proceedings of the International Conference (7th Blois Workshop) on Elastic and Diffractive Scattering: Recent Advances in Hadron Physics*, edited by K. Kang, S. K. Kim, and C. Lee (World Scientific, Singapore, 1998).
[9] A. R. White, Phys. Rev. D **29**, 1435 (1984).
[10] A. R. White, Int. J. Mod. Phys. A **11**, 1859 (1991); in *Structural Analysis of Collision Amplitudes*, Proceedings of the Les Houches Institute, edited by R. Balian and D. Iagolnitzer (North-Holland, Amsterdam, 1976); H. P. Stapp, *ibid.*
[11] A. R. White, Int. J. Mod. Phys. A **8**, 4755 (1993).
[12] A feeling for the controversy can be obtained by reading M. Le Bellac, in *Proceedings of the International Conference on High Energy Physics*, Tokyo, Japan, edited by S. Homma, M. Kawaguchi, and H. Miyazawa (Physical Society of Japan, 1978) and the following talk by the author. It might be worth noting that, while the majority of RFT theorists opposed our solution, Gribov said early on that he considered it the correct solution and continued to maintain this point of view.
[13] E. Fradkin and S. H. Shenker, Phys. Rev. D **19**, 3682 (1979); T. Banks and E. Rabinovici, Nucl. Phys. **B160**, 349 (1979).
[14] Z. Bern, L. Dixon, and D. A. Kosower, Annu. Rev. Nucl. Part. Sci. **46**, 109 (1996).
[15] H. P. Stapp and A. R. White, Phys. Rev. D **26**, 2145 (1982).
[16] V. N. Gribov, I. Ya. Pomeranchuk, and K. A. Ter-Martirosyan, Phys. Rev. **139**, B184 (1965).
[17] R. C. Brower, C. E. DeTar, and J. H. Weis, Phys. Rep., Phys. Lett. **14C**, 257 (1974).
[18] J. B. Bronzan and R. L. Sugar, Phys. Rev. D **17**, 585 (1978). This paper organizes into Reggeon diagrams the results from H. Cheng and C. Y. Lo, *ibid.* **13**, 1131 (1976); **15**, 2959 (1977).
[19] V. S. Fadin and L. N. Lipatov, Nucl. Phys. **B477**, 767 (1996) and further references therein.
[20] J. Bartels and M. Wüsthoff, Z. Phys. C **66**, 157 (1995).
[21] Y. A. Simonov, Sov. Phys. JETP **21**, 160 (1965); A. R. White, Phys. Rev. D **10**, 1236 (1974).
[22] C. Corianò and A. R. White, Nucl. Phys. **B468**, 175 (1996); A. R. White, Phys. Lett. B **334**, 87 (1994); C. Corianò and A. R. White, Nucl. Phys. **B451**, 231 (1995).
[23] J. L. Cardy, R. L. Sugar, and A. R. White, Phys. Lett. **55B**, 384 (1975).
[24] H. D. I. Abarbanel, J. Bartels, J. B. Bronzan, and D. Sidhu, Phys. Rev. D **12**, 2459 (1978); **12**, 2798 (1978).
[25] G. 't Hooft, Nucl. Phys. **B33**, 173 (1971).
[26] S. Coleman and B. Grossman, Nucl. Phys. **B203**, 205 (1982).